

Thesis Abstract

High repetition rate modelocked lasers ($>1\text{GHz}$) are expected to become key light sources for future developments in laser processing, optical communication and signal processing, LIDAR and remote sensing. However, their realization is complex because cavity size has to be reduced to its minimum, so that light pulses are densely packed in time.

Whispering-gallery-mode (WGM) microresonators are micrometer size devices that confine light both spatially and temporally by frustrated internal reflection, allowing strong light-matter interaction. They proved to be excellent CW laser platforms, because of their high Q factor ($>10^7$) and ultra-low threshold power.

Therefore, modelocking a WGM microlaser would provide a cost-effective and on-chip solution for ultra-high repetition rate laser. However, this poses numerous challenges for the integration of a saturable absorber together with a gain medium in such a small resonator.

This work is an attempt to solve these challenges by providing tools, fabrication methods and a design strategy to modelock a WGM microlaser.

Chapter 1 presents the background and the objective of the research.

Chapter 2 describes the basic theory and fundamental features of WGM microresonators and microlasers, as well as their fabrication method.

Chapter 3 introduces carbon nanotubes (CNT) as saturable absorber and proposes a method to integrate them into a WGM microresonator for passive modelocking.

Chapter 4 focuses on the creation of a reliable simulation model, by case studying an analogous system – a fiber ring laser modelocked by CNT.

Chapter 5 numerically investigates modelocking regime of a WGM microlaser. Operation regimes are identified and design strategy is proposed.

Chapter 6 summarizes the work, explains future works and gives an outlook on the research.

I believe this work paves the way to the realization of an ultra-high repetition rate WGM modelocked microlaser.

Contents

| | |
|---|------------|
| Thesis Abstract | iii |
| 1 Introduction | 1 |
| 1.1 Background | 2 |
| 1.1.1 Invention of Lasers | 2 |
| 1.1.2 CW laser and pulsed laser | 2 |
| 1.1.3 Theory of pulsed lasers | 4 |
| 1.2 High repetition rate modelocked lasers | 6 |
| 1.2.1 Applications | 7 |
| 1.2.2 High repetition rate modelocked laser platforms | 8 |
| 1.3 Objective of this study | 11 |
| 1.3.1 A new laser platform | 11 |
| 1.3.2 Modelocking of a WGM microlaser | 12 |
| 1.3.3 Research roadmap & Thesis overview | 12 |
| 2 WGM microresonator | 17 |
| 2.1 Q factor | 18 |
| 2.2 Optical modes in WGM microresonators | 19 |
| 2.2.1 Whispering-gallery modes | 19 |
| 2.2.2 Effective mode area | 21 |
| 2.2.3 Evanescent field | 21 |
| 2.2.4 Dispersion in WGM microresonators | 24 |
| 2.3 Fabrication of WGM microresonators | 25 |
| 2.3.1 Silica WGM microsphere | 25 |
| 2.3.2 Silica WGM microtoroid | 25 |
| 2.4 Coupling light in WGM microresonators | 27 |
| 2.4.1 Optical tapered fiber | 27 |
| 2.4.2 Coupling mode theory | 29 |
| 2.4.3 Q factor measurement | 30 |
| 2.5 Active WGM microresonator | 30 |
| 2.5.1 Er-doped WGM microsphere | 32 |
| 2.5.2 Er-doped WGM microtoroid | 32 |
| 2.6 Summary | 36 |
| 3 Carbon nanotubes as saturable absorber | 37 |
| 3.1 Saturable absorbers in pulsed lasers | 38 |
| 3.2 Single-walled carbon nanotubes | 40 |
| 3.3 Raman scattering spectroscopy of carbon nanotubes | 43 |

| | | |
|----------|--|------------|
| 3.4 | CNT integration methods | 46 |
| 3.4.1 | CNT optical deposition around tapered fibers | 46 |
| 3.4.2 | CNT microprobe | 52 |
| 3.5 | Summary | 60 |
| 4 | Modelocked fiber ring laser | 61 |
| 4.1 | Theoretical framework | 62 |
| 4.1.1 | Modified nonlinear Schrödinger equation | 62 |
| 4.1.2 | Step size determination | 64 |
| 4.2 | Modelocked fiber ring laser - Experiment | 65 |
| 4.2.1 | Er-doped fiber | 66 |
| 4.2.2 | Carbon nanotubes on fiber ferrule | 68 |
| 4.2.3 | Realization of ML fiber ring laser | 68 |
| 4.3 | Simulation vs Experiment | 72 |
| 4.4 | Summary | 73 |
| 5 | WGM modelocked microlaser | 75 |
| 5.1 | Theoretical framework - revisited | 76 |
| 5.2 | Modelocking investigation | 76 |
| 5.2.1 | Contribution graph | 76 |
| 5.2.2 | Modelocking detection | 78 |
| 5.2.3 | Operation regimes | 81 |
| 5.3 | WGM modelocked microlaser design | 84 |
| 5.3.1 | Small signal gain estimation | 84 |
| 5.3.2 | Gain and loss | 88 |
| 5.3.3 | Dispersion | 88 |
| 5.3.4 | Design strategy | 92 |
| 5.4 | Summary | 96 |
| 6 | Summary, future works and outlook | 97 |
| 6.1 | Summary | 98 |
| 6.2 | Future works | 98 |
| 6.3 | Outlook | 101 |
| A | Marangoni effect | 103 |
| B | Er-doped fiber simulation | 107 |
| C | SA parameters relationship | 109 |
| D | Gain and SA power saturation | 113 |
| | References | 115 |
| | List of achievements | 125 |

List of abbreviations

| | |
|--------|---|
| AC | SHG AutoCorrelator |
| CVD | Chemical Vapor Deposition |
| CW | Continuous Wave |
| EDFA | Erbium Doped Fiber Amplifier |
| FFL | Femtosecond Fiber Laser |
| FSR | Free Spectral Range |
| GVD | Group Velocity Dispersion |
| HRR | High Repetition Rate |
| HML | Harmonic ModeLocking |
| ISO | ISolator |
| ML | ModeLocking |
| MNLSE | Modified NonLinear Schrödinger Equation |
| OSA | Optical Spectrum Analyzer |
| OSC | OSCilloscope |
| PWM/PM | Power Meter |
| RBM | Radial Breathing Mode |
| RSS | Raman Scattering Spectroscopy |
| SA | Saturable Absorber |
| SAM | Self-Amplitude Modulation |
| SESAM | SEmiconductor Saturable Absorber Mirror |
| SPM | Self-Phase Modulation |
| SSFM | Split Step Fourier Method |
| SWCNT | Single-Walled Carbon Nanotube |
| TE | Transverse Electric |
| TLD | Tunable Laser Diode |
| TM | Transverse Magnetic |
| VOA | Variable Optical Attenuator |
| WGM | Whispering-Gallery Mode |

Chapter 1

Introduction

The invention of lasers has changed the way we live. And they will surely keep changing it for many years. The science of lasers is under constant evolution and laser technology is far from saturated.

Under this considerations, it is extremely important to keep realizing better and better lasers - that push their frontiers further - to satisfy the huge demand of new lasers in a large variety of fields.

This chapter introduces lasers and their potentiality, focusing on pulsed lasers, that recently are receiving great attention because of their large variety of applications in science and industry. A brief background and theory of pulsed lasers will be given.

Features and state of the art of pulsed laser are introduced, focusing the attention on high repetition rate pulsed lasers and their application.

Finally, the objective of the research is introduced and its roadmap explained in detail. An overview of the chapters is also given.

1.1 Background

1.1.1 Invention of Lasers

Laser (Light Amplification by Stimulated Emission) was considered by its inventor Theodore H. Maiman “a solution seeking a problem” in the early days of its discovery. Past 60 years, now we can confidently state that lasers are one of the most important inventions of the 20th century and our society hugely relies on this technology. It is difficult to image a world without lasers: smartphones, printers and barcode scanners, the internet and live music choreography, we live surrounded by laser technology and will certainly do so in the future. Why are lasers so revolutionary?

Laser is a totally different light source compared to an ordinary light source we normally experience (e.g. sunlight, lightbulb). They are based on different physical phenomena: the first is based on stimulated emission of electromagnetic radiation, while the latter on spontaneous emission. This results in very different light characteristics summarized in the following table:

| LASER light | ORDINARY light |
|------------------------------------|-----------------------|
| Monochromatic | Polychromatic |
| Spatially coherent and directional | Undirectional |
| Polarized | Unpolarized |
| Temporally coherent | Temporally incoherent |

These properties of laser light sources are what made them so successful in a wide range of applications, ranging from medicine to industry, from communication to entertainment and everyday life.

1.1.2 CW laser and pulsed laser

A laser has two modes of operation: continuous and pulsed. In continuous mode operation - known as Continuous Wave (CW) laser – output power is essentially constant over time. In pulsed mode operation, output power takes the form of repetitive light pulses in time (see figure 1.1).

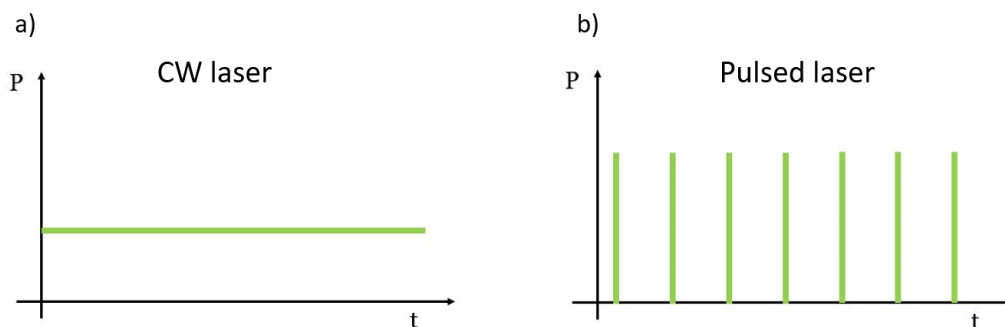


Figure (1.1): (a) CW laser output power in time. (b) Pulsed laser output power in time.

Because of its pulsed nature, the second mode of operation has very convenient features for many applications, that set it apart from CW lasers. These features can be categorized into: ultrashort pulse duration, comb-shaped broad optical spectrum, high peak intensity and high repetition rate. Some of these features tend to be in a trade-off relationship, therefore pulsed lasers usually satisfy only a few of them and are designed accordingly to meet the requirements of a certain application.

Ultrashort pulse duration

Ultrafast pulse lasers are lasers with a pulse output of very short duration, typically in the femtosecond regime. Let's imagine being in a nightclub. Light strobes freeze instants of the surroundings, just like a sequence of pictures. In the same way, ultrafast pulse lasers can freeze instants of the object of your study, allowing therefore fast temporal resolution for investigating chemical-physical phenomena in time domain.

Comb-shaped broad optical spectrum

The Fourier transformation of the output power of an ultrashort pulse laser results in a comb-shaped broad optical spectrum (see figure 1.2). This can be imagined as a spectrum ruler at very high accuracy, where each comb corresponds to a precise frequency.

The field of optical frequency metrology can take large advantages from such "spectral rulers", and they are expected to improve the accuracy of today's atomic clocks. Moreover, they can be used as a novel multi-wavelength light source for dense wavelength division multiplexing (DWDM) in high capacity optical communication.

High peak intensity

At the same output average power, pulsed lasers can achieve higher peak powers compared to CW lasers because the power is concentrated in each pulse. High peak intensity allows non-thermal ablation (i.e. without temperature increase) - a valuable feature in laser surgery and laser manufacturing - and spurs research high-field laser physics.

High repetition rate

Pulsed lasers can have short pulses closely packed to each other in time, with an extremely high rate of light pulses as output, exceeding well beyond gigahertz order.

They are crucial in high-capacity telecommunication systems, optical signal processing and clock distribution. These devices are expected to become key components for the next generation photonics.

Recent developments in pulsed lasers have pushed enormously the frontiers of ultrashort pulse duration, broad optical spectrum, high peak intensity and high repetition rate, reaching regimes that were unthinkable a few decades ago.

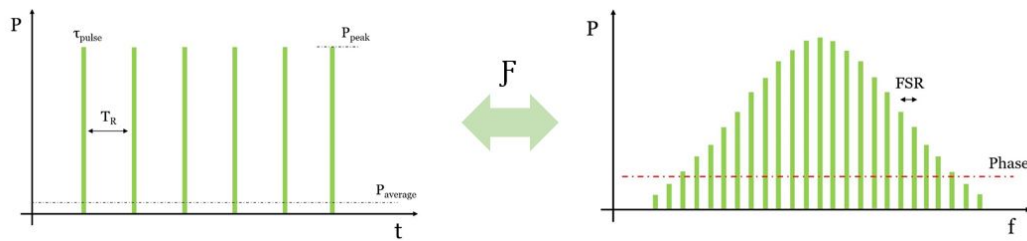


Figure (1.2): Pulsed laser output power in time and its Fourier transform in frequency domain.

The following table summarizes the frontiers of pulsed lasers:

| | |
|------------------------------------|---|
| Ultrashort pulse duration | few femtoseconds (few-cycle regime) [1] |
| Comb-shaped broad optical spectrum | > one octave [1] |
| High peak intensity | Megawatts order [2] |
| High repetition rate | >100 GHz [3] |

1.1.3 Theory of pulsed lasers

A laser is usually composed of a gain medium and a cavity, which provides optical feedback. When pumped, a gain medium can provide optical gain by means of stimulated emission in a given wavelength range - called gain bandwidth. By placing a gain medium inside an optical cavity, light intensity at specific wavelengths that are resonant with the cavity - called longitudinal modes - builds up allowing lasing action by collecting a small fraction of the laser light as the output. However, if the phases of the longitudinal modes are random, noisy CW lasing is obtained. In order to achieve pulsed operation, phase-locking of all the longitudinal modes of the laser is necessary. This pulsed mode of operation is called modelocking (ML), as the modes of the laser are locked in phase. Figure 1.3 illustrates basic principles of modelocking.

Modelocking can be realized actively or passively.

Active modelocking

Active modelocking is usually based on an acousto-optic or electro-optic loss modulator as a loss medium inside the cavity. By modulating the loss of such medium with an external sinusoidal signal, intracavity energy can be concentrated around the minimum of the modulated loss, thus realizing a pulse of light travelling inside the cavity.

It is therefore important to fine tune loss modulation with light cavity roundtrip time in order to realize a modelocked laser. Because the loss modulation is forced externally, this technique also allows harmonic modelocking (HML) - equally spaced multiple pulses inside the cavity - reaching higher repetition rates compared to fundamental modelocking, where only one pulse is travelling inside the cavity.

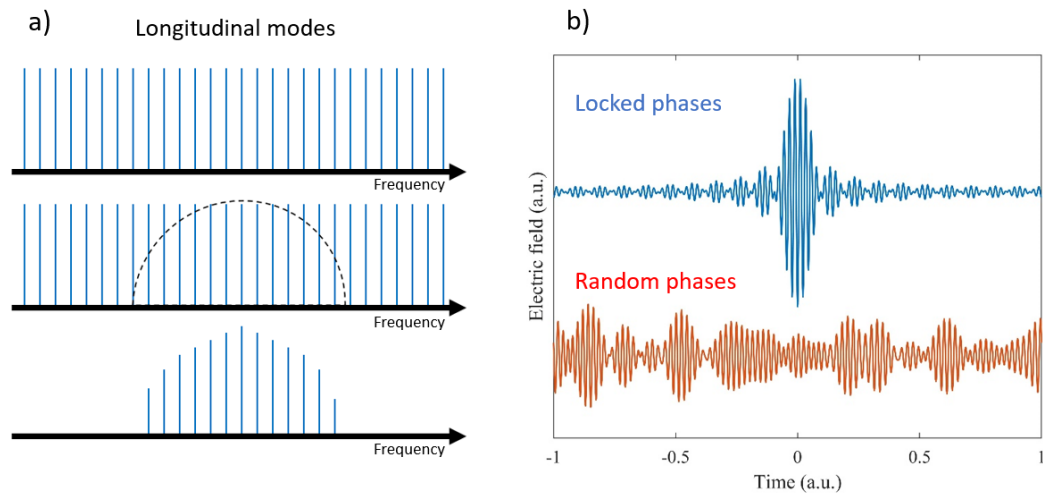


Figure (1.3): (a) Longitudinal modes of resonator that are within the gain bandwidth survive in the cavity. (b) Illustration of electric field with locked and random phases: phase-locking of all longitudinal modes is necessary for pulsed operation.

However, additional power is needed to modulate the loss medium and pulse duration tends to be longer, because of the sinusoidal modulation [4]. Moreover, repetition rate of the laser is limited by the frequency of the external sinusoidal modulation; therefore, if modulation is electronically driven, repetition rate is limited to tens of gigahertz by the electronics.

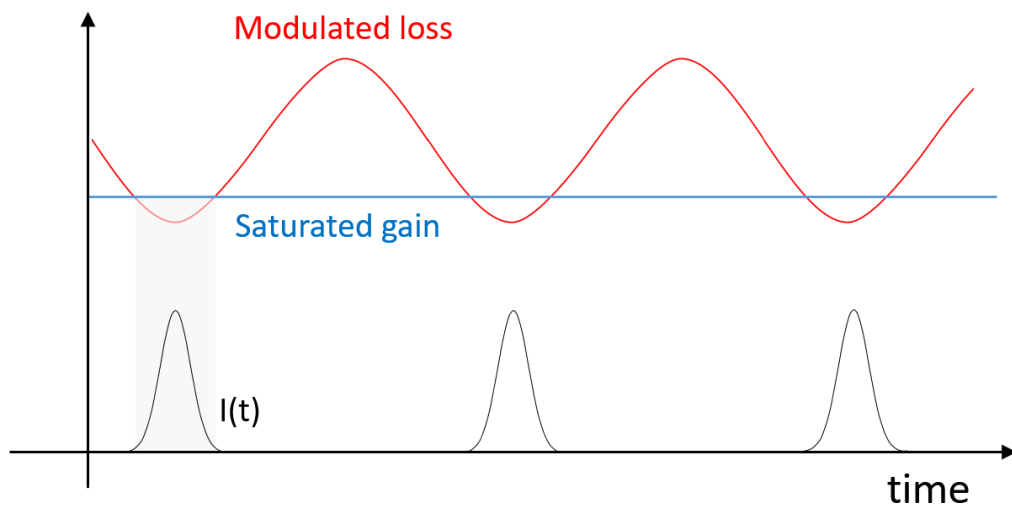


Figure (1.4): Active modelocking: sinusoidally modulated loss allows net gain windows in time, which will host and form pulses.

Passive modelocking

Passive modelocking is obtained without external action, by using a saturable absorber (SA) which causes self-amplitude modulation (SAM) of the light inside the laser cavity. A saturable absorber introduces a nonlinear loss, which is high when light intensity is low, and low when light intensity is high. This is because, while at low light intensities there are plenty of carriers at the ground state that can absorb incoming photons and get excited, at high intensities those carriers are all excited already and photon absorption does not take place. Therefore, in saturable absorbers absorption decreases as light intensity increases.

Although this principle can be applied to all light-absorbing materials, only a handful of materials saturate at conditions that are of practical use and these are called saturable absorbers.

This self-amplitude modulation effect (SAM) is the key for passive modelocking. Passive modelocked lasers start up with noise fluctuations, where a noise peak is increasingly amplified because of its higher intensity, while its wings – at lower intensity – get absorbed. As a result, roundtrip after roundtrip the energy of the cavity is collected around the high intensity noise peak where loss is reduced, and a sharp pulse is originated.

Unlike active modelocking, passive modelocking does not require external power supply for the loss modulator and pulse duration can be shorter, as recovery time of the saturable absorber – the time that it takes for the carries to relax back to ground state – tends to be shorter (femto-picosecond order).

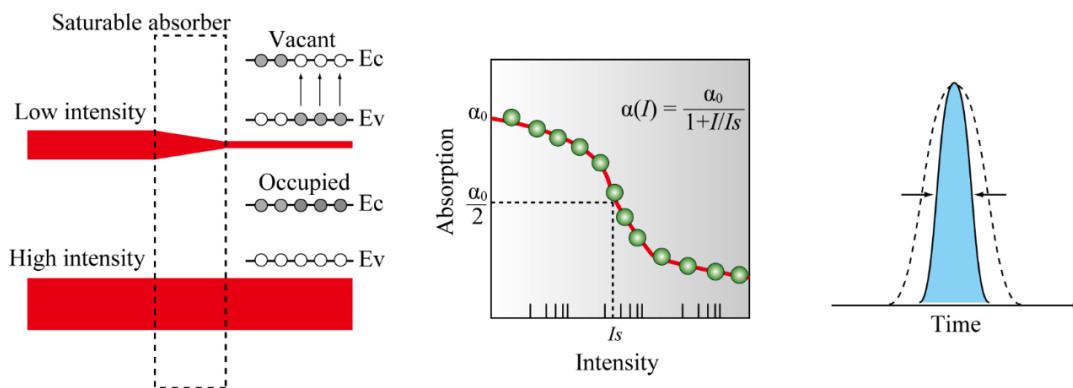


Figure (1.5): Passive modelocking: Working principle of saturable absorbers, where absorption decreases when impinging light intensity increases. This encourages pulse formation by absorbing low intensity tails and leaving untouched high intensity peaks. This image was kindly provided by T. Kumagai.

1.2 High repetition rate modelocked lasers

High repetition rate modelocked lasers (HRR ML lasers) feature pulsed output at Gigahertz rate. As explained in the section 1.1.2, they are a key component of

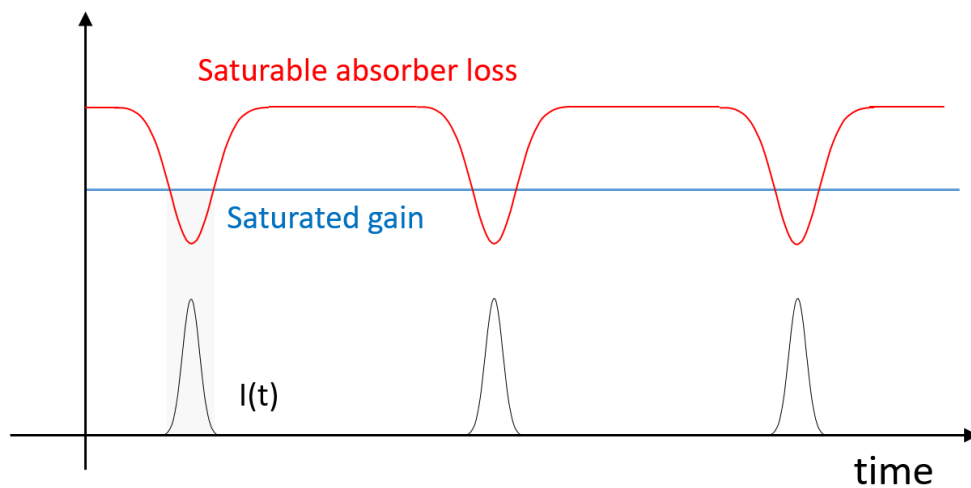


Figure (1.6): *Passive modelocking: nonlinear loss by saturable absorber is introduced in cavity which will allow net gain windows and pulse formation by self-amplitude modulation.*

today's technology and many other fields of application are awaiting to exploit this technology.

1.2.1 Applications

Laser processing

High repetition rate combined with high peak intensity – which can be done externally to the optical cavity – will increase the throughput of modern laser manufacturing by ablation-cooled material removal. Ultrafast successions of laser pulses ablate the target material before the residual heat deposited by previous pulses diffuses away from the processing region. Therefore, this thermal-damage-free method improves the quality of the machining and it increases the efficiency of the laser process compared to traditional laser processing techniques [5].

Laser surgery

Because of its thermal-damage-free characteristic, ablation-cooled material removal by high repetition rate modelocked lasers can be expected to allow non-invasive surgeries without damaging surrounding tissues, such as in delicate dental, eye or brain surgeries [6, 7].

High capacity optical communication

There is an increasing demand of higher capacity optical communication in order to accommodate the rapidly growing data traffic of Internet. High repetition rate modelocked lasers are very attractive for high-speed optical communication techniques, such as Optical Time Domain Multiplexing (OTDM) and soliton-based

communication systems. Moreover, high pulse quality and high signal to noise ratio compared to standard modulated CW sources will allow scaling of the bitrate, while reducing the costs related to the need of the modulator for creating pulses.

Combination of Optical Time Domain Multiplexing (OTDM) and Dense Wavelength Division Multiplexing (DWDM) systems will push the frontiers of optical communication beyond 1Tbit/s [8, 9, 10].

Optical signal processing

Photonic Analog-to-Digital Converters (ADC), optical interconnects in Very Large Scale Integrated (VLSI) microprocessors and photonic networks are all future generation technology that will hugely benefit from high repetition rate modelocked lasers. A high-quality low jitter pulse train at high repetition rates is, in fact, a key component for clock distribution, optical sampling, photonic switching and 3R regeneration (Reamplification, Reshaping, Retiming) [11, 12, 13].

Other applications

LIDAR and remote sensing applications are recently receiving great attention and large investments thanks to the automotive industry and the imminent “Internet of Things”. In this context, they would greatly benefit from high repetition rate modelocked lasers, which allows increased scanning speed and higher resolution, while being eye-safe at 2 μm laser operation wavelength [14, 15, 16].

1.2.2 High repetition rate modelocked laser platforms

Many platforms have been developed to host high repetition rate modelocked lasers. Because of the relationship between repetition rate and cavity length, a short cavity length is necessary to increase repetition rate:

$$\text{Repetition rate} = \frac{c}{nL} \quad (1.1)$$

where c is the speed of light, n the refractive index of the medium and L the cavity length. Therefore the focus of most of these platforms has been to decrease their cavity length without affecting pulse quality. In the following most common high repetition rate lasers platforms are reviewed.

Modelocked bulk lasers

Modelocked bulk lasers typically make use of bulk crystal gain medium, such as Ti:Sapphire or Nd:VO₄, and SESAM as saturable absorber, in order to obtain mode-locking. Typical setup is shown in the figure. By decreasing cavity length, ultra-high repetition rates can be obtained in the GHz regime with a relatively high average output power, thanks to their large effective mode area [17, 18]. By further decreasing the cavity length to microns, 160 GHz repetition rate was obtained by Prof. Ursula Keller, with a Nd:YVO₄ laser modelocked by SESAM [3]. Therefore bulk

lasers are excellent platforms for high repetition pulsed output, with repetition rates that border the limits of the bandwidth of the gain medium itself, but fabrication is complex and expensive, because they rely on free space optics which requires precise alignment and highly controlled environment to operate effectively.

Although there are already products available in the market with a repetition rate of 10GHz with over 1W average output power, they tend to be very expensive and large-scale production and commercialization is difficult as free optics is not suitable for large scale integration.

Modelocked semiconductor lasers

Modelocked semiconductor lasers are the most successful platform nowadays, because of the well developed semiconductor engineering. Although initially laser diodes were employed for this purpose [19], since the invention of VECSELs (Vertical External Cavity Surface Emitting Lasers), research has been progressing towards modelocking this latter devices, because of their higher specifications compared to traditional laser diodes. In fact, VECSELs feature simpler fabrication and testing, higher power at lower current drive, ease of coupling, better spectral characteristics and higher bandwidth. Modelocked VECSELs obtained quickly very high repetition rates above >50 GHz at 100 mW average power [20].

However, modelocked VECSELs required an additional component, a semiconductor saturable absorber mirror (SESAM), increasing the complexity of the setup.

In order to simplify the structure, a novel device was developed by U. Keller at ETH Zürich, named MIXSEL (Modelocked Integrated External Cavity Surface Emitting Laser), where the saturable absorber was introduced in the gain cavity [21]. This solution simplified the structure, allowing to reach even higher repetition rates above 100 GHz at record high output average power of 127 mW [22].

The main challenges related to MIXSELS is the fabrication process, in order not to degrade the saturable absorber, and heat management, which would degrade the properties of the laser [23, 24, 25].

Therefore, nowadays semiconductor modelocked lasers are the most successful and promising platform for high repetition rate lasers, however fabrication is complex and expensive, due to the highly specialized semiconductor technologies – such as bandgap and defect engineering and growth techniques – that need to be employed during their fabrication process. As a matter of fact, commercial products are not yet available.

Modelocked fiber lasers

In recent years, fiber lasers based on optical fibers as waveguides in the cavity, are gaining a lot of attention as laser platforms, compared to bulk lasers, because of their numerous advantages:

- High beam quality

- Alignment free
- Good thermal dissipation
- Simple and cost-effective

Therefore, fiber lasers have been replacing bulk lasers in many applications, both in and outside research laboratories.

In terms of ultrashort pulse duration, high peak power and comb shaped broad optical spectrum, modelocked fiber lasers have approached the performance levels of bulk lasers [26, 27, 28, 29] at lower fabrication complexity and costs – confirming the potentiality of this platform.

However, in terms of high repetition rate, due to the nature of its components, GHz operation is still a challenge. In fact, many fiber components need to be integrated in the cavity – such as isolators, and dispersion-managed fibers – increasing the cavity length, thus limiting the repetition rate below 100MHz [30]. Even trying to decrease cavity length by integrating many components into one single device, repetition rate was limited to 447 MHz and higher repetition rate was not achievable [31].

In 2005, a new all fiber passively modelocked Fabry Perot laser was proposed by S. Yamashita and S. Y. Set of Tokyo University [32]. This device comprises a very short section of highly doped Er:Yb fiber sandwiched with two fiber ferrules coated with highly reflective dielectric mirrors, one of which is coated with a thin layer of carbon nanotubes to provide the saturable absorption required for modelocking.

As a result, sub-picosecond 20 GHz operation was obtained. However, the laser noise and time jitter of the laser was bad and laser stability low, because of the high pump power that was thermally degrading the saturable absorber [33].

Therefore, modelocked fiber lasers are slowly taking over other laser platforms because of their simplicity and cost-effectiveness, but in general repetition rate has been limited by its own structure and higher repetition rate operation above GHz is still a challenge.

Table (1.1): Comparison of most common high repetition rate laser platforms.

| | ML Bulk Laser | Semiconductor ML Laser | ML fiber ring laser |
|-------------------------------|----------------------|-------------------------------|----------------------------|
| Rep. rate | >100 GHz | >100 GHz | <1 GHz |
| Fabrication & Cost | × | × | ○ |
| Integration | × | ○ | ○ |

1.3 Objective of this study

1.3.1 A new laser platform

Whispering Gallery Mode (WGM) microresonators are micrometer size devices that confine light both spatially and temporally by total internal reflection (TIR), allowing strong light-matter interaction.

The phenomenon was originally observed in its acoustic analogy in 1878 by Lord Rayleigh at the St. Paul's Cathedral in London, where whispers against its wall at any point could be heard at any other point around the 34 meters wide gallery. Indeed, acoustic waves travel clinging to the walls, thus decaying in intensity only with the inverse of the distance – rather than the inverse square as in the case of a point source radiating in all directions. This phenomenon involves also the physics of resonance, where only certain pitches survive in the gallery (called modes), when they constructively interfere. Thus, the name “Whispering Gallery Mode”.

The optical counterpart was first proposed in 1939 by Ritchmyer *et al.* [34] and successfully realized in 1989 by Braginsky *et al.* [35], employing a silica microsphere on the top of an optical fiber formed by laser annealing.

The small absorption coefficient of silica and the smooth surface of the microresonator allowed high quality factor in small mode volume. Moreover, silica is one of the most abundant and available materials on earth and it can be well fabricated on Si chips, therefore very low-cost and on-chip integrable.

This and the high temporal and spatial confinement of light are key feature of this microcavity, which opened up possibilities in fundamental physics studies like cavity quantum electrodynamics, nonlinear optics and cavity optomechanics, as well as in applications like optical sensing, communication technology and metrology [36, 37].

Many shapes and materials exist for fabricating WGM microresonators, each of them suitable for different applications and purposes. Example geometries are microspheres, microdisks, microtoroids, microrings and microbottles; example materials are CaF_2 and MgF_2 , LiNbO_3 and BBO, and even some photo-responsive liquid crystalline elastomer [38, 39, 40, 41].

In 2003, a new laser platform has been developed at the California Institute of Technology by K. J. Vahala: a Whispering-Gallery-Mode microlaser [42]. Their device consisted of a whispering gallery mode microresonator gain functionalized by sol-gel process, in order to activate its surface for CW lasing operation.

Thanks to the high Q factor and small mode volume, WGM microresonators are excellent laser platforms for low threshold and narrow linewidth lasers, besides being cost effective and suitable for on chip integration with other optical or electronic functions.

Self-pulsating behavior of WGM microlaser has also been observed at high erbium doping concentrations, producing a pulsed output [43].

This has been attributed to cooperative energy transfer between excited ion-pairs which results in one up-converted ion and one ground state ion, preventing the

population of paired ions from full inversion. As a result, it leads to the reduction of the laser efficiency and increase threshold power, while also drastically changing the dynamic behavior of a laser [44].

However, this self-pulsating operation of a WGM microlaser is not efficient, not stable and not modelocked, thus repetition rate is not fixed by cavity length. In fact, repetition rate was in the MHz range, while if modelocked it should be well above the GHz range, as a microtoroid of 43 μm was used in the experiment.

Because of the complicated integration of the nonlinear loss medium (i.e. saturable absorber) – which provides stable modelocking - no attempts in modelocking a WGM microlaser has been reported in literature.

Instead, many groups have been focusing on soliton generation in undoped WGM microresonators by other means, such as modelocking parametrically driven Kerr frequency combs [37, 45]. These dissipative Kerr solitons do not require saturable absorbers for pulse formation, but they fundamentally differ from traditional solitons, because pump laser is part of soliton spectrum, its power is much larger than its sidebands for parametric gain – therefore a CW background lays beneath the pulse train – and it has to be highly stabilized in frequency for soliton formation. As a result, it needs complicated setup and soliton generation is still a challenge.

Therefore, modelocking an active WGM microresonator by means of saturable absorber, would provide simpler and more stable soliton generation. However, modelocking of a whispering-gallery-mode microlaser has not been reported in literature.

1.3.2 Modelocking of a WGM microlaser

The objective of the research is to modelock a whispering-gallery-mode microlaser.

Because repetition rate scales with the inverse of the size of the cavity, such small resonating structure allows high repetition rate laser operation (table 1.2). Besides having high repetition rate pulsed output, it features small footprint and cost effectiveness, low power consumption and on chip integrability.

The idea behind this device is the miniaturization of a fiber ring laser modelocked by carbon nanotubes as saturable absorber, which has been proved in recent years to be a very simple and easily integrable way to obtain passive modelocking [46, 47, 30, 48].

1.3.3 Research roadmap & Thesis overview

Because of the originality of this work, a careful plan of the steps and results is necessary to reach the goal.

Fabrication-wise an erbium doping technique must be developed in our lab to provide gain medium to the WGM microresonator. Also, a carbon nanotubes integration method has to be conceived, in order to be able to couple the WGM microlaser with a saturable absorber for passive modelocking.

Table (1.2): Diameter and repetition rate relationship ($n=1.44$).

| Diameter (μm) | Repetition rate (GHz) |
|----------------------------|-----------------------|
| 10 | 6630.23 |
| 20 | 3315.115 |
| 30 | 2210.077 |
| 40 | 1657.557 |
| 50 | 1326.046 |
| 80 | 828.7787 |
| 100 | 663.023 |
| 200 | 331.5115 |
| 300 | 221.0077 |
| 400 | 165.7557 |
| 500 | 132.6046 |
| 800 | 82.87787 |
| 1000 | 66.3023 |

A model has to be created and calculations performed, in order to design the WGM microcavity in a way that it can host modelocking behavior.

Finally, experimental techniques for evaluating gain, nonlinear loss and dispersion of a WGM microlaser are needed to characterize the microcavity and link fabrication and design, allowing further optimization of the device.

1. Fabrication

- Er-doping technique
- CNT integration method

2. Design

- Modeling WGM modelocked microlaser
- Modelocking regime investigation

3. Evaluation

- Gain, nonlinear loss, dispersion characterization

By working through these three steps, the goal of modelocking a WGM microlaser can be achieved in a systematic way, and further optimization is possible.

This thesis focuses on the fabrication and the design of the modelocked WGM microlaser, providing the basic tools and methods to obtain a WGM microlaser operating in modelocking regime.

Chapter 2 presents the basic theory and fundamental features of whispering-gallery-mode microresonators and microlasers, also describing their fabrication methods.

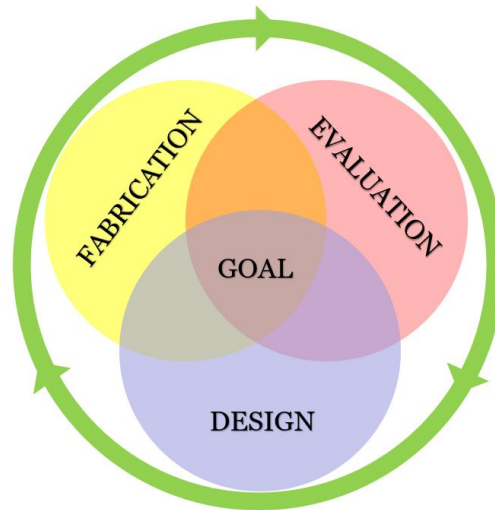


Figure (1.7): Necessary stages and workflow of research to achieve the goal.

Chapter 3 introduces carbon nanotubes as saturable absorbers and then gives an overview on CNT integration methods. Two methods of integration based on optical deposition are described in details. Their advantages and drawbacks are explained and saturable absorption properties evaluated.

Chapter 4 focuses on the creation of a reliable simulation model, by first modeling an Er-doped fiber laser modelocked by CNT that was realized in the lab for this purpose. Experimental results are compared with simulation results and reliability of the model is verified in view of its miniaturization.

Chapter 5 investigates modelocking regime for a WGM microlaser with saturable absorber. Also, a design strategy is proposed.

Chapter 6 summarizes the work and gives an outlook on the future work and possibilities.

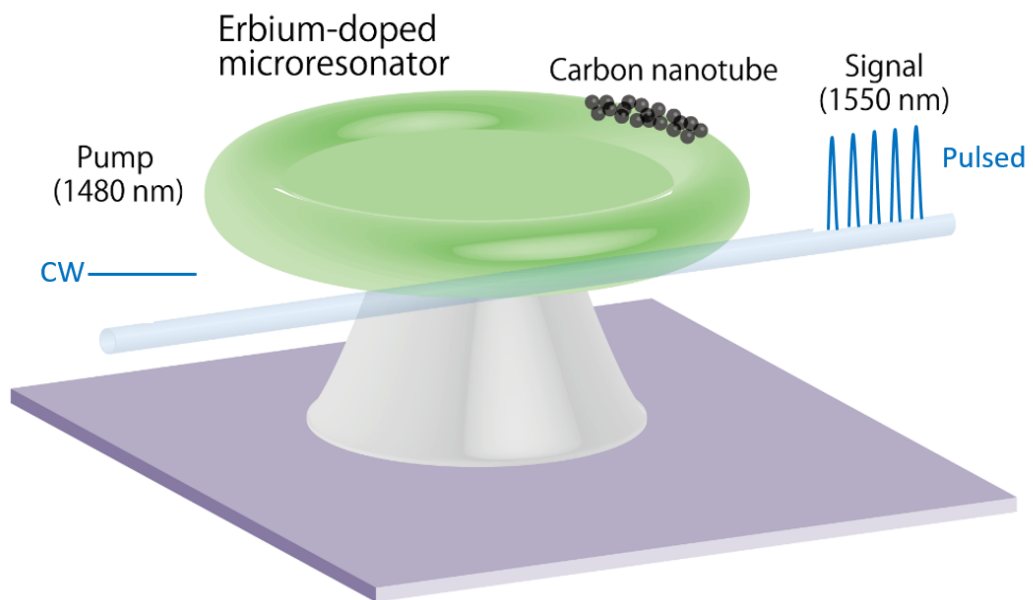


Figure (1.8): Illustration of WGM microlaser modelocked by carbon nanotubes as saturable absorber. Original image was kindly provided by S. Fujii.

Chapter 2

WGM microresonator

Whispering-gallery-mode (WGM) microresonators are micrometer size devices that confine light both spatially and temporally by total internal reflection (TIR), allowing strong light-matter interaction. Since their discovery in 1989, they have been widely employed in fundamental physics studies of nonlinear optical phenomena, as well as new technologies for sensing, metrology and optical communication.

WGM microresonators come in many shapes and materials, but in this thesis I will focus on silica WGM microspheres and silica WGM microtoroids, which can be fabricated in our lab and exhibit low light absorption while the latter being on-chip integrable.

In the following sections, I will give an overview on WGM microresonators, describing its parameters, fabrication process and characterization method. Then, I will introduce WGM microlasers – active WGM microresonators doped with gain material – and their CW lasing properties are evaluated.

For compactness, equations and simulations derived in the following sections are referred to a WGM microtoroid, however in principle they can be applied to other WGM microresonators with appropriate adjustments.

2.1 Q factor

High Q factor is essential in WGM microresonators. High Q factor means that light is trapped for a long time (ns~ μ s) inside the microresonator because of the low light absorption and scattering.

In general, Q factor indicates the extent of dissipation of a resonant system [49]:

$$Q = \omega_r \frac{\text{stored energy}}{\text{power dissipation}} \quad (2.1)$$

where ω_r is the angular frequency of the resonance.

Q factor is also related to the photon lifetime, its decay rate and the linewidth of the resonance:

$$Q = \omega_r \tau_{ph} = \frac{\omega_r}{k} = \frac{\nu_r}{\Delta\nu} \quad (2.2)$$

where τ_{ph} is the photon lifetime, k is the decay rate, ν_r is the frequency of the resonance and $\Delta\nu$ is the full-width-half-maximum (FWHM) of the resonance frequency linewidth. Related values of Q , τ_{ph} , $\Delta\nu$ and wavelength linewidth $\Delta\lambda$ at 1550 nm are shown in the table 2.1.

Table (2.1): Relationship between Q , $\Delta\nu$, $\Delta\lambda$, τ_{ph} at 1550 nm.

| Q | $\Delta\nu$ | $\Delta\lambda$ | τ_{ph} |
|----------------|-------------|-----------------|---------------|
| $1 \cdot 10^6$ | 193.4 MHz | 1.55 pm | 0.823 ns |
| $2 \cdot 10^6$ | 96.71 MHz | 0.775 pm | 1.647 ns |
| $1 \cdot 10^7$ | 19.34 MHz | 0.155 pm | 8.23 ns |
| $2 \cdot 10^7$ | 9.671 MHz | 77.5 fm | 16.47 ns |
| $1 \cdot 10^8$ | 1.934 MHz | 15.5 fm | 82.3 ns |
| $2 \cdot 10^8$ | 967.1 kHz | 7.55 fm | 164.7 ns |
| $1 \cdot 10^9$ | 193.4 kHz | 1.55 fm | 0.823 μ s |
| $2 \cdot 10^9$ | 96.71 kHz | 0.775 fm | 1.647 μ s |

In WGM microresonators, there are different causes that limit Q factor, such as material absorption loss, surface scattering loss, coupling loss and so on. Therefore, total Q is

$$Q_{total}^{-1} = Q_{material}^{-1} + Q_{scattering}^{-1} + Q_{couple}^{-1} + \dots \quad (2.3)$$

Note that total Q is limited by the lowest Q factor, therefore the largest loss.

Figure 2.1 categorizes losses in WGM microresonators. They are divided into two main categorizes: intrinsic loss – losses that are solely dependent on the characteristics of the device – and extrinsic loss – losses caused by perturbation of external components such as waveguides. Material absorption loss and surface scattering loss are intrinsic loss, while coupling loss is extrinsic loss.

If Q factor is given by material absorption, it can be calculated as:

$$Q = \frac{2\pi n}{\alpha\lambda_r} \quad (2.4)$$

where n is the refractive index, α is the absorption loss and λ_r is the resonance wavelength.

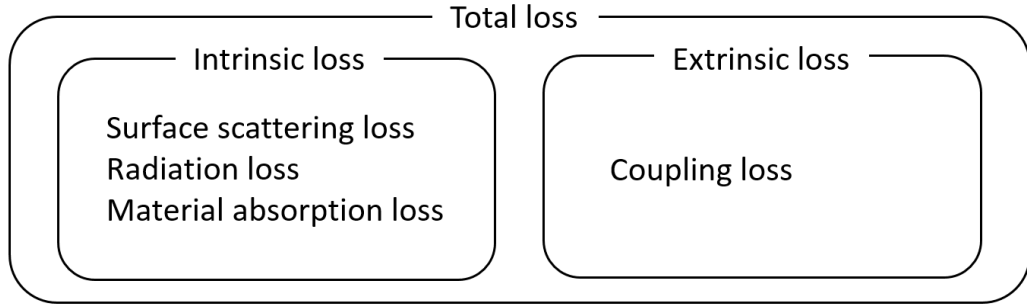


Figure (2.1): Categorization of losses in WGM microresonators.

2.2 Optical modes in WGM microresonators

2.2.1 Whispering-gallery modes

WGM microresonators are essentially optical resonators, therefore they possess resonant wavelengths and frequencies that can be trivially obtained by setting the condition of resonance where a frequency has to have same phase after one roundtrip to reinforce its oscillation:

$$m\lambda_m = 2\pi nR \quad (2.5)$$

$$\nu_m = \frac{mc}{2\pi nR} \quad (2.6)$$

where n is the refractive index, R is the radius of the optical microresonator and m is the mode number.

From equation 2.6 we can see that a WGM microresonator has equidistantly spaced resonance frequencies and its Free Spectral Range (FSR) is:

$$\nu_m = \frac{c}{2\pi nR} \quad (2.7)$$

FSR gives us information about the frequency distance between two adjacent resonances.

Because of its definition, FSR is also an indicator of the cavity roundtrip time T_r - the time that it takes for the light to travel one roundtrip inside the microcavity:

$$T_r = FSR^{-1} = \frac{2\pi nR}{c} \quad (2.8)$$

Figure 2.2, summarizes these basic properties of a WGM microresonator.

For a more detailed analysis of the modes inside a WGM microresonator, it is necessary to rely on the scalar wave equation for propagation in a dielectric medium

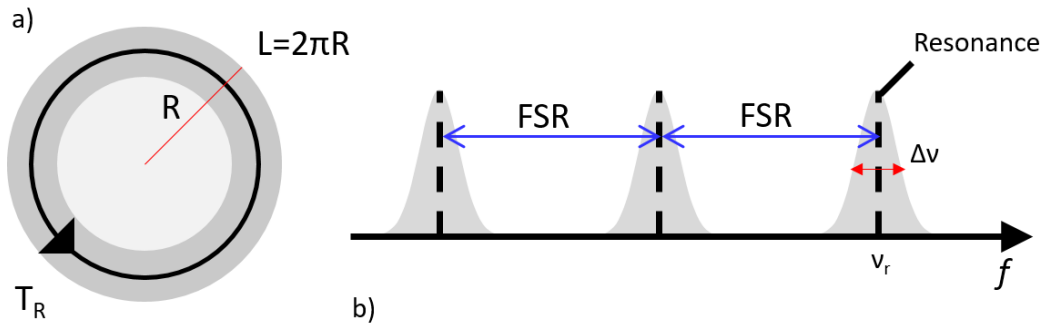


Figure (2.2): (a) Geometrical properties of WGM microresonators. (b) Basic WGM microresonator properties visualized in frequency domain. Grey areas indicate its resonances.

– known as Helmholtz equation - retrieved from Maxwell's equations in an isotropic charge free medium [49]:

$$(\nabla^2 + \frac{\omega^2 n^2}{c^2})E = 0 \quad (2.9)$$

Because of the cylindrical symmetry of microtoroid structure, the electric field can be written as:

$$E(r, \phi, z, t) = \text{Re}[E(r, \phi, z)e^{i\omega t}] \quad (2.10)$$

where r is the radial direction, ϕ is the azimuthal direction and z is the vertical direction in cylindrical coordinates (see figure 2.3).

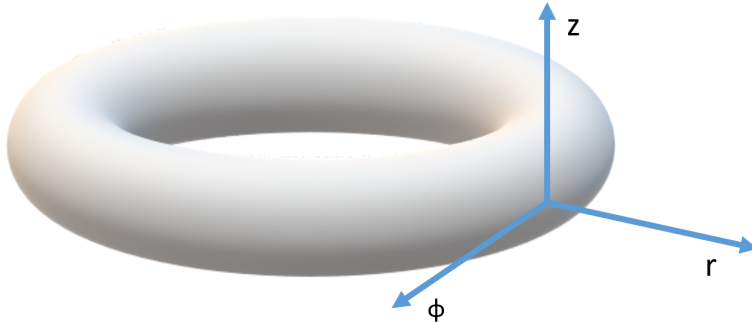


Figure (2.3): Cylindrical coordinates in WGM microtoroid.

The solutions to the equation 2.9, have either transverse-electric (TE) or transverse-magnetic (TM) polarization in the cavity. In TE modes, electric field oscillates in the (r, z) plane, transverse to the propagation direction along ϕ , thus $E_\phi = 0$. On the contrary, in TM modes the magnetic field oscillates in the (r, z) plane and thus $H_\phi = 0$. The remaining field components can be expressed with only one field component: H_ϕ for TE mode and E_ϕ for TM mode. Equation 2.9 is then reduced to a scalar Helmholtz equation with one field component.

Therefore, TE mode and TM mode can be respectively expressed as:

$$H_\phi = H_\phi(r, z)e^{\pm il\phi} \quad (2.11)$$

$$E_\phi = E_\phi(r, z)e^{\pm il\phi} \quad (2.12)$$

where l is the angular mode number.

By expanding the Laplacian operator of equation 2.9, Helmholtz equation reduces to:

$$\left[\frac{\partial^2}{\partial r^2} + \frac{\partial}{r\partial r} - \frac{l^2}{r^2} + \frac{\partial^2}{\partial z^2} + \frac{\omega^2 n^2}{c^2} \right] E_\phi(r, z) = 0 \quad (2.13)$$

Because of the complicated form of the partial differential equation, numerical calculation with finite-element method (FEM) is usually used to analyze the spatial mode profile of silica WGM microtoroids. Figure 2.3(a)-(b)-(d) shows the numerical results with COMSOL Multiphysics for TE fundamental mode and its intensity distribution in the radial direction. Figure 2.3(c) shows an example of higher order whispering gallery mode.

TE fundamental modes are the focus of this thesis, as they exhibit higher Q factors than TM modes due to their weaker light leakage and possess minimum effective mode area, thus confining light better spatially.

2.2.2 Effective mode area

Effective mode area A_{eff} measures the cross section area occupied by an optical mode in a WGM microresonator. It is related to the effective mode volume – volume occupied by an optical mode – by $V_{eff} \sim L_{cavity} A_{eff}$.

It can be calculated by:

$$A_{eff} = \frac{\left(\iint |E(r, z)|^2 dx dy \right)^2}{\iint |E(r, z)|^4 dx dy} \quad (2.14)$$

Figure 2.5 shows COMSOL Multiphysics calculation results for TE fundamental mode of a WGM microtoroid at different minor and major diameters. Increase in major and minor diameters induces larger effective mode areas.

2.2.3 Evanescent field

As it can be seen in figure 2.5, there is light leakage outside the boundaries of the WGM microresonator. This is called evanescent field and that is what makes this device interesting practically. Evanescent field is sensitive to the surroundings, therefore it allows coupling light in and out through waveguides [50, 51], sensing environment (e.g. temperature and gases) [52, 53, 36, 54], and perturbing or investigating the properties of light inside the WGM microresonator [55].

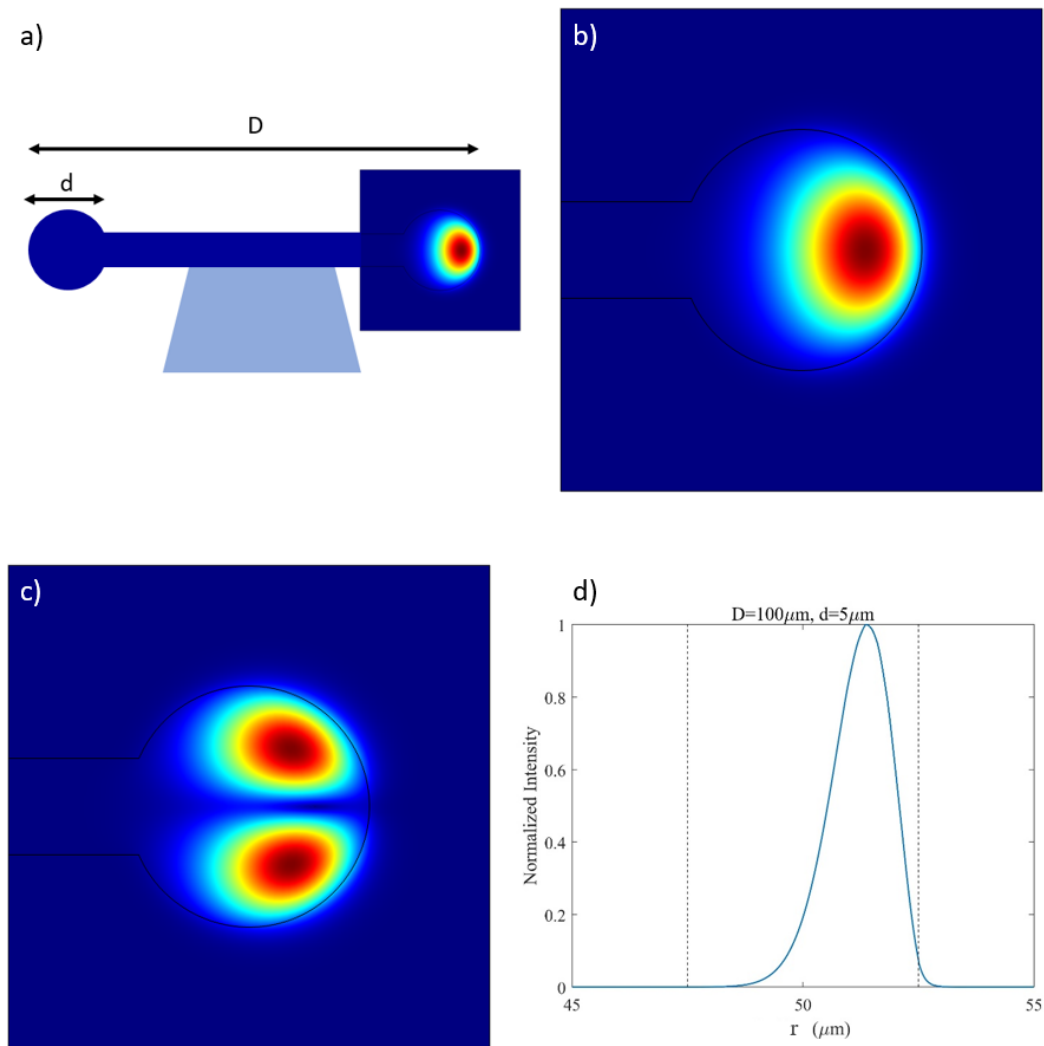


Figure (2.4): (a) Illustration of simulated WGM microresonator's structure: D is major diameter and d is minor diameter. (b) COMSOL Multiphysics calculation result for TE fundamental mode. (c) Example of a higher order whispering gallery mode. (d) Intensity distribution of TE fundamental mode in radial direction. Dashed lines indicate boundaries of WGM microtoroid.

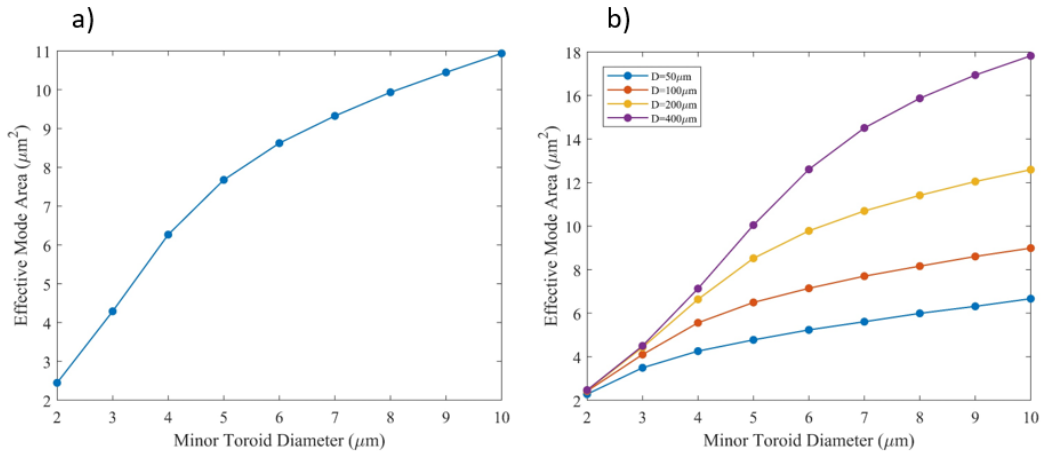


Figure (2.5): (a) COMSOL Multiphysics calculation results of effective mode area of TE fundamental mode for WGM microtoroids at different minor diameters. Major diameter is fixed to $150 \mu\text{m}$. (b) Results for other major diameters ($50 \mu\text{m}$, $100 \mu\text{m}$, $200 \mu\text{m}$, $400 \mu\text{m}$).

Evanescent field ratio – ratio between leaked power and total power – is determined by:

$$\text{Evanescent field ratio} = \frac{\iint_{\text{clad}} |E(r, z)|^2 dx dy}{\iint_{\text{tot}} |E(r, z)|^2 dx dy} \quad (2.15)$$

Figure 2.6 shows COMSOL Multiphysics calculation result of the evanescent field ratio of WGM microtoroids at different major and minor diameters. With increasing minor and major diameters, light is more and more confined inside the cavity and evanescent field ratio decreases.

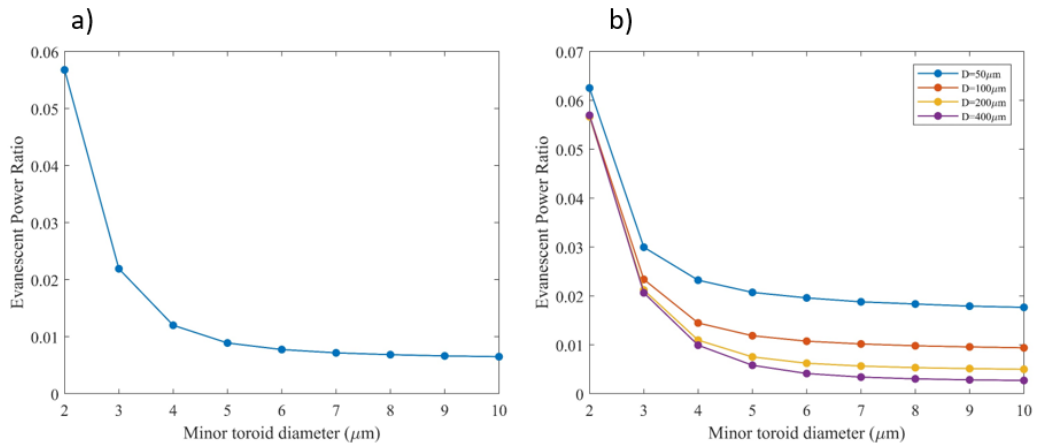


Figure (2.6): (a) COMSOL Multiphysics calculation results of evanescent field ratio of TE fundamental mode for WGM microtoroids at different minor diameters. Major diameter is fixed to $150 \mu\text{m}$. (b) Results for other major diameters ($50 \mu\text{m}$, $100 \mu\text{m}$, $200 \mu\text{m}$, $400 \mu\text{m}$).

2.2.4 Dispersion in WGM microresonators

Dispersion is a key parameter to engineer in not only fiber lasers, but also WGM microresonators. While it allows soliton modelocking in fiber lasers, careful engineering of dispersion allows microcomb and soliton generation in WGM microresonators. Therefore, dispersion effects in optical modes need to be controlled.

In absence of dispersion, resonant frequencies are equidistant by a FSR, as explained in the section 2.2.1. However, because of the frequency-dependent nature of refractive index (chromatic dispersion) and different light paths (geometric dispersion) speed of light is different for different frequencies. Therefore, resonant frequencies are not expressed anymore only in terms of FSR, but with a Taylor-expanded equation with correction terms that take into account chromatic and geometric dispersion (see figure 2.7) [56]:

$$\omega_\mu = \omega_0 + D_1\mu + \frac{1}{2}D_2\mu^2 + \frac{1}{6}D_3\mu^3 + \dots \quad (2.16)$$

where $\frac{D_1}{2\pi}$ is cavity FSR, $\frac{D_2}{2\pi}$ and $\frac{D_3}{2\pi}$ are second and third order dispersion, respectively. Second-order dispersion parameter D_2 is typically larger than D_3 ($D_2 \gg D_3$) and it is related to the group velocity dispersion (GVD) β_2 by:

$$D_2 = -\frac{c}{n}D_1^2\beta_2 \quad (2.17)$$

Positive (negative) D_2 and negative (positive) β_2 determine anomalous (normal) dispersion.

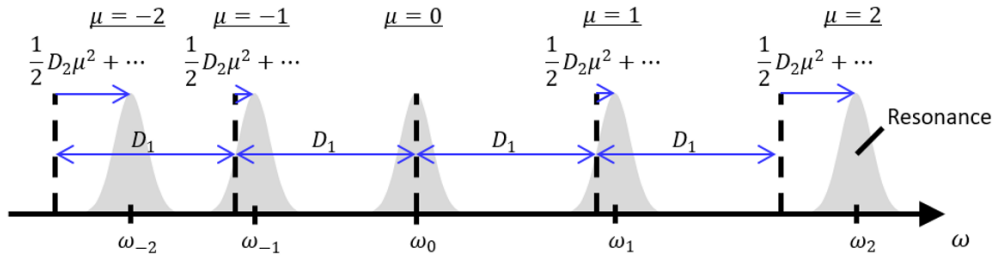


Figure (2.7): Illustration of dispersion effects on resonances in WGM microresonators, based on equation 2.16. In this case, anomalous dispersion ($D_2 > 0$) is responsible for the resonance shift.

From equation 2.16, it is clear that by measuring the resonant frequencies of a WGM microresonator it is possible to quantify D_2 and β_2 , thus the dispersion of that specific WGM microresonator. In figure 2.8, calculation results are given for the dispersion (in terms of β_2) at different wavelengths for a WGM microtoroid with different major diameters.

Therefore, by finely tuning cavity diameter, it is possible to engineer dispersion of the cavity in order to achieve microcomb generation and soliton modelocking [45, 37].

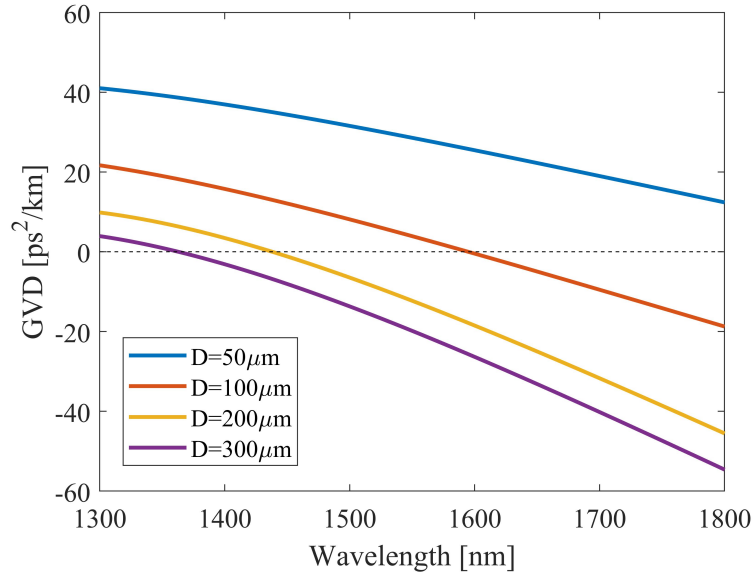


Figure (2.8): COMSOL Multiphysics calculation results of dispersion β_2 at different wavelengths for a WGM microtoroid with different major diameters. Minor diameter is 8 μm .

2.3 Fabrication of WGM microresonators

2.3.1 Silica WGM microsphere

WGM microspheres were first fabricated in 1989 by Braginsky *et al.* [35] by laser annealing. They feature high Q factor with smooth surface.

Fabrication of a WGM microsphere is relatively simple from a standard single mode fiber by CO₂ laser reflow or arch discharge method. Figure 2.9 shows fabricated WGM microspheres with different diameters.

2.3.2 Silica WGM microtoroid

While WGM microspheres are useful for laboratory demonstration, they are not suitable for large scale integration, because their properties cannot be controlled well during fabrication. On the other side, WGM microtoroids are on-chip integrable and their properties are more easily controlled during fabrication. This makes them suitable candidates for large scale integration. Besides being on-chip integrable, they have high Q factor (100 million) and small mode volume.

Silica WGM microtoroid were first developed in 2003 at California Institute of Technology by Armani *et al.* [41]. Figure 2.10 shows the fabrication process.

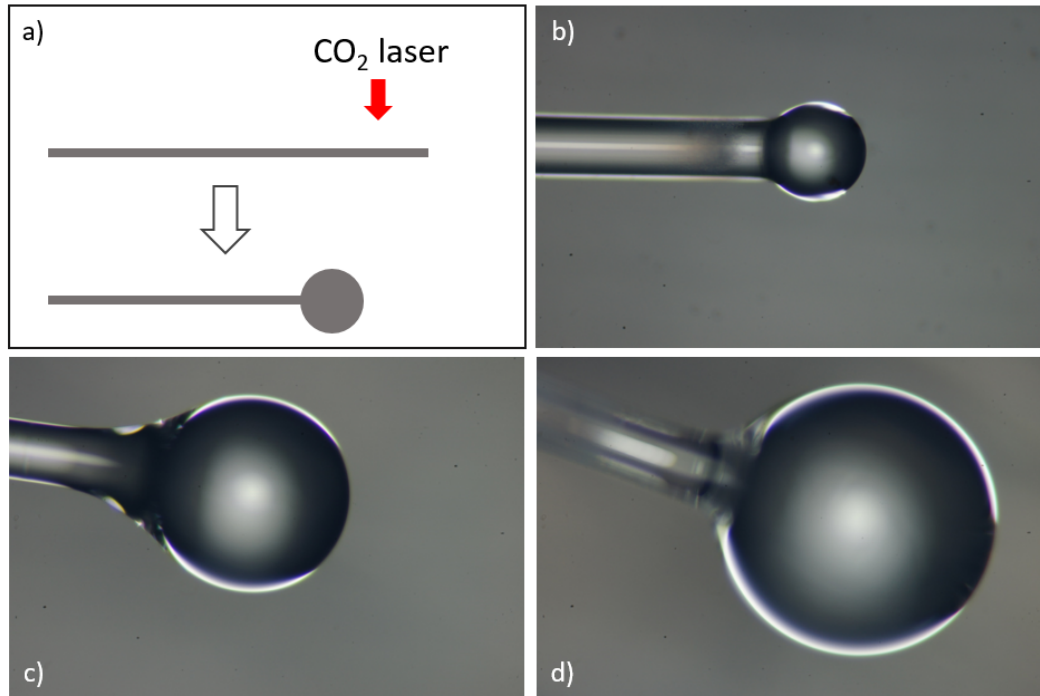


Figure (2.9): (a) Schematics of silica WGM microsphere fabrication by CO₂ laser reflow. (b)-(c)-(d) are examples of fabricated silica microspheres with diameters of approximately 200 μm, 400 μm, 600 μm.

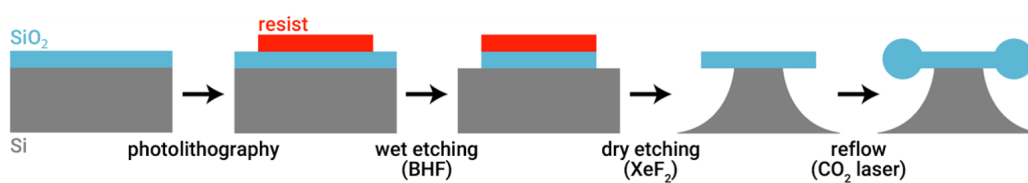


Figure (2.10): (a) Fabrication process of silica WGM microtoroid.

First, a silicon wafer with a silica layer of $2\ \mu\text{m}$ is prepared, then by photolithography and silica etching with buffered hydrogen fluoride (HF), circular silica disks on silicon are realized. Diameters are typically from $50\ \mu\text{m}$ to $200\ \mu\text{m}$. Silicon etching with XeF_2 creates a silica disk on top a silicon pillar, which can already confine light in whispering-gallery modes at the edges of the disk. In order to further smooth the surface of the resonator, CO_2 laser beam is focused on this silica disk from the top, melting only the edges of the silica disk, because the silicon pillar works as a heat tank. Thus, a toroidal shape with smooth surface is realized and usually Q factor improves by two orders of magnitude by laser reflow (see figure 2.11).

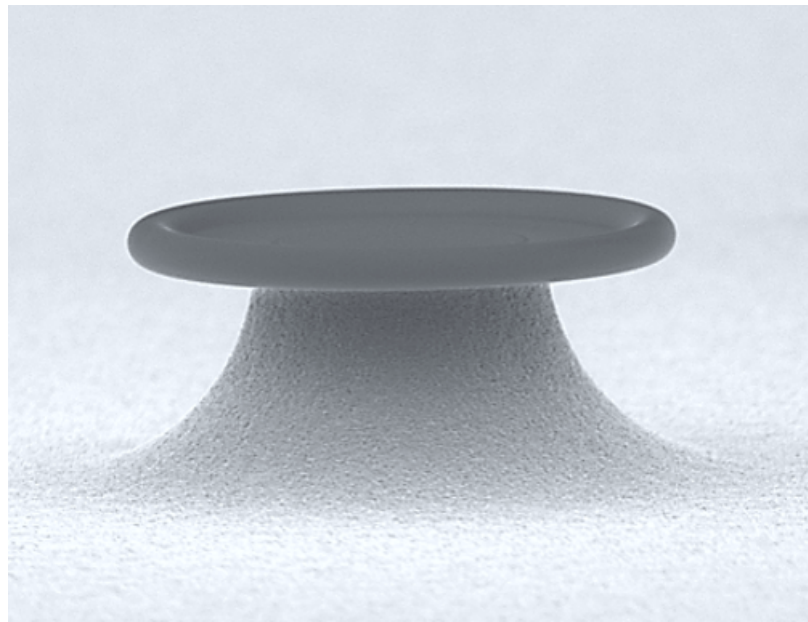


Figure (2.11): (a) SEM image of a silica WGM microtoroid. The image was kindly provided by R. Suzuki.

2.4 Coupling light in WGM microresonators

There are different ways for coupling light into a WGM microresonator: optical tapered fibers, pig-tailed fibers, prisms and on-chip waveguides. Optical tapered fibers are the most commonly used method for coupling light via evanescent field into WGM microspheres and WGM microtoroids, because of their simple fabrication, high coupling coefficient ($>99\%$) and no need for free-space alignment.

2.4.1 Optical tapered fiber

Optical tapered fiber are micrometer thin fibers with strong evanescent field leakage, which allows excitation of whispering gallery modes in microresonators. They are fabricated by flame-brushing technique, where a conventional $125\ \mu\text{m}$ optical fiber is stretched while heating, until a diameter of approximately $1\ \mu\text{m}$ is obtained.

During the fabrication process, the optical fiber experience many propagation modes (multi-mode condition), but eventually it satisfies the single mode condition given as:

$$V_{fiber} = \frac{2\pi n_1 a}{\lambda_0} \sqrt{2 \frac{n_1^2 - n_2^2}{n_1^2}} < 2.405 \quad (2.18)$$

$$a < 0.57$$

where a is the radius of the tapered fiber, $\lambda_0 = 1.55\mu m$, $n_1 = 1.44$ (fused silica), $n_2 = 1$ (air). Figure 2.12(a) shows flame-brushing fabrication setup, while monitored transmission in time is shown in figure 2.12(b), revealing multi-mode and single-mode operation of tapered fiber during fabrication process. Figures 2.12(c)-(d) are COMSOL Multiphysics calculation results that quantify the effective mode area of tapered fibers with different diameters and their evanescent field ratio.

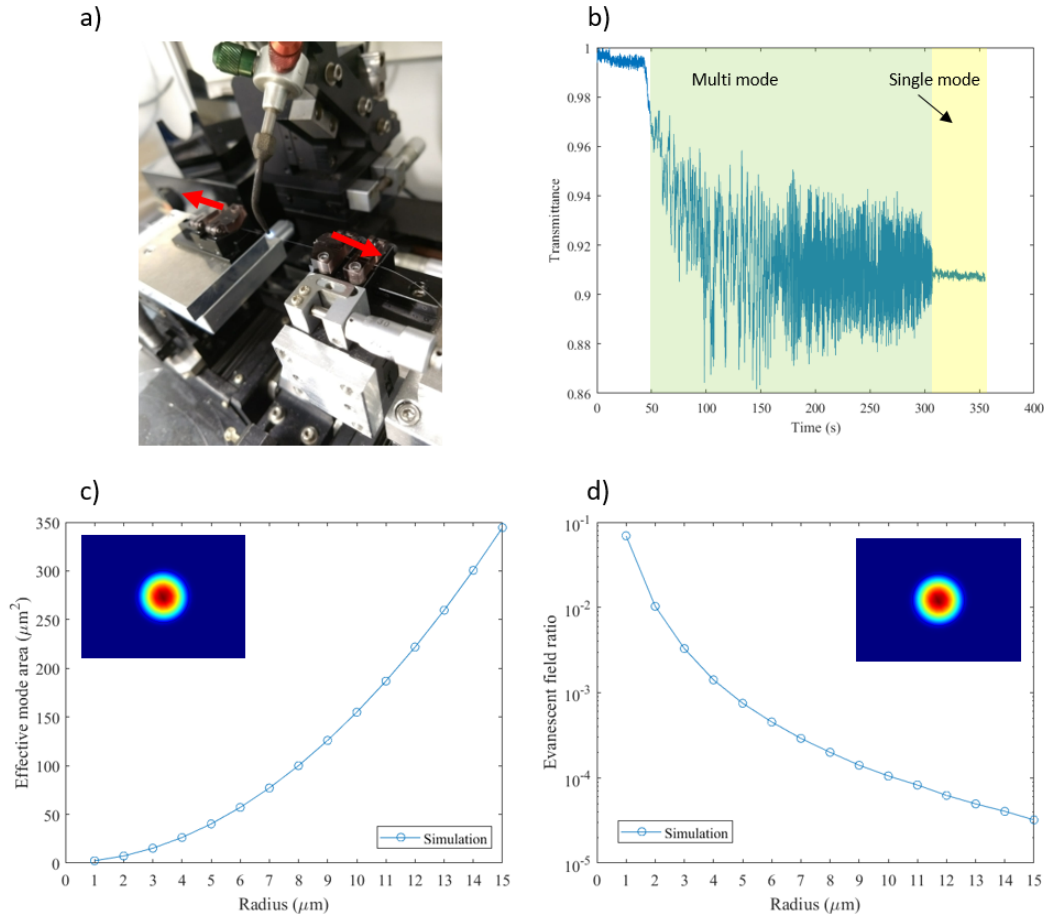


Figure (2.12): (a) shows the fabrication setup to realize tapered fibers by flame brushing technique. (b) Transmission of tapered fiber during its fabrication process reveals multi-mode and single-mode operation. (c) COMSOL Multiphysics calculation results of effective mode area for single mode tapered fiber with different diameters. (d) COMSOL Multiphysics calculation results of evanescent field ratio for single mode tapered fiber with different diameters.

2.4.2 Coupling mode theory

Coupled Mode Theory (CMT) [57] can be used to study light coupling in WGM microresonators. Light field $a_0(t)$ – normalized so that $|a_0(t)|^2$ corresponds to the intracavity energy - can be expressed as:

$$\frac{da_0(t)}{dt} = -\frac{k}{2}a_0(t) + i(\omega_p - \omega_0)a_0(t) + \sqrt{k_{ext}}s_{in}(t) \quad (2.19)$$

where $k = k_{int} + k_{ext}$ is total decay rate, ω_p and ω_0 are pump and resonance frequency respectively and $s_{in}(t)$ is the input field - normalized to $|s_{in}^2(t)|$ as its power.

In steady-state condition, equation 2.18 becomes:

$$a_0 = \frac{\sqrt{k_{ext}}}{\frac{1}{2}k - \Delta\omega_0} s_{in} \quad (2.20)$$

$$|a_0|^2 = \frac{k_{ext}}{\frac{1}{4}k^2 + \Delta\omega_0^2} |s_{in}|^2 \quad (2.21)$$

where $\Delta\omega_0 = \omega_p - \omega_0$ is the detuning of the pump with respect to resonant frequency.

Output field $s_{out}(t)$ is given by

$$s_{out}(t) = \sqrt{k_{ext}}a_0(t) - s_{in}(t) \quad (2.22)$$

Therefore, by rearranging equation 2.21 and equation 2.22 transmittance can be calculated as:

$$T = \left| \frac{s_{out}}{s_{in}} \right|^2 = \frac{\frac{1}{4}(k_{ext} - k_{in})^2 + \Delta\omega_0^2}{\frac{1}{4}(k_{ext} + k_{in})^2 + \Delta\omega_0^2} \quad (2.23)$$

When detuning is set to zero, from equation 2.23 three coupling conditions can be inferred:

- Under coupling ($k_{int} > k_{ext}$): in this case, coupling rate is smaller than the intrinsic decay rate. Hence, light coupling into the microcavity is small and total Q factor is merely determined by its intrinsic losses and it is highest.
- Critical coupling ($k_{int} = k_{ext}$): here, coupling rate matches the intrinsic decay rate. Transmittance falls to zero, therefore all light is coupled into the cavity.
- Over coupling ($k_{int} < k_{ext}$): in this case, coupling rate is larger than the intrinsic decay rate. Light coupling into the microcavity is large and total Q factor is also affected by extrinsic losses and it decreases.

Figure 2.13(a) shows the transmittance and total Q factor normalized by its intrinsic Q, against the coupling parameter $\frac{k_{int}}{k_{ext}}$. As mentioned above, three coupling conditions can be inferred. Figure 2.13(b) shows the experimental results, which match well with calculated results. In this case, because of the difficulty in measuring coupling parameter, the distance (gap) between tapered fiber and WGM microtoroid is used as a measure of coupling.

Also, from coupled mode theory, cavity build-up factor can be determined. That is the ratio between intracavity power and input power, which is greatly enhanced in high-Q WGM microresonators.

In case of critical coupling and zero detuning, cavity build-up factor can be expressed as:

$$\text{Build-up factor} = \frac{P_{cav}}{P_{in}} = \frac{Q\lambda}{2\pi L} \quad (2.24)$$

For example, for a WGM microresonator of diameter $100\ \mu\text{m}$ and Q factor of 10^7 at $1550\ \text{nm}$, intracavity power is 7860 times input power.

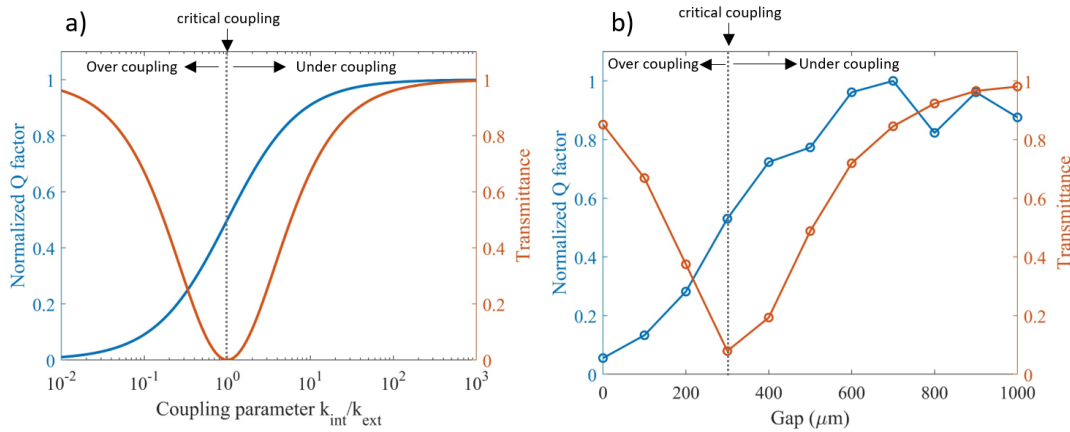


Figure (2.13): (a) Numerical calculation of transmittance and total Q factor normalized by its intrinsic Q factor against coupling parameter $\frac{k_{int}}{k_{ext}}$. (b) Experimental results for the transmittance and normalized Q factor with WGM microresonator-tapered fiber gap, which accounts for the coupling parameter. Theoretically derived coupling regimes can be observed.

2.4.3 Q factor measurement

In order to evaluate Q factor of WGM microresonators, the setup shown in figure 2.14(a) is used. A tunable laser diode (Santec TSL-710) and polarization controller are used to couple light into a WGM microresonator via a tapered fiber. A power meter measures transmission spectrum, as the laser sweeps its wavelength across the resonance. As a result the spectrum in figure 2.14(b)-(c) is obtained. By fitting such spectrum, Q factor of WGM microresonator can be retrieved.

2.5 Active WGM microresonator

Because of their large Q factor to mode volume ratio Q/V – which results in strong light-matter coupling – WGM microresonators are excellent platforms for realizing low threshold and narrow linewidth lasers [58, 59] – often called WGM microlasers.

These on-chip integrable light sources have many potential applications in sensing, optical communication and integrated photonics.

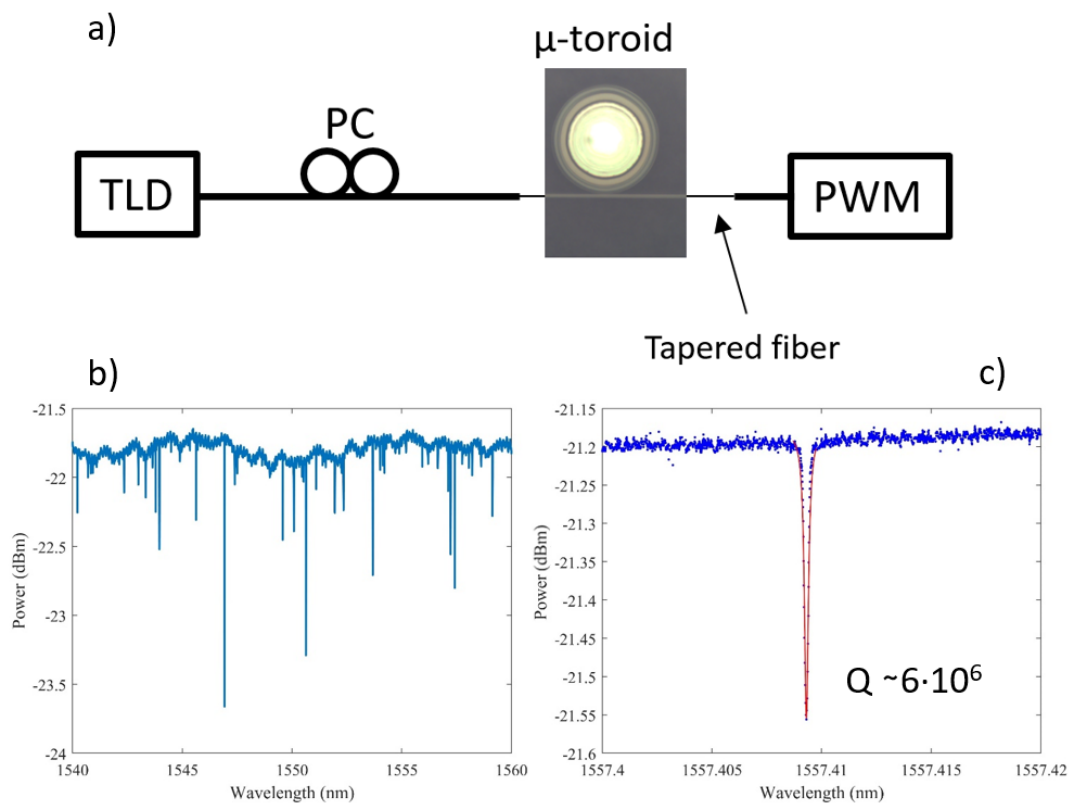


Figure (2.14): (a) Experimental setup for Q factor measurement of WGM microresonators. (b)-(c) Typical spectrum from Q factor measurement setup (taken from different experiments). By fitting such spectrum, Q factor can be derived.

Doping high Q microresonators with different gain materials gives the possibility to access different corners of the spectrum - from ultraviolet to infrared. Among different active materials, rare-earth ions – such like Er^{3+} , Yb^{3+} , Nd^{3+} - are popular dopants in laser industry because of their high efficiency, long upper-state lifetime and wide emission spectrum. They cover wavelengths fundamental to many sensing and communication applications: in particular, Er^{3+} ions provide gain in C-band, hence becoming key dopant for optical communication applications.

In the following sections, two types of WGM microlasers are studied - Er-doped microsphere and Er-doped microtoroid - their fabrication process explained and CW lasing properties evaluated.

2.5.1 Er-doped WGM microsphere

Er-doped WGM microsphere can be easily fabricated from commercially available doped Er-doped optical fibers by CO_2 laser reflow. Highly doped erbium fibers (LIEKKI Er30-4/125: $\rho = 4 \times 10^{19} \text{ cm}^{-3}$) are first HF-etched to diameters of around 20 μm (etching rate is 100 nm/min at room temperature), in order to remove excess amount of non-doped cladding which would decrease the concentration of erbium ions. Then, an Er-doped WGM microsphere is realized by CO_2 laser reflow. Figure 2.15(a) shows fabricated microsphere. Diameter is 80 μm and erbium concentration is estimated to be $8 \times 10^{18} \text{ cm}^{-3}$ - as high as possible for low-threshold CW lasing, while minimizing quenching effects.

CW lasing properties were evaluated with the setup in figure 2.15(b). Q factor is 2.4×10^5 and CW lasing is observed. Threshold power is 102 μW and slope efficiency is 2%. Up-conversion (green light emission) due to multi-photon absorption and energy transfer between excited ions can be observed (inset of figure 2.15(d)).

Q factor is limited by its over-coupling with tapered fiber. In fact, WGM microsphere is extremely sensitive to air movements and inevitably adheres to tapered fiber during experiments.

2.5.2 Er-doped WGM microtoroid

In order to achieve better control over microresonator parameters –such as erbium doping concentration, diameter and coupling – Er-doped WGM microtoroids are fabricated in our lab using conventional fabrication method based on CO_2 laser reflow, as explained in section 2.3.2. However, in order to introduce gain material in the WGM microtoroid, a Er-doped silica layer is first prepared by sol-gel method on top of silicon wafer (see figure 2.16). Er-doped sol-gel silica film fabrication is described in details in [60, 61, 62].

Figure 2.17(a) shows SEM image of fabricated microtoroid. Diameter is 40 μm and Q factor is $\sim 1 \times 10^6$ at pump wavelength and 1×10^7 at signal wavelength. Erbium concentration is $2 \times 10^{18} \text{ cm}^{-3}$.

Setup used for CW lasing evaluation is the same as in figure 2.15(b). Figure 2.17(c) show CW lasing spectrum at 1586 nm and figure 2.17(d) reveals ultra-low threshold

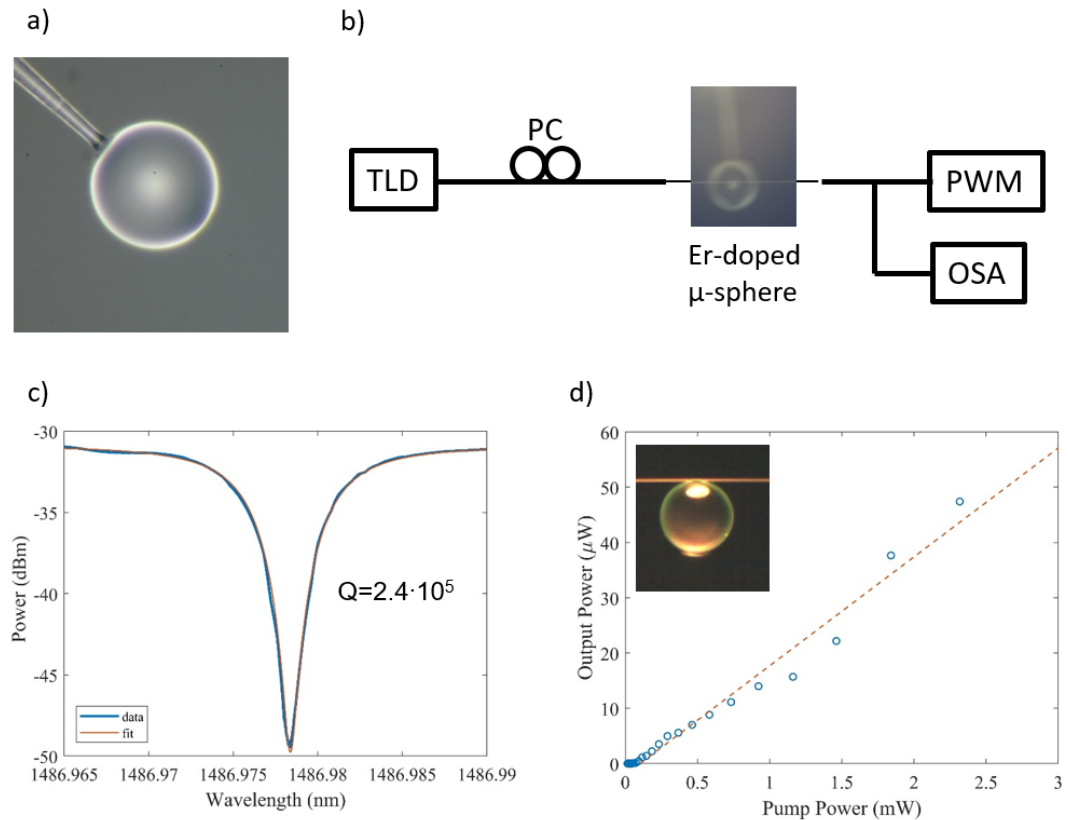


Figure (2.15): (a) Fabricated Er-doped WGM microsphere. Diameter is 80 μm . (b) shows the setup for observing CW lasing and evaluating its properties. (c) Q factor measurement result for fabricated microsphere: Q factor is 2.4×10^5 , mainly limited by over-coupling with the tapered fiber. (d) shows CW lasing evaluation: CW lasing threshold power is 102 μW and slope efficiency is 2%. Inset shows green light up-conversion.

power of $1.2 \mu\text{W}$ and slope efficiency of 0.04%. Up-conversion shows very uniform Er-doping distribution.

From coupled mode equation (section 2.4.2), intracavity power at lasing wavelength can be estimated in the $\sim\mu\text{W}$ order, which is too low to reach saturation power levels of saturable absorbers for modelocking; however, by optimizing coupling, size and Q factor, a high-power Er-doped WGM microtoroid can be fabricated [63].

Therefore, higher Q factor and lower threshold power, together with better control over parameters such as erbium ions concentration, diameter and coupling can be obtained with Er-doped WGM microtoroids [64, 63], making them the most suitable platform for obtaining a WGM modelocked microlaser.

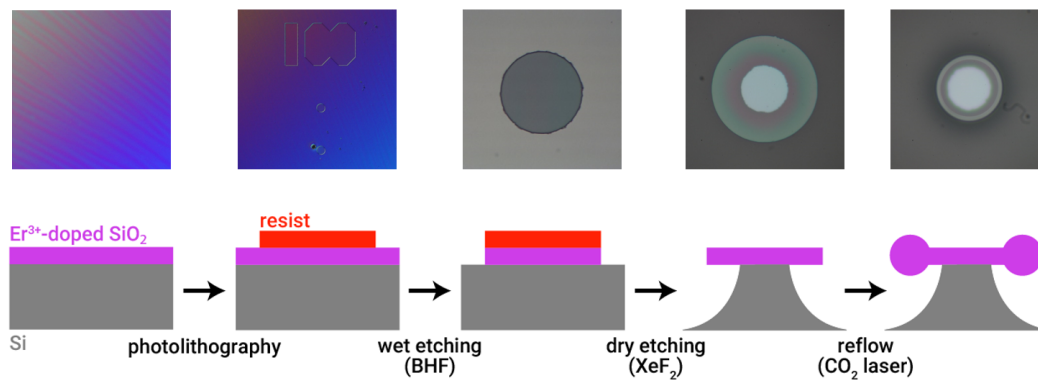


Figure (2.16): (a) Fabrication process of an Er-doped silica WGM microtoroid. Er-doped sol-gel silica film is prepared on silicon wafer and then a WGM microtoroid is fabricated by conventional method. This image was kindly provided by R. Imamura.

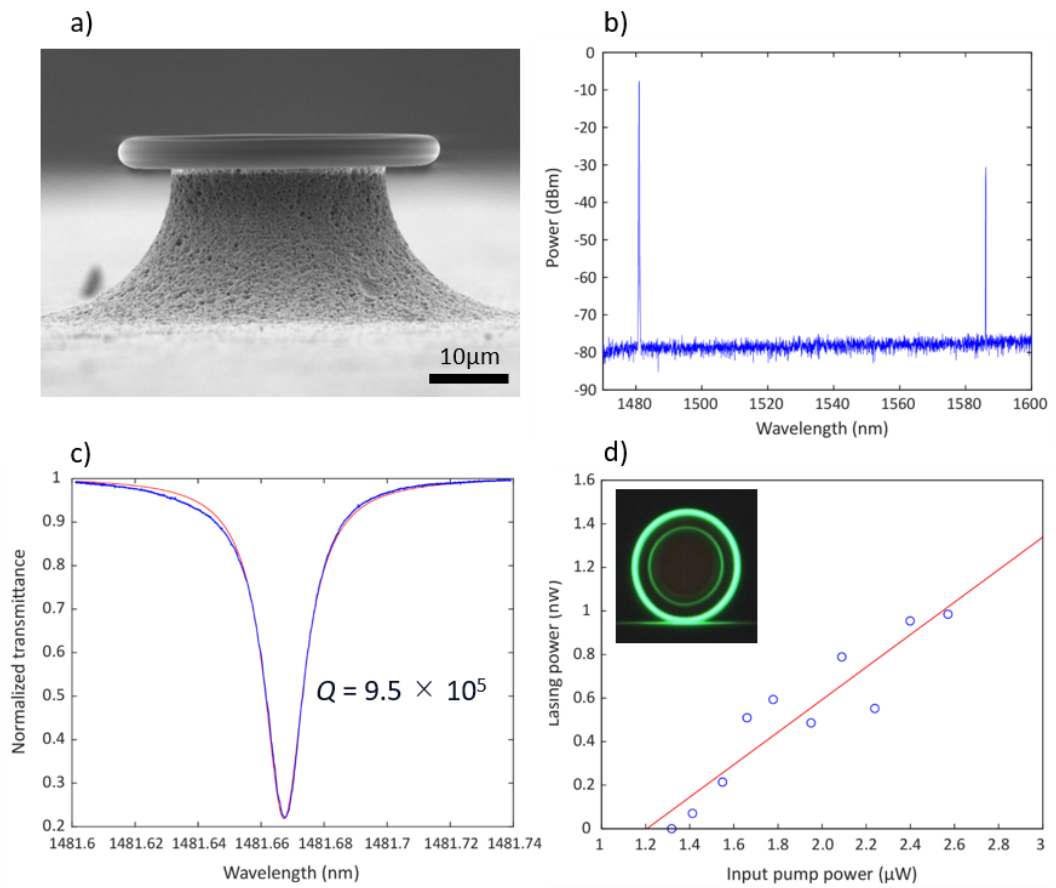


Figure (2.17): (a) SEM image of fabricated Er-doped silica WGM microtoroid. (b) Spectrum from optical spectrum analyzer shows CW lasing at 1586 nm . Peak at around 1480 nm is pump laser. (c) Q factor measurement result: Q factor at pump wavelength is $9.5 \cdot 10^5$. (d) CW lasing is observed with ultra-low threshold power of $1.2\mu\text{W}$ and slope efficiency of 0.04% . Inset shows green light up-conversion. Images were kindly provided by R. Imamura.

2.6 Summary

In this chapter, a comprehensive introduction on WGM microresonators was undertaken, focusing especially on a WGM microtoroid. Its properties, parameters, fabrication methods were thoroughly investigated theoretically and experimentally.

Then, two WGM microlaser platforms – Er-doped microsphere and Er-doped microtoroid - were introduced and their CW lasing properties evaluated. Er-doped WGM microtoroid demonstrated to be the most suitable platform for realizing a modelocked WGM microlaser, due to its high Q factor and fabrication process, which allows broad tunability of its parameters.

Chapter 3

Carbon nanotubes as saturable absorber

Saturable absorber is a key component for pulse formation in lasers. Since the invention of pulsed lasers, many saturable absorbers have been deployed, each with their own advantages and drawbacks.

In the following sections, a brief introduction on the theory and history of saturable absorbers is followed by a comprehensive study on carbon nanotubes as saturable absorber - from the basics of its crystallographic structure to its characterization via Raman Scattering Spectroscopy - because of their excellent properties for passive modelocking.

Next, carbon nanotubes integration methods are investigated. Two methods based on optical deposition are developed: CNT tapered fiber and CNT microprobe.

These methods are evaluated and compared, to determine which one is more suitable for modelocking a WGM microlaser.

3.1 Saturable absorbers in pulsed lasers

Saturable absorbers (SA) are key components for passive modelocking. Through self-amplitude modulation – where absorption decreases as impinging light intensity increases due to carrier depletion at ground state – pulsed operation is encouraged over CW operation. A noise spike is increasingly amplified because of its higher intensity, while its wings – at lower intensity – get absorbed. As a result, roundtrip after roundtrip the energy of the cavity is collected around the high intensity noise peak where loss is reduced, and a sharp pulse is originated.

The basic equation describing the behavior of a saturable absorber is as follows:

$$\alpha(I) = \alpha_{ns} + \frac{\alpha_0}{1 + \frac{I}{I_{sat}}} \quad (3.1)$$

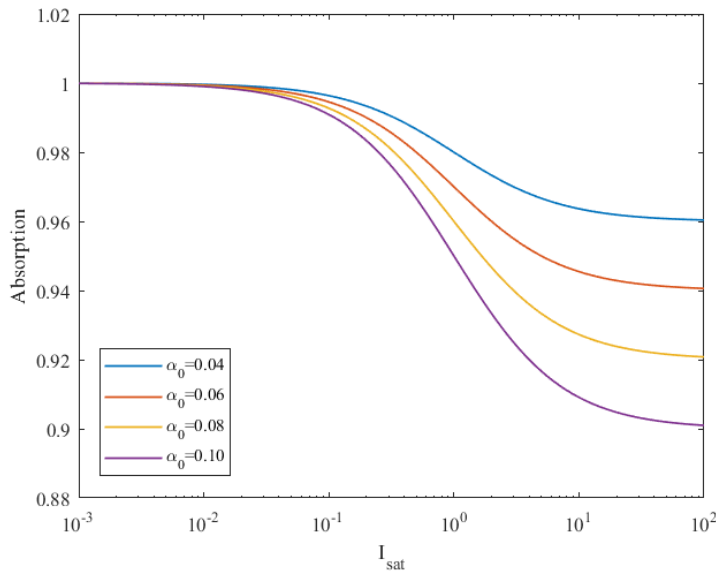


Figure (3.1): Saturable absorption curves for different modulation depths of $\alpha_0 = 0.04$, $\alpha_0 = 0.06$, $\alpha_0 = 0.08$ and $\alpha_0 = 0.10$. SA saturation intensity is fixed at 1 (a.u.) and α_{ns} adjusted so that all curves show unity absorption at low light intensity.

where α_{ns} is the non-saturable loss, α_0 is the modulation depth, I_{sat} is the saturation intensity and α is the total absorption given by the saturable absorber, which is indeed dependent to the light intensity I .

The non-saturable loss α_{ns} describes the component of the absorption that is not possible to saturate even at high light intensities, and it is an unwanted absorption in pulsed lasers because it does not contribute in pulse formation and stabilization.

The modulation depth α_0 describes that part of the absorption that can be saturated with high light intensity and it is responsible for pulse formation and stabilization in pulsed lasers.

The saturation intensity I_{sat} describes the intensity of impinging light at which the saturable absorber is saturating – precisely the modulation depth is half saturated.

Many efforts through the years have been done in order to increase the ratio between modulation depth and the non-saturable absorption of the saturable absorber, and decrease the saturation intensity in order to obtain pulse formation at less prohibitive light intensities.

Other macroscopic parameters of saturable absorbers that have to be considered when designing a pulsed laser are operating wavelength range and recovery time. Operating wavelength range is the range of wavelength where the absorber can actually absorb light and behave as a saturable absorber. Recovery time is the time that it takes for the excited carriers to relax back at ground state. This is also a very important parameter for saturable absorbers, since a large recovery time cannot absorb effectively the tail of the pulse because the carriers are still all excited, therefore resulting in a less sharp pulse. Typical recovery time of saturable absorbers is in the femtoseconds or picoseconds order.

As already mentioned in chapter 1, in theory all light-absorbing materials can potentially be used as saturable absorbers, but in practice only a handful of them satisfy the key saturable absorber requirements for pulsed lasers, such as fast response time, strong nonlinearity, broad bandwidth, low loss and cost, and high power handling.

The table 3.1 reviews the most successful saturable absorbers used today. The most successful saturable absorber is by far the semiconductor saturable absorber mirrors (SESAM). It was developed in the '80 and owing to the remarkable success of semiconductor technologies for electronics, SESAMs achieved excellent performance as saturable absorbers. Nowadays it is used in most pulsed laser configurations, from fiber lasers to semiconductor lasers, and commercially available ultrafast pulsed lasers are modelocked by means of SESAMs.

Relying on the well-developed semiconductor engineering, excellent control over saturable absorber parameters is possible, also allowing to engineer recovery time and operation wavelength range [65]. However, this comes with a high cost and fabrication complexity. In fact, SESAMs fabrication requires highly specialized equipment, post-growth ion implantation or low-temperature growth, all of them needed to control the saturable absorber parameters [66, 4].

Therefore, this major drawback spurred researchers to develop a simpler and more cost-effective saturable absorber. As a result, artificial saturable absorbers based on nonlinear optical effects, such as nonlinear optical loop mirrors (NOLM) or nonlinear polarization evolution were developed [67, 68, 69, 70]. They are very suited for fiber laser configurations, they are simple and cost effective, and because they rely on nonlinear optical phenomena, response time is extremely fast and operation wavelength range is broad. However, they are sensitive to the environment which makes them not reliable solutions for industrial applications and commercialization.

In 2002, single-walled carbon nanotubes (SWCNT) were first discovered as saturable absorber [71, 72]. One year later, S. Y. Set *et al.* [73] demonstrated laser modelocking by using carbon nanotubes. Since then, single-walled carbon nanotubes have been rapidly adopted by several groups for passively modelocking lasers

[47, 74, 75], because of their cost-effectiveness and fabrication simplicity, while their saturable absorption properties are comparable with SESAMs. For example, single-walled carbon nanotubes have been demonstrated to have sub-picoseconds recovery time, which is as fast as SESAM, although the latter requires complex fabrication processes - such as defect engineering - in order to achieve such small recovery time [47, 71].

This and many other advantages – such as broad operating wavelength range and high integrability in many configurations - have paved the way to a new generation of simple and reliable saturable absorbers, with comparable properties to SESAMs but more accessible. Many other 2D and 1D material after single-walled carbon nanotubes have demonstrated saturable absorption properties and have been used in modelocking pulsed lasers - such as graphene and MoS₂ – and many more are waiting to be discovered [76, 77].

Because of the longer history as saturable absorber, single-walled carbon nanotubes are the most studied and demonstrate best saturable absorption properties so far. The following of this thesis will focus on single-walled carbon nanotubes as saturable absorber.

Table (3.1): Review of most commonly used saturable absorbers. Their strengths and weaknesses are highlighted.

| SA characteristics | SESAM | Artificial SA | CNT as SA |
|--------------------|-------|---------------|-----------|
| Fabrication & Cost | × | ○ | ○ |
| Integration | × | △ | ○ |
| Wavelength range | ○ | ○ | ○ |
| Stability | ○ | × | △ |
| SA properties | ○ | △ | △ |

3.2 Single-walled carbon nanotubes

Single-walled carbon nanotubes (SWCNT) were discovered in 1991 by S. Iijima [78] and since then they have attracted unprecedented interest and extensive studies because of their extraordinary thermal, mechanical, electrical and optical properties [79]. Immense progress has been made in their basic understanding, demonstrating the potential of nanotechnology in general. They are one of the most ideal realizations of one-dimensional (1-D) systems available today.

A single-walled carbon nanotube can be viewed as a monolayer of sp²-hybridized carbon atoms arranged in a honeycomb lattice, which is then rolled into a cylinder terminated by two half-fullerene caps (see figure 3.2). The diameter of these species typically ranges from 0.7 to 2.5 nm and their lengths are typically microns and often millimeters, therefore with an aspect ratio that can be as high as 10⁴ or 10⁵.

Its unit cell is defined by the primitive vectors \mathbf{a}_1 and \mathbf{a}_2 and each SWCNT is individuated by a chiral vector C_h , which specifies the two atoms of the graphene

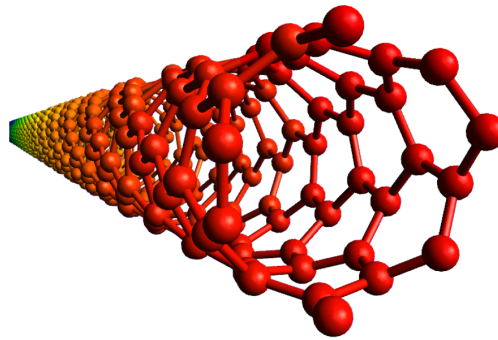


Figure (3.2): Inner structure of SWCNT with chiral vector $C_h(5, 2)$. This image was realized with advanced molecular editor and visualizer Avogadro [80].

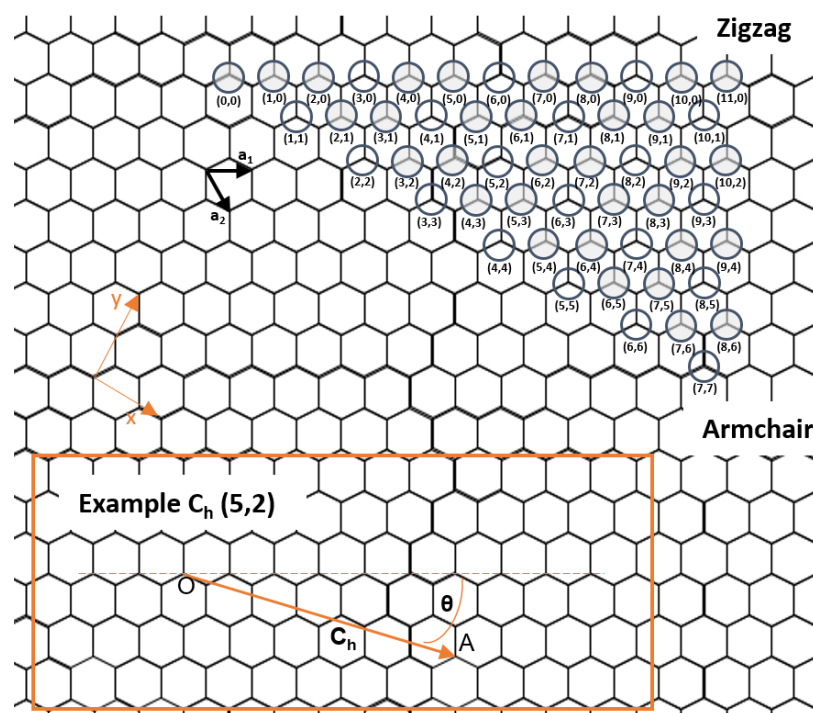


Figure (3.3): Graphene honeycomb lattice: chiral vector $C_h(\overline{OA})$ indicates carbon atoms that are connected to form a nanotube. All possible species of carbon nanotubes according to their chiral vector (n, m) . Filled circles are semiconducting species, while empty circles are metallic species.

sheet which are connected together upon the formation of the tube. (points O and A in example box of figure 3.3). The chiral vector is defined with respect to the graphene primitive vectors as [81]:

$$\mathbf{C}_h \equiv n\mathbf{a}_1 + m\mathbf{a}_2 \equiv (n, m) \quad (3.2)$$

where n and m are integers such that $0 \leq m \leq n$. The form (n, m) is called chiral index. The chiral angle, angle θ formed between \mathbf{C}_h and \mathbf{a}_1 , is of great importance for determining the electronic properties of SWCNT

$$\cos\theta = \frac{\mathbf{C}_h \cdot \mathbf{a}_1}{|\mathbf{C}_h||\mathbf{a}_1|} = \frac{2n + m}{2\sqrt{n^2 + m^2 + nm}} \quad (3.3)$$

While nanotube diameter can be calculated from the chiral vector by

$$d_t = \frac{|\mathbf{C}_h|}{\pi} = \frac{a_{C-C}}{\pi} \sqrt{3(m^2 + mn + n^2)} \quad (3.4)$$

where $a_{C-C} \sim 1.44 \text{ \AA}$, is the nearest distance between neighboring carbon atoms in graphene.

According to how the graphene sheet is rolled up, SWCNTs can be classified into three main types:

- Armchair nanotubes ($\mathbf{C}_h = (n, n)$)
- Zig-zag nanotubes ($\mathbf{C}_h = (n, 0)$)
- Chiral nanotubes ($n \neq m \neq 0$)

As a result of this, single-walled carbon nanotubes can be either metals or semiconductors in behavior, depending on their chirality. This can be deduced from simple considerations of their chiral angle. The figure 3.3(b) discriminates between metallic SWCNT (filled circles) and semiconductor SWCNT (empty circles), according to their chiral vector.

Therefore, there are different types of SWCNT with different properties depending on how the graphene sheet is been rolled, and most importantly the bandgap of SWCNT is dependent upon the diameter of the species [82], which makes it an excellent optical material for next generation opto-electronics (see figure 3.4).

It is important to be able to fabricate selectively metallic and/or semiconductor SWCNT of certain chiral vectors and diameter distributions, according to the intended application. Owing to the intensive studies on their fabrication and synthesis, SWCNT can be prepared by various methods, such as arc-discharge methods, chemical vapor deposition (CVD), laser ablation, vapor-phase growth and so on, each of them with advantages and drawbacks, but most importantly with careful engineering of the diameter in mind [79].

For simplicity, in the following of the thesis we will refer to single-walled carbon nanotubes (SWCNT) as simply carbon nanotubes (CNT), if not specified otherwise.

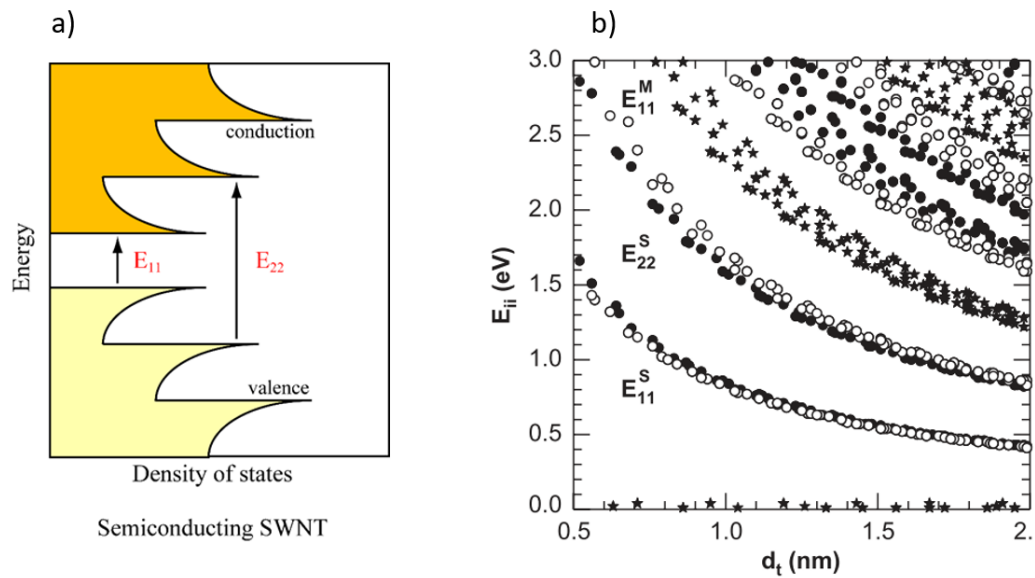


Figure (3.4): (a) SWCNT bandgap transitions. The image was kindly provided by T. Kumagai. (b) Bandgaps of different semiconducting and metallic transitions according to nanometer diameter. Reprinted from *Physics Reports*, 409(2), M. Dresselhaus et al., *Raman spectroscopy of carbon nanotubes*, 47-99, Copyright (2005), with permission from Elsevier [82].

3.3 Raman scattering spectroscopy of carbon nanotubes

As a consequence of what mentioned in the previous section, it is important to be able to characterize carbon nanotubes, in order to assess the qualities and properties of the sample under investigation, especially concerning the quality of the sample and the diameter of carbon nanotubes.

Raman scattering spectroscopy (RSS) is a useful tool to serve this purpose. It measures the intensity of energy of photons that are inelastically scattered off matter. The change in energy between scattered photon and incident photon corresponds to a vibrational or phonon mode of CNT [81].

Raman scattering spectroscopy is the most widely used optical method for characterizing carbon nanotubes, because of its ability to study semiconducting and metallic CNTs non-invasively, regardless of their aggregation state, doping and number of defects.

The figure 3.5 shows typical Raman spectrum of SWCNT in our lab. The lowest frequency modes ($100 \sim 400 \text{ cm}^{-1}$) are called Radial Breathing Modes (RBM) and are typical resonances in carbon nanotube structures, owing to the isotropic stretching vibration occurring in the radial direction perpendicular to the tube axis. Because the frequency of RBMs varies inversely with nanotube diameter, it serves as an indicator of carbon nanotube diameter and it can be simply calculated by the following

equation [81, 82]:

$$d = \frac{248}{\omega_{RBM}} [nm] \quad (3.5)$$

The G band (1550-1600 cm^{-1}) is also a Raman-intense vibration in carbon nanotubes, common to all sp^2 -hybridized carbon, indicating in-plane C-C stretching vibration mode. By studying the splitting of the G band into two sub-resonances G+ and G-, presence of metallic or semiconducting SWCNT can be inferred.

Lastly, the D-band (around 1300 cm^{-1}) is an out-of-plane bending mode that is usually Raman-inactive in pristine sp^2 carbons. But when the translation symmetry of carbon nanotubes is broken by some sort of disorder or defect, the D-band becomes active and its intensity is proportional to the degree of disorder. Thus, the name D-band, which stands for Defect/Disorder. By studying this mode, the presence of defects in the sample can be investigated and therefore the quality of the carbon nanotubes under investigation can be deduced.

A common parameter that evaluates the quality of CNT samples is the G/D ratio (usually above 5) – the greater the ratio the better the quality of CNT.

Therefore, by studying the RBM and G/D ratio through Raman Scattering Spectroscopy, CNT samples can be well characterized optically, in order to see if they are suitable for a certain application prior to their integration.

CNT used in our lab was purchased from Sigma-Aldrich in a powder form. CNT was then dispersed in organic solvents - such as N-methyl-2-Pyrrolidone (NMP), dimethylformamide (DMF) and ethanol – which provide good dispersion and work against the agglomeration tendency of CNTs [83]. To decrease CNT bundling even further, physical dispersion by ultrasonication (Branson Ultrasonics) is necessary (see figure 3.6(a)). Our samples were sonicated for around 30 min, showing good overall dispersion of CNTs (see figure 3.6(b)). Figure 3.5 shows Raman spectrum of our CNT sample, obtained from inVia confocal Raman microscope (RENISHAW). RBM modes range 245-281 cm^{-1} , indicating presence of SWCNTs of diameter 0.9 ~ 1 nm. By comparing the diameters with the graph in figure 3.4, we can derive their bandgap and verify that their operation wavelength range is around 1550 nm, suitable for telecom applications.

Moreover, the strong G band indicates the presence of carbon nanotubes, in prevalence semiconducting SWCNTs but with metallic SWCNTs too, which is important in order to decrease time recovery. In fact, in presence of metallic SWCNTs excited states can relax quickly through the metallic tubes providing sub-picosecond response time [47].

As mentioned earlier, quality can be assessed by evaluating G/D ratio. Our CNT sample has a G/D ratio above 10, which ensures high quality of our sample.

As expected, the investigation of the qualities and properties of this CNT sample, matched well with the specifications given by the producer.

CNT integration methods and experiments explained in the following sections were conducted by using this CNT sample dispersed in organic solvents.

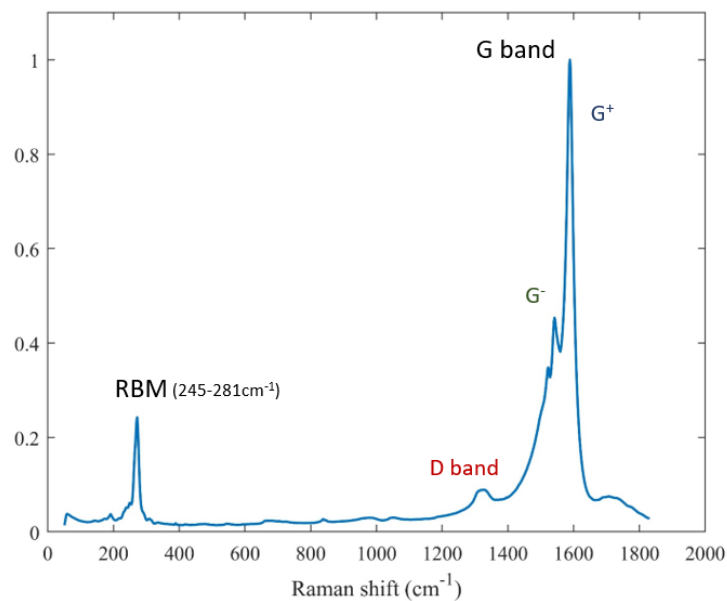


Figure (3.5): Typical Raman scattering spectroscopy of carbon nanotubes. G band, D band and RBM can be observed.

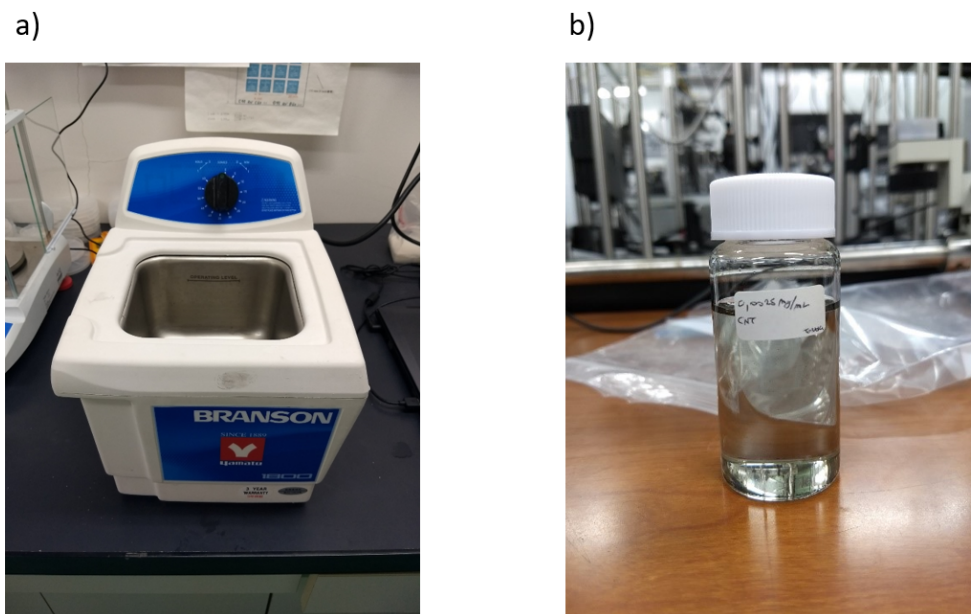


Figure (3.6): (a) Ultrasonicator used to physically disperse CNT bundles. (b) CNT sample in NMP showing good dispersion.

3.4 CNT integration methods

There are different ways to integrate CNTs with WGM microresonators/microlasers. In fact, the saturable absorber can be integrated on the surface of the WGM microresonator, around its coupling element (i.e. tapered fiber) or on a third element that will probe the WGM microresonator. Figure 3.7 shows simple schematics of these three methods.

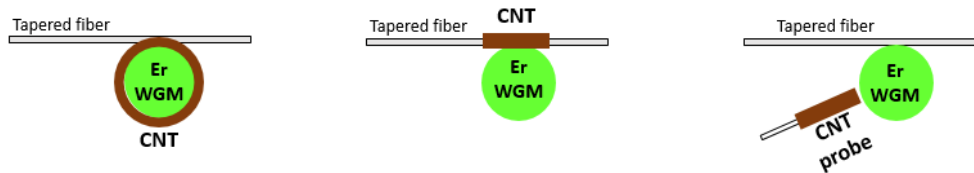


Figure (3.7): Simple schematics of CNT integration methods.

In our lab different methods and techniques have been developed in order to integrate carbon nanotubes on this microlaser system:

- Chemical Vapor Deposition (CVD)
- CNT-embedded polymer coating
- CNT optical deposition around tapered fiber
- CNT microprobe

First two methods integrate CNTs on the surface of a WGM microresonator. However, this causes large Q degradation due to the use of additional lossy substances for integration and surface light scattering [84]. Therefore in order to solve these issues I developed the last two methods based on optical deposition, which allow CNT deposition without adding lossy substances and decreased surface light scattering as CNT integration is performed on other optical elements.

In the following sections, CNT optical deposition around tapered fiber and CNT microprobe methods will be described in details, their advantages and drawbacks explained and the most effective integration method for modelocking a WGM microlaser proposed.

3.4.1 CNT optical deposition around tapered fibers

Fabrication

Optical deposition is a novel deposition method based on optical tweezing effect – recently Nobel-awarded physical phenomena for its vast applications in science and biology - where dielectric particles are attracted by gradient force towards high intensity electric field at the center of the laser beam [85]. If the intensity of the laser beam is properly adjusted to balance out the scattering force induced by light

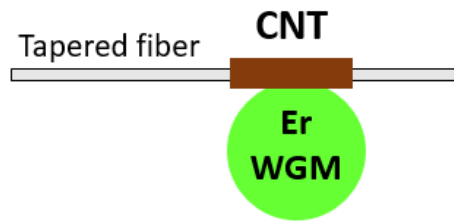


Figure (3.8): Optical deposition around tapered fiber for saturable absorber integration.

with the attractive optical tweezing force, not only particles can be manipulated, but also deposited onto surfaces where the laser beam is focused.

In this way, CNTs can be optically deposited around tapered fibers. By evanescent field interaction, CNT particles are attracted towards high light intensities at the surface, resulting in their deposition onto the surface of the tapered fiber.

The fabrication process and setup is simple [86, 87, 88], with only a few precautions in adjusting the input laser light intensity to encourage optical deposition, as in figure 3.9.

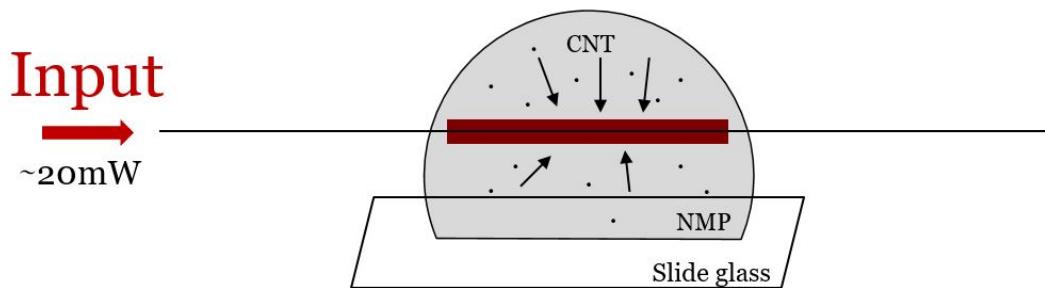


Figure (3.9): Setup for optical deposition around tapered fiber. Optical input power for deposition is ~ 20 mW.

A droplet of CNT dispersed solution is placed onto a substrate (e.g. slide glass, as in figure 3.10(a)), the tapered fiber slowly dipped inside the droplet (figure 3.10(b)) and input laser switched on. If proper input power is launched inside the tapered fiber, deposition occurs rapidly and tapered fiber can be taken out of the droplet (figure 3.10(d)-(e)), taking care that it won't break due to surface tension of the droplet (figure 3.10(c)).

CNT dispersed in NMP was used in this experiment, because of the good solubility of CNT in this organic solvent and higher evaporation temperature compared to other solvents, which allows light illumination for direct observation of the process by digital microscope.

Also, a base for the droplet was conceived as in figure 3.11. This base avoids solution contamination by contaminants on slide glass surface, provides a flexible

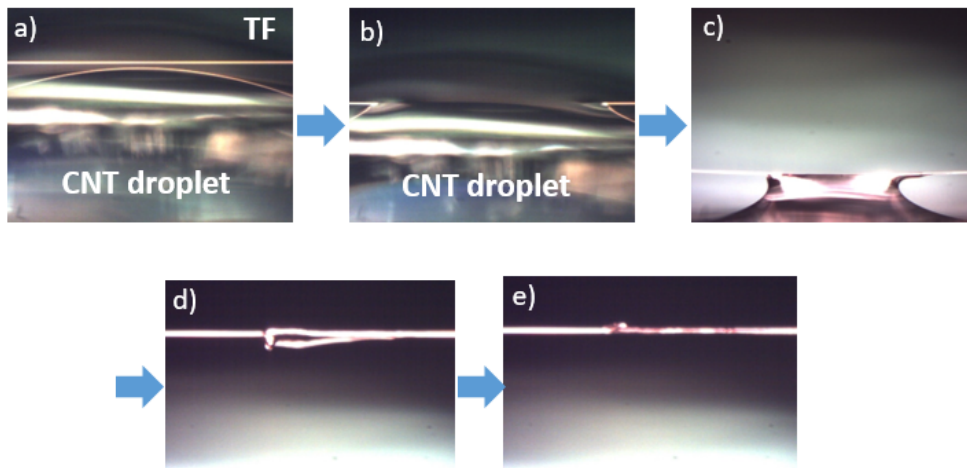


Figure (3.10): Images taken during optical deposition around tapered fiber, that show the different stages of deposition process.

structure against abrupt forces (such as when removing the fiber from the droplet) and most importantly, allows the formation of a smaller and narrower droplet for a more localized deposition.

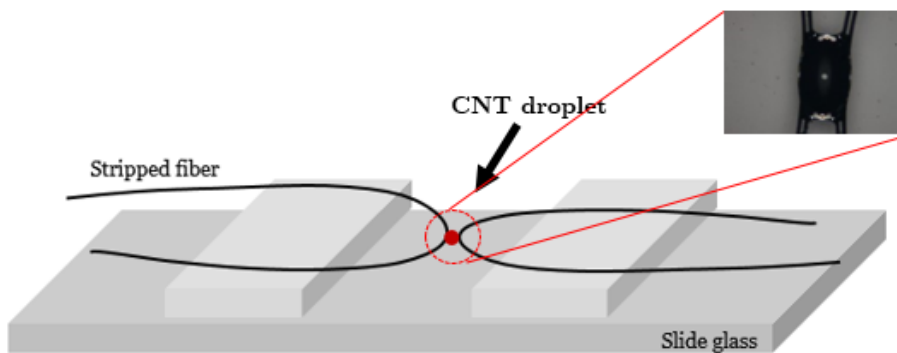


Figure (3.11): Fabricated base for CNT droplet, which improves optical deposition process compared to using a conventional slide glass.

Raman Scattering Spectroscopy verified CNT deposition, with properties as expected from RSS of the original CNT sample, showing that optical deposition does not induce any changes in the optical properties of CNTs (figure 3.12(a)). Mapping of the strength of G band from RSS spectrum at different positions of the tapered fiber, shows uniform CNT deposition (figure 3.12(b)). Because it is important, when coupling the Er-doped WGM microlaser to the tapered fiber, that coupling position

coincides with where CNTs are deposited, a visible red laser can be used to determine deposition location by scattering (figure 3.12(c)).

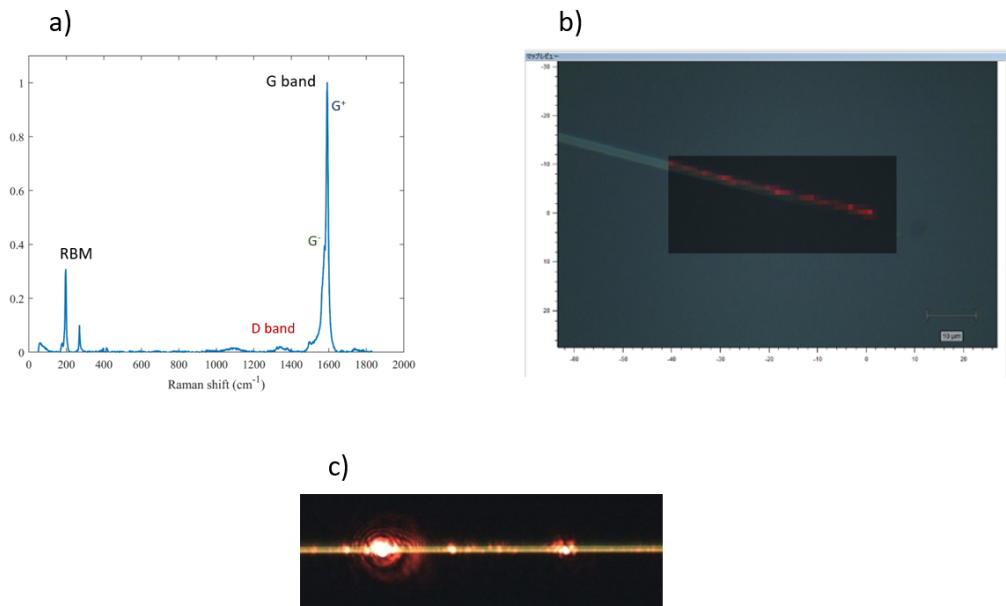


Figure (3.12): (a) Raman scattering spectroscopy of optically deposited CNTs around the tapered fiber. (b) Spatial mapping of the strength of G band along the tapered fiber. Uniform CNT deposition is verified. (c) Deposited CNTs can be individuated with a digital microscope by light scattering with a conventional red laser coupled to the tapered fiber.

SA evaluation of optically deposited CNT around tapered fiber

In order to verify its saturable absorber properties, a transmittance measurement was undertaken for different input light powers. The setup is as shown in the fig. 3.13.

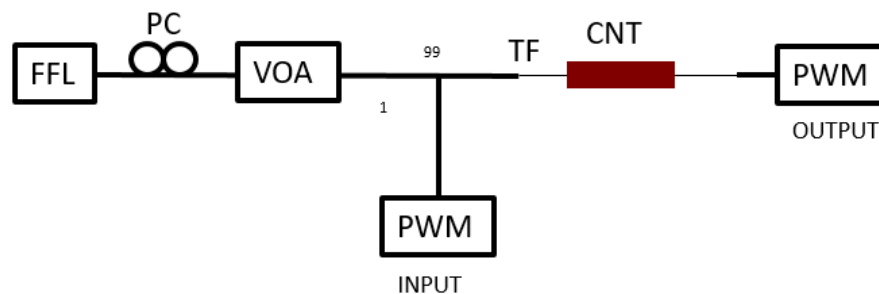


Figure (3.13): Transmittance measurement experimental setup to study SA properties of CNT deposited tapered fiber.

A femtosecond pulsed fiber laser (PriTel Femtosecond Fiber Laser) with 20 MHz repetition rate at 1550 nm is used together with a variable optical attenuator (OZ Optics) for changing the input power. Transmittance is measured for different input powers.

By using the following relationship, input average power can be readily converted to input light intensity:

$$I = \frac{P_{ave}}{A FSR \tau_p} \quad (3.6)$$

where A is the mode area of light in tapered fiber, FSR is the repetition rate of the source pulsed laser and τ_p is its pulsewidth.

The result is shown on graph 3.14. Saturable absorption property is verified, as absorption decreases with increasing light intensity. Loss at low light intensity is around 5dB. Modulation depth is >20% and saturation intensity is in the GW/cm^2 order.

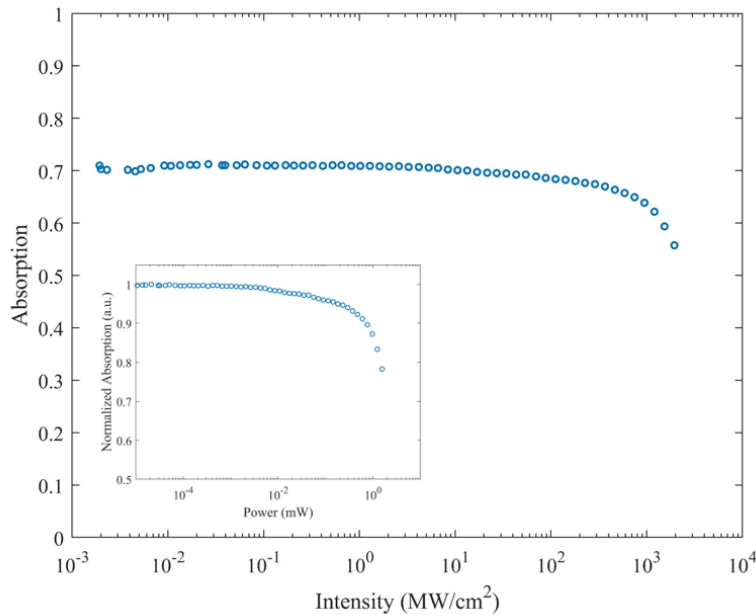


Figure (3.14): Saturable absorption curve is observed for CNT deposited tapered fiber. Inset shows the same result with normalized absorption.

In order to verify that such saturable behavior is attributable to the saturable absorption effect of carbon nanotubes, I performed same transmittance experiment with only NMP deposited on tapered fiber (before it would completely evaporate away) and without anything deposited on tapered fiber.

As it can be seen in figure 3.15, no saturable absorption behavior is observed for these cases; therefore, observed nonlinear loss is given by the power dependent loss of deposited carbon nanotubes.

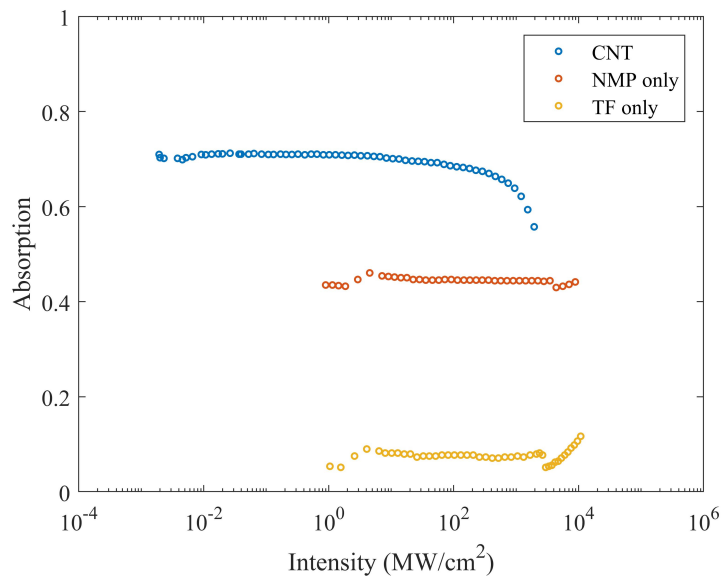


Figure (3.15): Transmission experiment is carried out with tapered fiber and with NMP-tapered fiber; no saturable absorption behavior was observed, as opposed to CNT tapered fiber.

Discussion

Optical deposition of carbon nanotubes on a tapered fiber was performed and its saturable absorption properties verified. However, this integration method comes along with a few issues that convinced me to change approach of CNT integration.

Tapered fibers are only few micrometers in thickness, therefore they are fragile and easily breakable. Working with them during optical deposition process imposes great challenges that can only be overcome with extreme care and it is hard to have full control of the process.

Due to the thin nature of the tapered fiber, it can easily break when removing it from the solution. Surface tension of the solution tends to strongly pull down the fiber until it breaks (see figure 3.16(a)).

Even if tapered fiber was successfully removed from the solution, there is the possibility that impinging light heats up deposited CNTs by light absorption, and produced heat causes the tapered fiber to snap [88]. Therefore, great attention has to be paid in avoiding too high input powers once CNT is deposited, otherwise excess heat will snap the thin and fragile fiber.

Moreover, tapered fibers are notably not durable and dirt can easily trap on their surface. (see figure 3.16(b)) Therefore, even if great care is taken in the deposition of CNTs on tapered fiber, it would not last long and after a few days or weeks - depending on the environment where it is stored - it would be unusable and a new fabrication has to be undertaken.

Lastly, during the optical deposition process another phenomenon works against a localized deposition of CNTs on a small fraction of the length of the fiber. Indeed, when input light is turned on for deposition and its power increased, small droplets form on the side of the main droplet (see figure 3.16(c)). This causes deposition also in unwanted areas, outside the region where tapered fiber is dipped into the CNT droplet. As a result, deposition lengths is in the order of a few hundreds of micrometers.

Due to the difference in temperature inside the droplet caused by impinging light from one side, there is a net mass transfer of the fluid towards colder regions and eventually it accumulates on the side of the main droplet and escapes from it along the tapered fiber, forming small side droplets to minimize surface energy. This phenomenon – called Marangoni effect – which causes mass transfer due to thermal gradient is well known in fields which exploit optical tweezing effect, such as biology and nanotechnology [89, 90, 91]. For compactness, a more detailed description of Marangoni effect is given in the Appendix A.

As a result of Marangoni effect, non-localized deposition is observed with optical deposition of carbon nanotubes around tapered fibers.

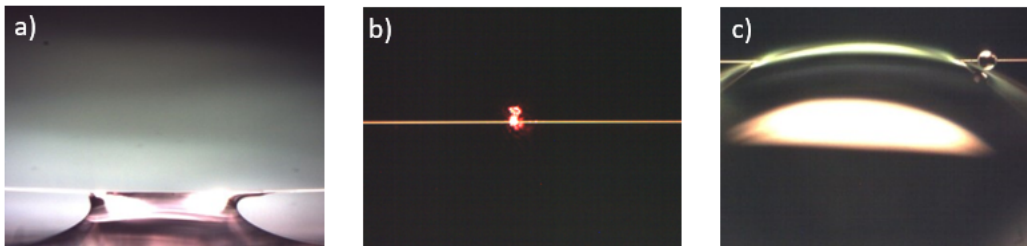


Figure (3.16): (a) Surface tension of the droplet causes the tapered fiber to bend and - depending on its thickness - eventually snap. (b) Tapered fibers tend to trap dirt if not stored in a highly-sealed environment. (c) Marangoni effect causes additional droplets to slide along the tapered fiber during the deposition process, leading to non-localized CNT deposition.

3.4.2 CNT microprobe

Because all previous methods have failed in delivering low loss and are complicated in fabrication, I developed a new method for integrating carbon nanotubes on WGM microresonators in a more flexible and controllable way, always based on optical deposition, which proved to be a convenient and original method for depositing small particles without additional lossy substances.

This method introduces a new element to the device: a CNT microprobe. It is a micrometer size probe with carbon nanotubes optically deposited on its surface.

Although increasing the number of components of the device, the idea behind this method is that it would interact via evanescent field with the WGM microlaser, acting as saturable absorber and allowing great flexibility in its properties by varying the gap between them.

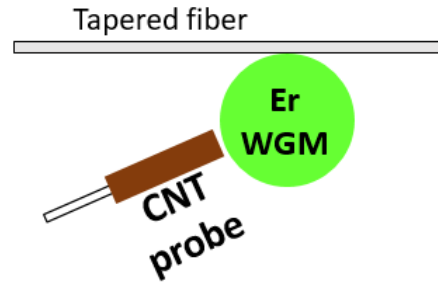


Figure (3.17): Optical deposition on CNT microprobe for saturable absorber integration.

Fabrication

Many groups around the world have worked on the optical deposition of carbon nanotubes on cleaved fiber facets for passive modelocking in fiber lasers - starting from S. Y. Set *et al.* [92, 93] - because of its simplicity, yet potentiality.

By dipping a cleaved fiber end in a solution with well-dispersed CNTs (sonication is necessary beforehand) and feeding laser light inside the fiber, carbon nanotubes are gathered around the naked core of the fiber end by optical tweezing effect and eventually deposit. If input power light and deposition time is properly adjusted, a good control of the process can be achieved.

The setup is as in figure 3.18(a). An EDFA is used to amplify light from the laser diode and its power is carefully monitored with a power meter. Through a circulator, reflection of light from the fiber facet can also be monitored. This allows great control over the deposition process. In fact, because of the different refractive indexes of NMP and CNT - respectively $n_{NMP} = 1.47$ and $n_{CNT} \sim 3$ - when carbon nanotubes start to deposit on the surface of the fiber core, the reflectivity experiences a “jump” (see figure 3.18(b)) and this can be used as an indicator that deposition has started. By measuring the reflectivity R in both cases with silica ($n_{SiO_2} = 1.44$) it is possible to calculate the amount of the “jump”:

$$R_{NMP-SiO_2} = \left| \frac{n_{NMP} - n_{SiO_2}}{n_{NMP} + n_{SiO_2}} \right|^2 \sim -40dB \quad (3.7)$$

$$R_{CNT-SiO_2} = \left| \frac{n_{CNT} - n_{SiO_2}}{n_{CNT} + n_{SiO_2}} \right|^2 \sim -10dB \quad (3.8)$$

Therefore we expect a 30dB jump, which is verified experimentally and thus proving that it can be used to learn when deposition has started and control the amount of deposition by arbitrarily choosing the deposition time.

Figure 3.19 shows microscope image of CNT optically deposited on a cleaved fiber facet by digital microscope. It is evident that CNTs are deposited in a very confined way around the core of the fiber, showing that optical deposition is a precise and controllable deposition method.

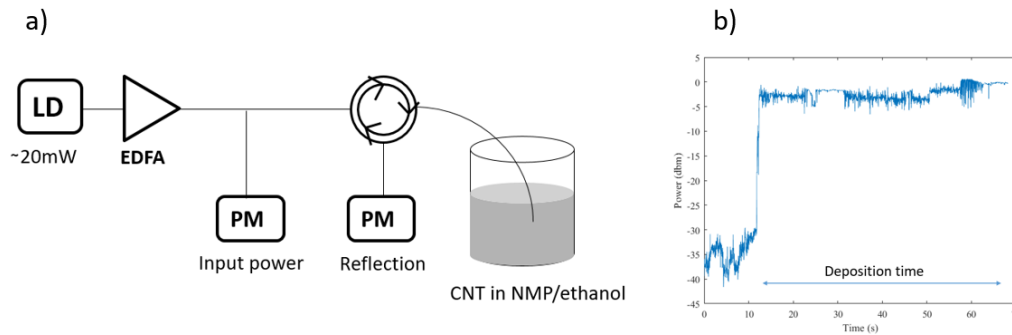


Figure (3.18): (a) Optical deposition setup on a cleaved fiber facet. Input power is carefully adjusted for optimized deposition and reflection is analyzed to monitor deposition process. (b) Reflection monitored by power meter: a 30dB jump reveals when CNT deposition has started. Adjusting deposition time allows control of CNT deposition.

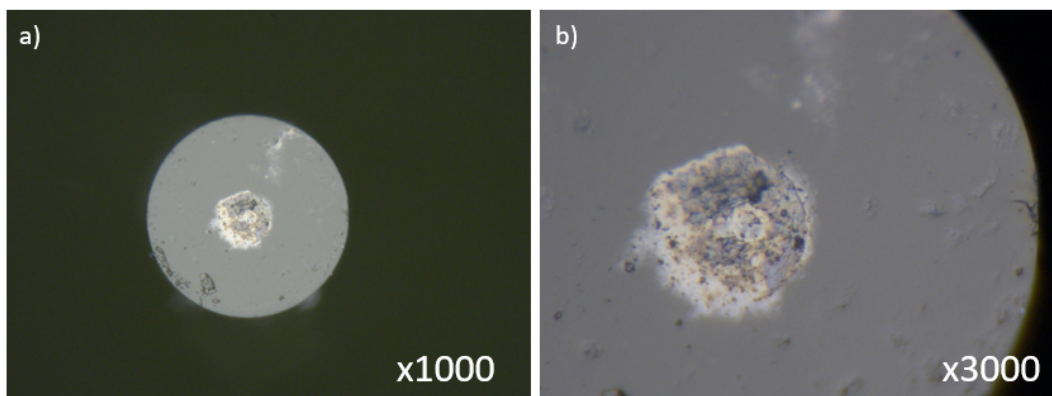


Figure (3.19): (a) Optically deposited CNTs on cleaved fiber facet (x1000 digital microscope). (b) Optically deposited CNTs on cleaved fiber facet (x3000 digital microscope).

However, in our case it is not possible to simply use a bare fiber end of $125\ \mu\text{m}$ in diameter with CNTs deposited on its core as a CNT microprobe, because its size is comparable to that of a WGM microresonator, therefore it would be difficult to position it in a way that carbon nanotubes interact with the evanescent field of the microcavity. Moreover, bare silica would provide an escape path for the evanescent light because of the same refractive with the silica microresonator, causing additional loss and degrading Q factor.

Therefore, it is necessary to decrease the size of the probe, in order to facilitate its positioning and reducing the possibility that evanescent light escapes without interacting with the saturable absorber.

To solve this issue, a microtip was realized by flame-brushing technique. Same process for fabricating a tapered fiber was used, except when the diameter of the fiber is stretched down to a few micrometers, it is cut in half to produce a microtip. Then by optical deposition CNT is deposited on its surface (see figure 3.20). This time reflectometry cannot be used because the end of the fiber is not cleaved, but for the same reason deposition process is simpler and careful adjustment of the power is not necessary.

Because of its micrometer size, it would not act as a nano-scatterer disturbing whispering-gallery modes, but only acting as a loss mechanism [94, 95].

In order to verify and characterize deposited CNTs, Raman scattering spectroscopy was performed on it (see figure 3.21), confirming good quality CNT with G/D ratio above 6 at telecommunication wavelength (RBM $\sim 260\ \text{cm}^{-1}$).

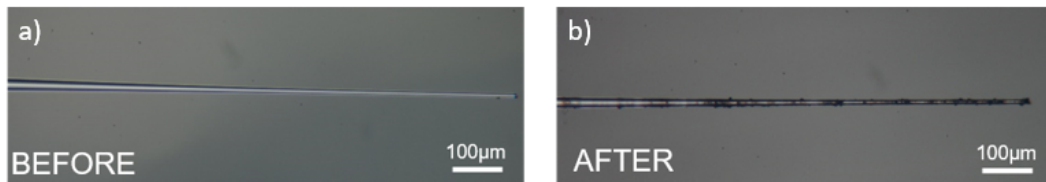


Figure (3.20): Microprobe before and after optical deposition of CNT on its surface. Microtip is realized by flame brushing technique.

SA evaluation of CNT microprobe

In order to evaluate saturable absorption properties of fabricated CNT microprobe a transmission experiment was carried out at different input light powers. To keep SA measurement simple, WGM microresonator was not adopted to evanescently couple light with the CNT probe, but instead a tapered fiber was used. Its evanescent field would couple with the probe, so that the latter can act as a saturable absorber, and transmitted power is monitored.

The setup is as in figure 3.22. PriTel's femtosecond fiber laser is used with a computer-controlled variable optical attenuator (OZ Optics) to change input power automatically.

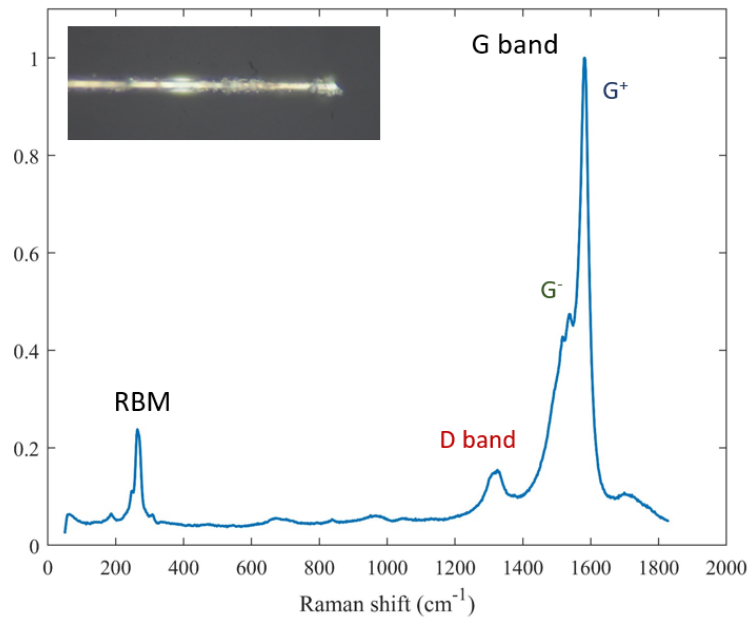


Figure (3.21): Raman scattering spectroscopy of CNT microprobe. G band, D band and RBM can be clearly observed.

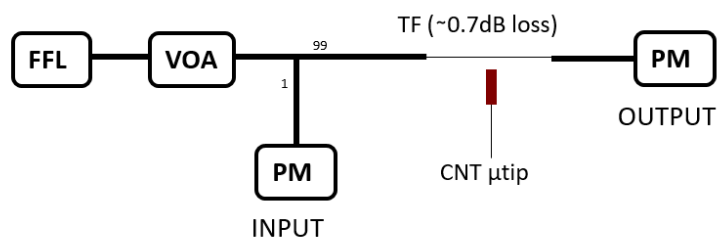


Figure (3.22): Transmission measurement experimental setup for evaluating SA properties of CNT microprobe at 1550 nm.

By taking the difference between the transmittance (for different input powers) with and without CNT microprobe, its loss can be measured

$$\alpha_{CNT} = T|_{w/o \text{ probe}} - T|_{w/ \text{ probe}} \quad (3.9)$$

Because interaction length between CNTs on microprobe and evanescent light of tapered fiber is small, low absorption loss can be expected and measurements of saturable absorption behavior are delicate as it can be hidden beneath the noise fluctuations of the input laser.

As shown in figure 3.23(a) saturable absorption behavior at low absorption loss is verified in the case of CNT microprobe, while a SiO₂ microprobe – without optical deposition of CNTs on its surface – results in a flat curve without revealing any saturation in the absorption. Therefore, it is reasonable to conclude that saturable absorption is given by CNTs on the surface of the probe, interacting with the evanescent field of the light in the tapered fiber.

Also, using the same CNT microprobe different measurements of saturable absorption can be done by varying the gap and the position of the probe with respect to the tapered fiber (see figures 3.23(b)-(d)).

By fitting the equation of saturable absorbers (eq. 3.1), it is possible to evaluate its parameters – non-saturable loss, modulation depth and saturation intensity – and compare with other results and with simulations, to see if they meet modelocking requirements. Fitting results are shown in figure 3.24.

Figures 3.24(c)-(d) show the most important advantage of using CNT microprobe as an integration method. Using the same probe and just varying its position and gap with the tapered fiber, it is possible to change its absorption loss, and consequently changing its saturable absorber parameters. In figure 3.24(d), fitting results of experiments are drawn in the parameter plane of saturation intensity and modulation depth. It is clear that a wide range of parameter's combination is obtainable by simply varying the gap and position of the CNT microprobe.

Due to noise fluctuations of input laser, smaller SA absorption losses cannot be measured, as they fall beneath noise levels. However, it is believed that by changing the position of the microprobe and therefore the extent of interaction between light and CNTs, smaller absorption losses can be obtained, resulting in smaller modulation depths and SA saturation intensities - as explained in detail in appendix C - which are necessary to modelock an Er-doped WGM microtoroid.

This integration method is extremely advantageous in the first stages of modelocking a WGM microlaser, because it allows fine tuning of saturable absorber action without re-fabrication of the device (which was needed in case of previous integration methods): by only varying the amount of CNTs interacting with the evanescent light through change in microprobe's position, saturable absorption can be adjusted – in order to meet modelocking requirements and obtain stable pulse formation.

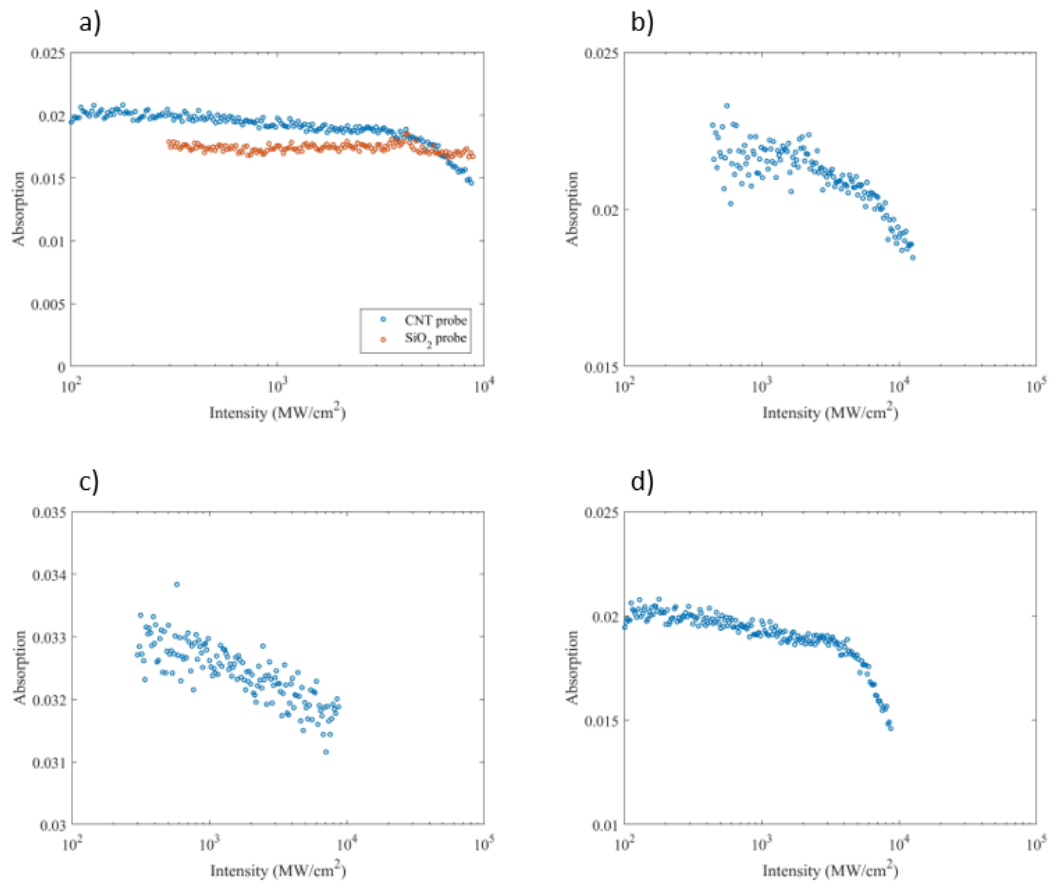


Figure (3.23): (a) SA transmission experiment for CNT probe and SiO₂ probe. Saturable absorption behavior is observed only in the case of CNT probe. (b)-(c)-(d) show saturable absorption of CNT probe at different position with respect to the tapered fiber.

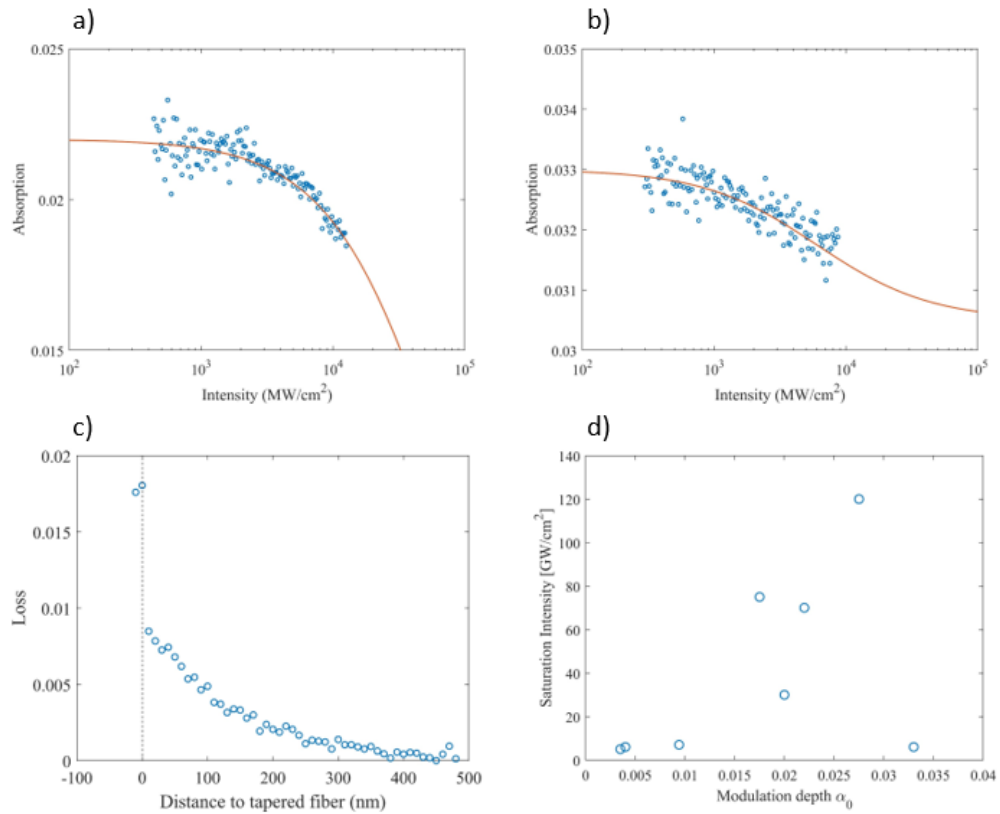


Figure (3.24): (a)-(b) Fitting of experimental results with SA curve. CNT microprobe at different gap and position with respect to tapered fiber yields different SA properties and parameters. (c) Absorption loss of CNT microprobe vs CNT microprobe-tapered fiber gap. (d) Parameters retrieved by fitting experimental results are plotted on the parameter's plane of SA saturation intensity and modulation depth.

3.5 Summary

Saturable absorbers are key components in pulsed lasers for passive modelocking. In this chapter, I reviewed basic theory and history of saturable absorbers, highlighting the strengths and advantages of carbon nanotubes as saturable absorbers compared to traditional ones.

Advantages include:

- Easily accessible and cost effective
- Simple fabrication
- Broad wavelength operation range
- Fast recovery time

Methods of carbon nanotubes integration to whispering-gallery mode microresonators undertaken in our lab are introduced and new techniques based on optical deposition are developed to overcome the challenges imposed by previous methods: CNT optical deposition around tapered fibers and CNT microprobe.

Both of them are relatively simple to fabricate and saturable absorption properties were verified, but the first raised new problematics:

- Low success rate of deposition because of the thin nature of the fiber
- Non-durability of tapered fibers in time
- Non-localized deposition of carbon nanotubes due to Marangoni effect

On the other hand, CNT microprobe – simpler in fabrication and more reliable in its properties – has demonstrated to be the best method of integration, allowing low absorption loss and adjustable saturable absorption properties by changing the gap between probe and microresonator, in order to meet modelocking requirements.

Chapter 4

Modelocked fiber ring laser

In previous chapters, erbium doping technique and carbon nanotubes integration method have been developed. However, pulse formation is the result of many complicated phenomena taking place inside a resonant cavity. Self-phase modulation (SPM) and dispersion, gain and nonlinear loss act simultaneously on the intracavity electric field: only in certain conditions pulse formation and stable modelocking is obtained. Therefore, a careful design stage of a modelocked WGM microlaser is needed.

In order to create a reliable simulation model of such an original and innovative device, first a trustable model of a modelocked fiber ring laser is to be realized and verified with experiments. Once its reliability is confirmed, the model can be miniaturized into a WGM microlaser incorporating a saturable absorber.

In the following sections, theoretical framework based on the Modified Nonlinear Schrödinger Equation (MNLSE) is clarified and a fiber laser modelocked by CNT as SA is realized and pulsed operation verified. Its parameters are derived and simulation is run; then, simulation results and experimental results are compared and reliability of the model is verified.

4.1 Theoretical framework

4.1.1 Modified nonlinear Schrödinger equation

The Nonlinear Schrödinger Equation (NLSE) is a well-known equation used to describe propagation of light in nonlinear optical fibers [96]:

$$\frac{\partial}{\partial T}A(t, T) = \left(-iD \frac{\partial^2}{\partial t^2} + i\delta|A|^2 \right) A(t, T) \quad (4.1)$$

where $A(t, T)$ is the slowly varying field envelope – normalized so that $|A(t, T)|^2$ is its power – D is the dispersion and δ is the self-phase modulation coefficient. T is the long-term time variable - used to describe the step size, while t is the short-term time variable - used to describe intracavity waveform.

D can be calculated from the dispersion parameter D_p , which is usually given in the datasheets of optical fibers:

$$D = \frac{c}{n} \beta_2 \quad (4.2)$$

$$\beta_2 = -\frac{D_p}{2\pi c} \lambda_0^2 \quad (4.3)$$

where β_2 is the group velocity dispersion. Dispersion accounts for the different speed at which different wavelengths travel inside a medium, because of the wavelength-dependent nature of refractive index.

On the other hand, self-phase modulation takes into account the power-dependent nature of refractive index:

$$n(I) = n_0 + n_2 I \quad (4.4)$$

where n_2 is the nonlinear refractive index. Therefore, SPM causes a nonlinear phase delay with the same temporal shape as the light intensity. This phenomena is considered in the Nonlinear Schrödinger Equation by the SPM coefficient, which can be calculated from the nonlinear refractive index n_2 :

$$\delta = \frac{2\pi n_2 c}{\lambda_0 A_{eff} n} \quad (4.5)$$

where A_{eff} is the effective mode area.

Equation 4.1 supports soliton solution. Thanks to the balance between dispersion and SPM nonlinearity, solitons are non-dispersive light pulses and therefore their shape is not distorted during propagation. In fact, SPM up-chirp - the instantaneous frequency increase in time caused by nonlinear phase delay - can be compensated by anomalous dispersion - where longer wavelength travel slower than shorter wavelength, resulting in a down-chirp.

Because of this feature, in the '70 they were proposed as a new way for carrying information in optical communication systems and since then many researchers proved the potentiality of soliton error-free optical communication [97, 8, 9, 98]. This gave enormous attention to solitons and the Nonlinear Schrödinger Equation as its master equation.

Modelocked fiber lasers are excellent pulsed lasers for soliton formation and they can also be modelled by Nonlinear Schrödinger Equation, because they are indeed realized with optical fibers. Figure 4.1 shows typical scheme of a modelocked fiber ring laser, where cavity is circular and not linear. The following discussion will consider fiber ring lasers, but same framework can be applied to linear cavities too.

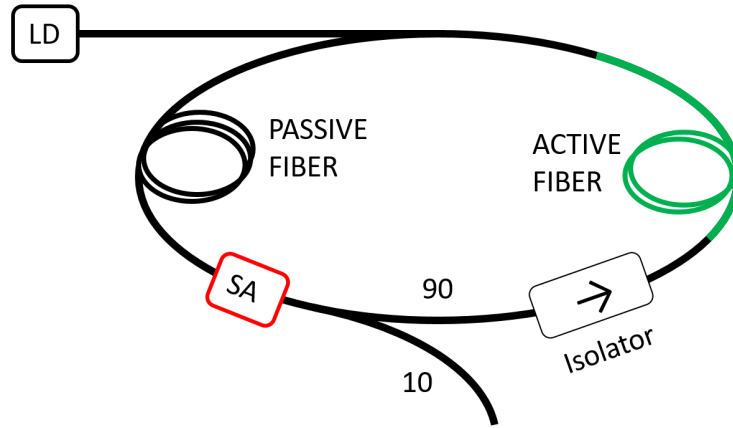


Figure (4.1): Schematics of typical modelocked fiber ring laser.

However, in order to generate solitons, modelocked fiber lasers are also made of an active fiber – which amplifies light in the cavity – and a saturable absorber – which shapes the waveform to promote and stabilize pulse generation. Follows the need to modify the Nonlinear Schrödinger Equation, in order to take into account the effects of the active fiber and the saturable absorber. This equation – called Modified Nonlinear Schrödinger Equation – was developed by A. Haus [99, 100, 101] and sometimes it is also referred as Haus’ master equation:

$$\frac{\partial}{\partial T} A(t, T) = \left(-iD \frac{\partial^2}{\partial t^2} + i\delta |A|^2 \right) A(t, T) + \left(g - (l + \alpha(t, T)) \right) A(t, T) \quad (4.6)$$

where g is the gain of the active fiber, $\alpha(t, T)$ is the nonlinear loss of the saturable absorber and l takes into account other linear losses of the cavity.

During propagation, gain g experiences saturation and it possesses a gain bandwidth – window of frequencies where light is amplified by the active fiber. Therefore, it can be rewritten as:

$$g = g_0 \left(\frac{1}{1 + \frac{|A(t, T)|^2}{P_{sat}^g}} \right) \left(1 + \frac{1}{\omega_g^2} \frac{\partial^2}{\partial t^2} \right) \quad (4.7)$$

Where g_0 is the gain coefficient, $|A(t, T)|^2$ is the intracavity power and P_{sat}^g is the gain saturation power, and ω_g is the gain bandwidth. The second factor takes into account gain saturation, while the last factor is less intuitive in the time domain, but considering its Fourier Transform

$$\left(1 + \frac{1}{\omega_g^2} \frac{\partial^2}{\partial t^2}\right) \Leftrightarrow \left(1 - \frac{\omega^2}{\omega_g^2}\right) \quad (4.8)$$

it is clear that it considers the gain bandwidth with a parabolic filtering function in frequency, where ω are angular frequencies with respect to the central frequency.

The effect of the saturable absorber $\alpha(t, T)$ - considered ideal in the following of this work (i.e. fast recovery time) - is directly derived from 3.1:

$$\alpha(I) = \alpha_{ns} + \frac{\alpha_0}{1 + \frac{|A(t, T)|^2}{P_{sat}^a}} \quad (4.9)$$

where α_{ns} is the nonsaturable absorption, α_0 is the modulation depth and P_{sat}^a is the saturation power of the saturable absorber.

Since a modelocked fiber laser is composed of different elements - such as active and passive fiber, coupler and saturable absorber - the model is applied accordingly to different sections of the fiber ring as in the table below:

| | |
|--------------------|--|
| Active fiber | $\frac{\partial}{\partial T} A(t, T) = \left(-iD \frac{\partial^2}{\partial t^2} + i\delta A ^2\right) A(t, T) + gA(t, T)$ |
| Passive fiber | $\frac{\partial}{\partial T} A(t, T) = \left(-iD \frac{\partial^2}{\partial t^2} + i\delta A ^2 - l\right) A(t, T)$ |
| Saturable absorber | $A_{out}(t, T) = T_{SA} A_{in}(t, T) = \sqrt{\left[1 - \left(\alpha_{ns} + \frac{\alpha_0}{1 + \frac{ A(t, T) ^2}{P_{sat}^a}}\right)\right]} A_{in}(t, T)$ |
| Output coupler | $A_{out}(t, T) = T_{coupler} A_{in}(t, T)$ |

Because of the complicated nature of the equations, there is no analytic solution and thus simulation is necessary. In order to solve it, Split Step Fourier Method (SSFM) is used. This method is widely used to study pulse propagation in nonlinear media by NLSE, because of its increased computational speed at same accuracy. By splitting the equation into its nonlinear and linear part, and solving them separately in time and frequency domain respectively within a step, higher performance can be obtained thanks to the use of FFT algorithm. Because of the “splitting”, accuracy of the solution is affected but careful choice of step size can maintain required accuracy [96].

Finally, by seeding the model with an initial noise and monitoring its evolution in time, modelocking behavior can be investigated [102, 103].

4.1.2 Step size determination

Split Step Fourier Method is a powerful method for solving above model, but careful choice of the step size is necessary to achieve accurate solution. Therefore, a simple and fast step size determination method proposed by Rasmussen *et al.* [104] is used.

Error per roundtrip for different step sizes h can be calculated as follows:

$$\epsilon(h) = \sqrt{\frac{\int |A_{out,num}(h, t) - A_{out,exact}(t)|^2 dt}{\int |A_{out,exact}(t)|^2 dt}} \quad (4.10)$$

where $A_{out,num}(h, t)$ is the output field calculated by SSFM after one roundtrip for a given step h . $A_{out,exact}(t)$ can be on the other hand calculated by using a step size h much smaller than the given step.

By plotting the error per roundtrip for different step sizes, required step size can be determined. Figure 4.2 shows the result for active and passive fibers used in experiments at 4.2.

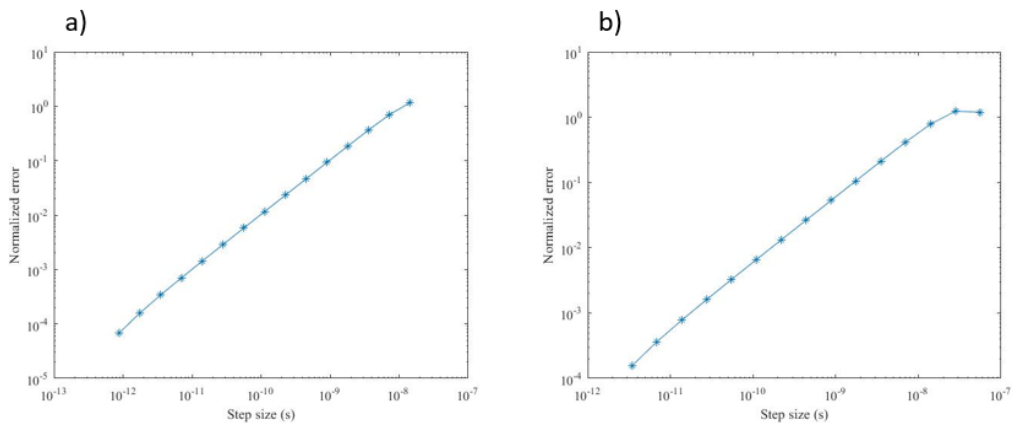


Figure (4.2): (a) Calculation of normalized error per roundtrip of active fiber output field with Split Step Fourier Method for different step sizes. (b) Calculation of normalized error per roundtrip of passive fiber output field with Split Step Fourier Method for different step sizes.

Therefore, a step size of 10^{-10} s will yield a normalized error of less than 1%.

4.2 Modelocked fiber ring laser - Experiment

In order to verify that the model in section 4.1.1 is correct and accurate, it has to agree with experimental results. In our lab, modelocked fiber ring lasers were not available nor there was any know-how on their fabrication, therefore a modelocked fiber laser is realized from scratch in less than a week by using carbon nanotubes as saturable absorber. This proves the potentiality of carbon nanotubes, as simple and cost-effective saturable absorbers (see 3.1). In the following sections, fabrication of modelocked fiber ring laser is described in details. Active fiber is chosen and characterized, and CNT is integrated in the fiber ring and its SA properties evaluated. Also, parameters for simulation are retrieved from experiments.

4.2.1 Er-doped fiber

3 meters of erbium doped fiber (LIEKKI Er30-4/125) is used as active fiber. Its properties and parameters are evaluated with the setup in figure 4.3(a).

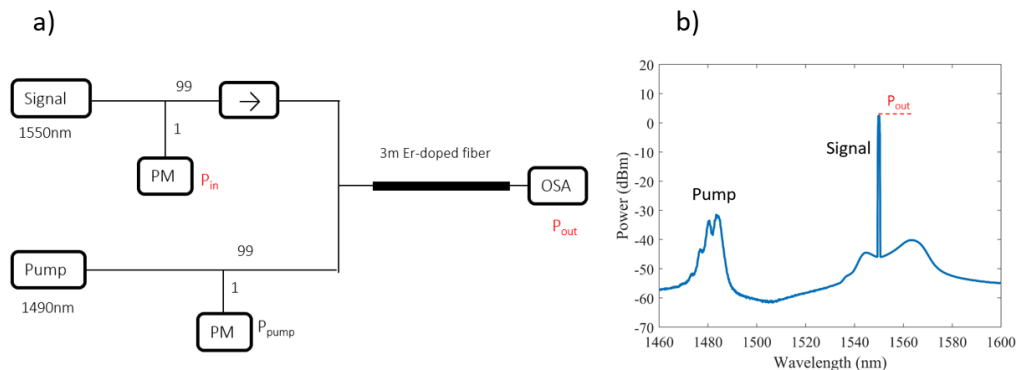


Figure (4.3): (a) Setup for the characterization of a 3m Er-doped fiber. (b) Typical optical spectrum analyzer result: pump is observed at around 1480 nm and amplified signal at 1550 nm. Because of the narrow linewidth of the laser, P_{out} can be measured by detecting the peak at 1550 nm. Amplified spontaneous emission can be observed at the base of the signal.

A single mode fiber-coupled laser diode at 1490 nm (QFLD-1490-150S by QPHOTONICS) is used as pump laser and its power monitored. Although by specification its maximum output power can reach 150 mW, due to damages to its pins, maximum output power was 27 mW. Another laser diode (Santec TSL-710) at 1550 nm is used as signal and its power monitored. An isolator (ISO) is used to ensure that monitored power is only given by signal laser.

Both pump and signal are coupled in a 3 meter Er-doped fiber and the output is sent to an Optical Spectrum Analyzer (OSA: AQ6375B by YOKOGAWA). Figure 4.3 shows typical OSA spectrum of the experiment. Signal output power can be measured and gain calculated, for different values of signal and pump power. As a result, the fiber under test – 3 meters of er-doped fiber – is completely characterized and simulation parameters derived (see figure 4.4).

Figure 4.4(a) shows gain against signal power for pump powers of 10 mW, 16 mW, 22 mW and 27mW. Gain saturation for high signal powers can be observed. Figure 4.4(b) investigates gain dependence from signal wavelength: a gain bandwidth ω_g of 19 nm is obtained. Figure 4.4(c) shows small signal gain for different pump powers, as retrieved from (a). Pump saturation power can be observed. Finally, figure 4.4(d) shows signal saturation power dependence to pump power, as retrieved from (a).

Therefore, by analyzing these results, simulation parameters can be obtained for this active medium in a modelocked fiber ring laser.

These experimental results are in reasonable agreement with simulation results of Er-doped fibers. For compactness, comparison between simulation and experiment is addressed in Appendix B.

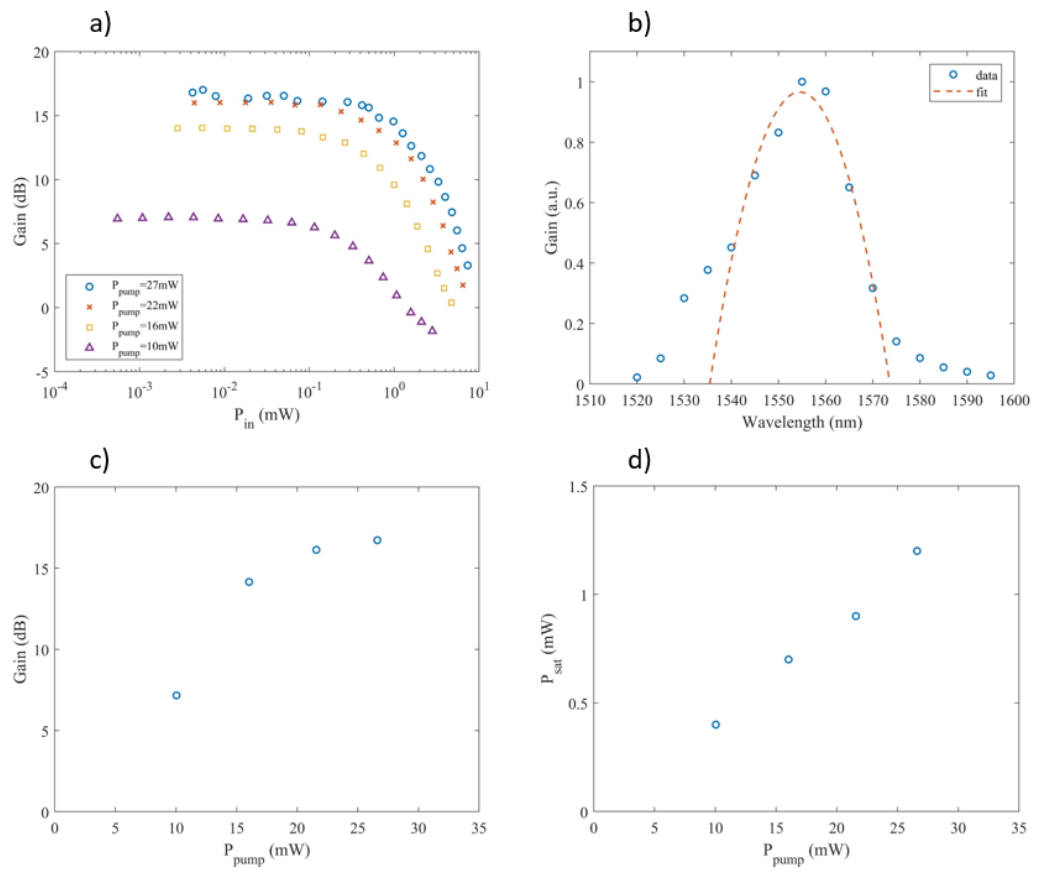


Figure (4.4): (a) 3m Er-doped fiber gain against signal power for different pump powers. Gain saturation can be observed. (b) Gain dependence to the wavelength is investigated and parabolic fitting is performed. Gain bandwidth is 19 nm. (c) Gain for different pump powers. (d) Gain saturation power for different pump powers.

4.2.2 Carbon nanotubes on fiber ferrule

Fabrication and integration of carbon nanotubes in the fiber ring follows the work of Nicholson *et al.* [105]. Carbon nanotubes are optically deposited on a fiber ferrule in the same way as described in section 3.4.2. CNTs are dispersed in ethanol with a concentration of 0.04 mg/ml and ultrasound sonication is performed to decrease CNT agglomeration.

Ethanol has good CNT dispersion properties and it quickly dries at room temperature and therefore measurements are faster.

Saturable absorption properties are verified with a transmission experiment at different input light powers (see 3.4.1 for experimental setup). CNT loss is around 3 dB, of which modulation depth is 8% and non-saturable loss is 40% (saturable to non-saturable loss ratio of 1:5). SA saturation intensity is 460 MW/cm² (see figure 4.5).

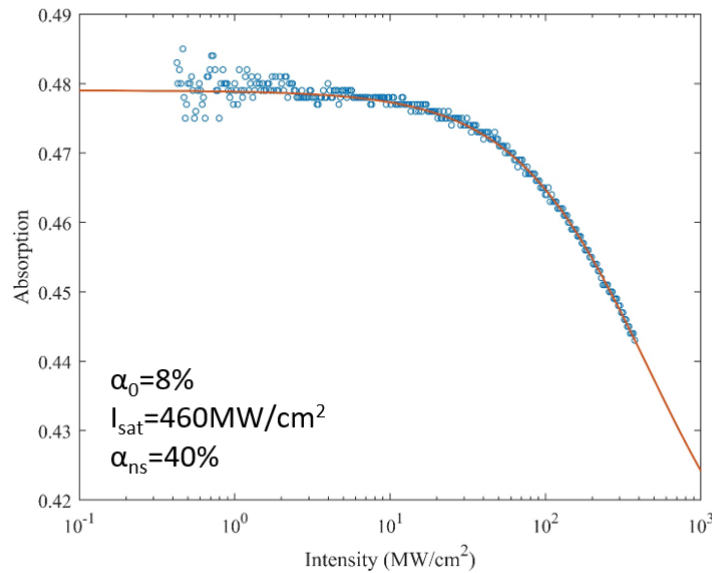


Figure (4.5): SA evaluation of CNT optically deposited on fiber ferrule. Modulation depth is 8%, non-saturable loss is 40% and SA saturation intensity is 460 MW/cm².

Relationship between saturable absorber parameters is also investigated. For compactness, such analysis is included in appendix C.

4.2.3 Realization of ML fiber ring laser

Incorporating in the fiber ring above elements – 3m Er-doped fiber and the saturable absorber – a modelocked fiber ring laser is realized as in figure 4.1. A 10:90 output coupler is used and its output monitored. Pump laser diode is the same as the one used for characterizing the active fiber.

A passive fiber (Corning SM-28) of around 12 meters is used to tune the dispersion of the cavity towards the anomalous dispersion to support soliton formation.

In absence of the saturable absorber, the fiber ring laser shows CW operation. When saturable absorber is introduced in the cavity and pump power is adjusted, pulsed operation is achieved. Figure 4.6 shows OSA (AQ6375B by YOKOGAWA) results for these two cases.

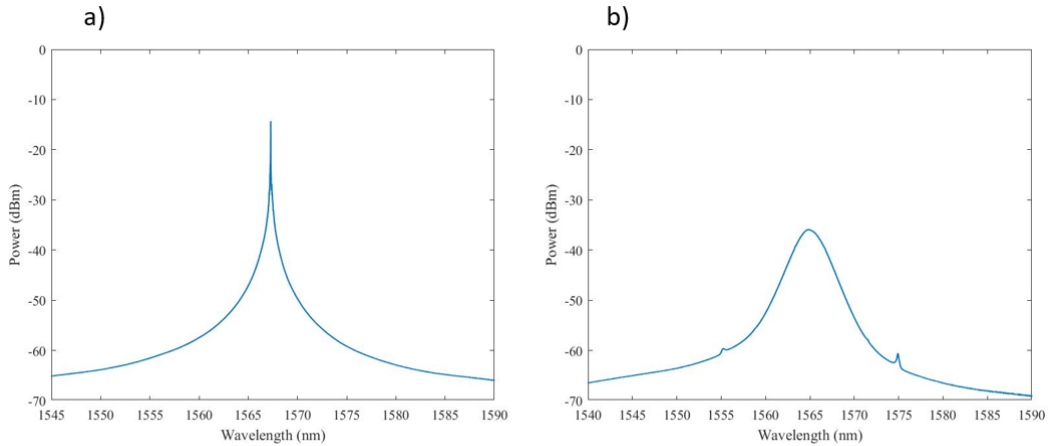


Figure (4.6): (a) OSA spectrum of CW Er-doped fiber ring laser. (b) OSA spectrum of Er-doped fiber ring laser modelocked by CNT as saturable absorber.

Modelocking operation is further verified by sending the output of the fiber ring into a SHG autocorrelator (AC: PulseCheck APE150), an RF spectrum analyzer (R3273 by ADVANTEST), a power meter (Agilent 81634B) and a digital oscilloscope (RTE1104 ROHDE&SCHWARZ). Results are shown in figure 4.7. Oscilloscope in figure 4.7(a) shows stable modelocking operation. SHG autocorrelator trace in figure 4.7(b) confirms pulse operation and soliton formation by matching well with soliton fitting (sech^2). Pulses width is 960 fs.

Figure 4.7(c)-(d) are RF spectrum analyzer's results and confirm stable modelocking with around 14.2 MHz repetition rate - which agrees well with the cavity length of ~15 meters - and high extinction ratio >50 dB.

CW and ML operation were compared also in terms of output and pump power (see figure 4.8). CW operation has threshold power of 10.7 mW and slope efficiency of 3.1%. By inserting a saturable absorber, inevitably threshold power increases to 11.8 mW and slope efficiency decreases to 1.7%.

It is worthwhile to note that before entering modelocking regime at around 15 mW, the fiber ring laser incorporating a saturable absorber works in CW operation. In fact, pulsed operation is possible only if intracavity power reaches SA saturation power and thus pump power has to be increased. On the other side, if pump power is increased too much (>20 mW), intracavity power becomes too high and modelocking stability is ruined. As a result, light pulse splits into multiple pulses under the action

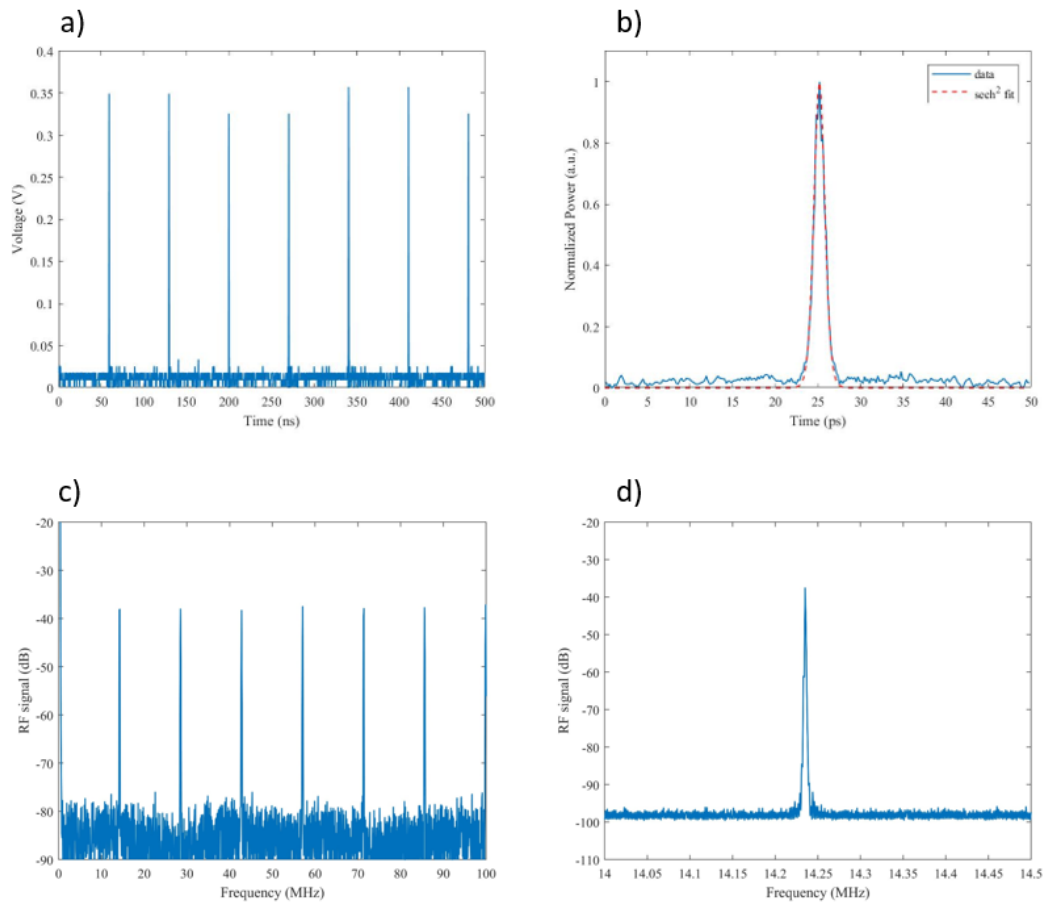


Figure (4.7): (a) Oscilloscope trace of output of ML fiber ring laser. Stable modelocking can be observed. (b) SHG autocorrelation trace confirms soliton generation with a pulsewidth of 960 fs. Red dashed line is the sech^2 fit. (c)-(d) RF spectrum analyzer's traces at RBW=100 kHz and RBW=1 kHz respectively, showing stable modelocking at 14.2 MHz repetition rate and high extinction ratio of >50dB.

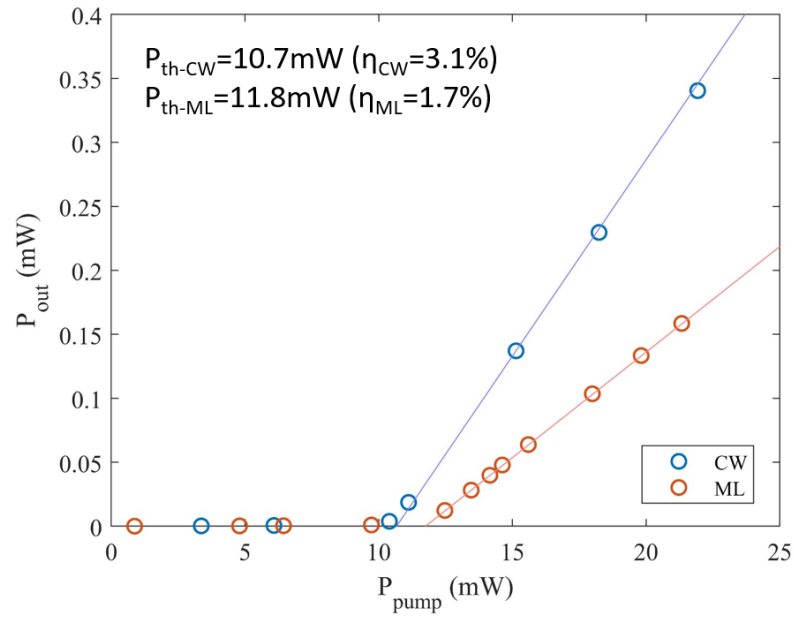


Figure (4.8): CW and ML operation output power against pump power comparison. Inserting an SA inevitably increases threshold power (from 10.7 mW to 11.8 mW) and decreases slope efficiency (from 3.1% to 1.7%).

of self-phase modulation. Figure 4.9 shows OSA and AC of multiple pulses regime at 20 mW.

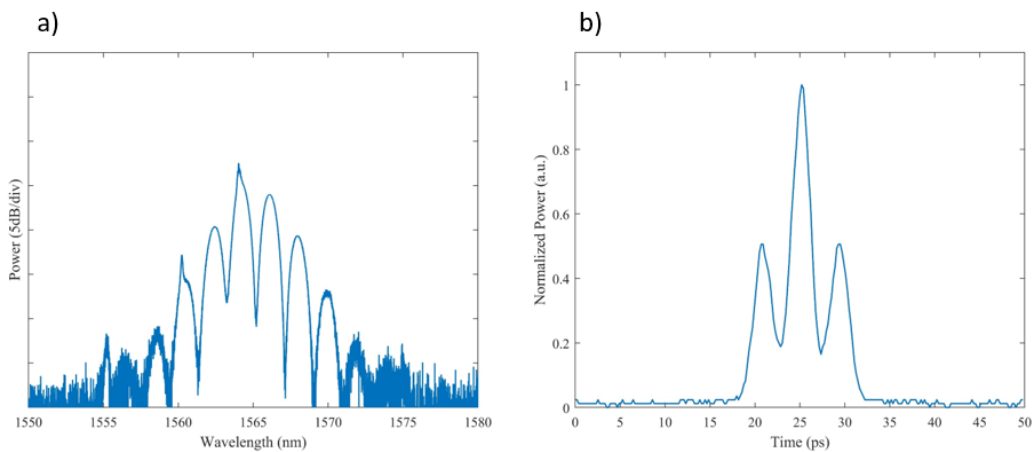


Figure (4.9): (a) OSA spectrum of ML fiber ring laser at 20 mW. The spectrum modulated into equidistant humps reveals the presence of two pulses travelling inside the cavity at 5 ps delay. (b) AC trace confirms OSA hypothesis with a trace that corresponds to two pulses 5 ps apart.

In summary, I realized a fiber ring laser modelocked by carbon nanotubes as saturable absorber from scratch in less than a week. This proves the simplicity in fabrication of the fiber ring, especially concerning the saturable absorber integration,

which in case of other SAs (such as SESAMs) needs complicated fabrication and expensive equipment, while integration in fiber configuration is not straightforward.

Moreover, gain and nonlinear loss parameters needed for simulation are retrieved. In the following section, experiment and simulation are compared, in order to verify the reliability of the model from 4.1.1.

4.3 Simulation vs Experiment

Table 4.1 summarizes parameters used in the simulation. Gain and saturable absorber parameters are retrieved experimentally, while self-phase modulation and dispersion parameters are obtained from fiber specifications.

Table (4.1): Parameters used in simulation.

| ACTIVE FIBER | PASSIVE FIBER | SA |
|--|--|--|
| $D_p = -20 \text{ ps}/(\text{nm km})$ | $D_p = 12 \text{ ps}/(\text{nm km})$ | $\alpha_{ns} = 0.4$ |
| $n_2 = 31 \cdot 10^{-21} \text{ m}^2/\text{W}$ | $n_2 = 31 \cdot 10^{-21} \text{ m}^2/\text{W}$ | $\alpha_0 = 0.08$ |
| $g_0 = 12.8 \text{ dB}$ | $l = 0.2 \text{ dB}$ | $I_{sat} = 460 \text{ MW}/\text{cm}^2$ |
| $P_{sat}^g = 0.68 \text{ mW}$ | $A_{eff} = 85 \text{ }\mu\text{m}^2$ | |
| $\omega_g = 19 \text{ nm}$ | $L = 11.7 \text{ m}$ | |
| $A_{eff} = 85 \text{ }\mu\text{m}^2$ | | |
| $L = 3 \text{ m}$ | | |

Simulation results are shown in figure 4.10 when compared to experiments. They agree well and Kelly sidebands are also predicted by the model. The main difference between experiment and simulation is believed to be due to the absence in the latter of amplified spontaneous emission (ASE), which was not considered in the model.

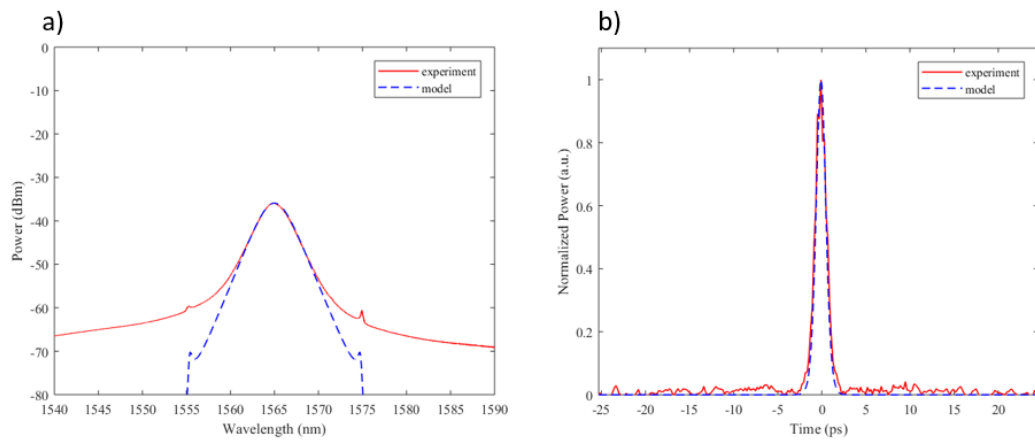


Figure (4.10): (a) Blue dashed line is the model, which agrees well in frequency domain with experimental OSA results in red. Position of Kelly sidebands is also predicted by the model. Discrepancies between simulation and experiments are mainly due to amplified spontaneous emission, not accounted for in the model. (b) Blue dashed line is the model, which also agrees well in time domain with experimental AC results in red.

4.4 Summary

In this chapter, a reliable model of a Er-doped fiber ring laser modelocked by carbon nanotubes as saturable absorber was realized based on the Modified Nonlinear Schrödinger Equation (MNLSE), widely used master equation to study nonlinear optics in fiber lasers.

In order to verify the model, a modelocked fiber ring laser was realized and its simulation parameters retrieved. It was proven that carbon nanotubes provide a very simple and cost-effective way to obtain passive modelocking. In fact, threshold power was 12 mW with sub-picosecond pulsewidth.

Finally, simulation was run with retrieved parameters and results agreed well with experiments. This shows that created model is reliable in predicting modelocking behavior and therefore it can be confidently miniaturized into a WGM microlaser with saturable absorber, in order to investigate its modelocking regime.

Chapter 5

WGM modelocked microlaser

In the previous chapter, a reliable model has been created for a fiber ring laser mode-locked by carbon nanotubes as saturable absorber. Therefore, it can be miniaturized into a WGM microlaser, in order to investigate its modelocking regime. To do so, the model has to be adjusted to the case, its significant parameters automatically swept and behavior autonomously detected. This imposes additional challenges to the investigation.

In the following sections, above challenges are addressed and clarified, and WGM microlaser behavior explained and operation regimes classified. Next, modelocking regime is investigated and relationship between device's parameters studied in detail. Finally, a design strategy for WGM modelocked microlaser is proposed.

5.1 Theoretical framework - revisited

The model used for the simulations in this chapter are based on the Modified Non-linear Schrödinger Equation (MNLSE), which is explained in details in 4.1.1:

$$\frac{\partial}{\partial T}A(t, T) = \left(-iD\frac{\partial^2}{\partial t^2} + i\delta|A|^2\right)A(t, T) + \left(g - (l + \alpha(t, T))\right)A(t, T) \quad (5.1)$$

where gain term can be expanded as:

$$g = g_0 \left(\frac{1}{1 + \frac{|A(t, T)|^2}{P_{sat}^g}} \right) \left(1 + \frac{1}{\omega_g^2} \frac{\partial^2}{\partial t^2} \right) \quad (5.2)$$

and saturable absorber loss term:

$$\alpha(I) = \alpha_{ns} + \frac{\alpha_0}{1 + \frac{|A(t, T)|^2}{P_{sat}^a}} \quad (5.3)$$

Conceptually, a WGM microlaser is a miniaturization of a fiber ring laser and hence, same model is used but in a different region of parameters' space, because of the smaller size. In fact, same phenomena take place - first term of the 5.1 refers to the dispersion, the second term to self-phase modulation, the third to the gain and the last term takes into account the linear/nonlinear losses (i.e. saturable absorber) of the cavity – but with a much smaller effect per roundtrip on the intracavity field.

Because of the large number of parameters, in the following of this thesis the non-saturable loss α_{ns} is not considered - although it would degrade Q factor in practice - in order to simplify the investigation.

Because of the much smaller cavity length, in the case of a WGM microresonator it is not necessary to determine a step size smaller than the cavity length to achieve a high degree of accuracy when solving with Split Step Fourier Method; instead, step size can be equal to the roundtrip time and roundtrip after roundtrip intracavity waveform can be monitored.

This simplifies the model and lightens the computational load.

5.2 Modelocking investigation

5.2.1 Contribution graph

Because of the large number of parameters in the model, it is extremely complicated to understand how all of them are related and affected by each other, hence making it difficult to run meaningful simulations and interpret the results.

In order to better understand the behavior of the intracavity field with a certain set of parameters, I developed a contribution graph, which visualizes the contribution to intracavity field of each phenomenon against intracavity power.

Figure 5.1(a) shows one example of contribution graph. Gain and loss (black lines) contribute to the amplified of the field, while dispersion and SPM (red lines) contribute to the phase of the field. Apart from the dispersion, all the other three phenomena have a power dependence, which is illustrated in the graph. Gain shows saturation when it approaches its saturation power, and analogously loss (intrinsic loss + saturable absorber) saturates at saturable absorber's saturation power. On the other hand, the contribution of self-phase modulation on the phase increases linearly with the power.

Although it is an approximate tool, because of its simplicity, it allows effortless understanding of how a given parameter set will affect the behavior of the device.

As an example, let's study and predict the behavior of intracavity field for the set of parameters depicted in figure 5.1(a). Since at low-power initial noise gain is higher than the loss, intracavity power will build up until gain starts to saturate and meets loss line. This is approximately where intracavity power will settle in steady state. If around this power, the saturable absorber starts saturating – hence decreasing overall loss – and dispersion and SPM are in good balance, pulse formation is encouraged inside the cavity. While SPM and dispersion balance is crucial for soliton generation, SA helps pulse formation and stabilization. As a result, a stable modelocking is obtained as predicted (see figure 5.1(b)).

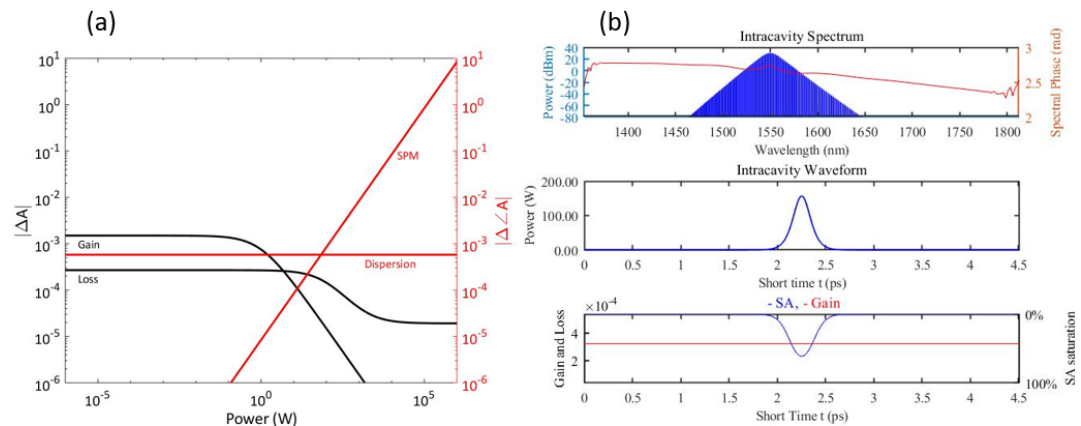


Figure (5.1): (a) Contribution graph for $D=300 \mu\text{m}$, $Q = 10^8$, $\beta_2 = -10 \text{ ps}^2/\text{km}$, $\alpha_0 = 0.0005$ and $g_{Tr} = 0.003$. $P_{sat}^g = 1 \text{ W}$ and $P_{sat}^a = 100 \text{ W}$. Gain and loss contributions to the amplitude of the field (black lines), SPM and dispersion contributions to the phase of the field (red lines) are plotted against intracavity power. This tool helps understanding device's behavior for a given set of parameters and has predictive capabilities. (b) Numerical result for the set of parameters used in (a). As predicted by its contribution graph, pulse formation and stable modelocking is obtained.

Therefore, given a certain set of parameters, the contribution graph is extremely helpful in understanding the relationship between them and the consequent behavior of the WGM microlaser incorporating saturable absorbers. Most importantly, it allows effortless and objective interpretation of the results – such as why pulse formation has or has not been obtained - and how to correct device's parameters in

order to improve its performance. Finally, it possesses predictive capabilities too, as shown in the example explained above.

5.2.2 Modelocking detection

Because of the large number of parameters and possible outcomes of the simulation, it is necessary to find a way to easily detect modelocking regime and identify other regimes as well. One way to do this is to compute automatically the ratio between peak power and average power of intracavity waveform for a given set of parameters. Then visualize the result on the parameters'.

Figure 5.2 shows an example of such graph, where small signal gain of the gain material and modulation depth of the saturable absorber are swept as parameters. For now, I would like to focus on the modelocking detection strategy, without concentrating on the meaning of these parameters and of this graph in terms of device's design, which will be thoroughly discussed in section 5.3.

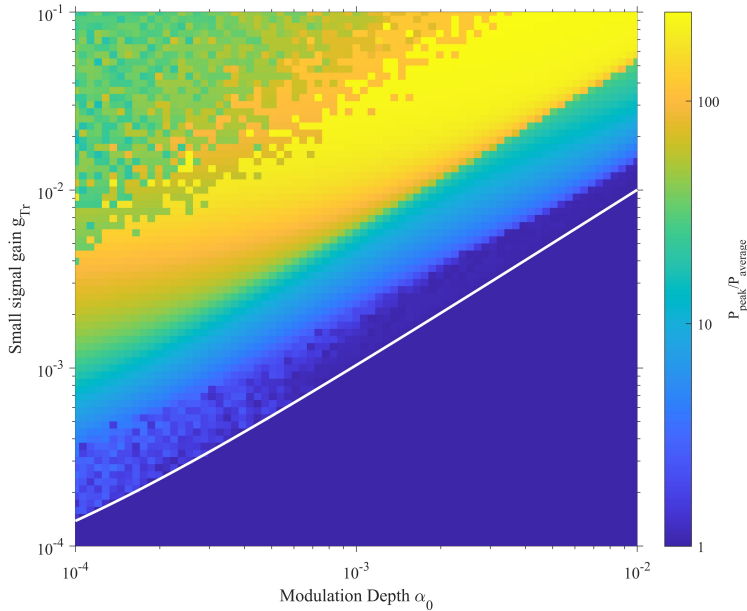


Figure (5.2): Modelocking investigation with small signal gain and modulation depth as parameters. Each square in the parameter's plane contains the numerical result of the model for a given set of parameters. Here, peak power to average power ratio is used as criterion to interpret simulation results.

P_{peak}/P_{ave} gives a good indication of different working regimes, because if pulse formation happens, intracavity power tends to concentrate in a small fraction of the roundtrip time, hence peak power is large. As a result, the ratio P_{peak}/P_{ave} will be large as well (yellow areas in figure 5.2).

On the other side, if pulse formation does not occur, intracavity power is well distributed along the cavity and consequently its peak power is also weak. This results in small P_{peak}/P_{ave} (blue areas in figure 5.2).

Because of the action of SPM, multiple pulses can also happen to travel inside the cavity: in this case, peak power is large because of pulse formation, but not larger than in the case of only one pulse, because intracavity power has to be shared between these pulses. Thus, the resulting P_{peak}/P_{ave} will lay somewhere between the case with one pulse formation and the case with no pulse formation (green areas in figure 5.2). Therefore, by studying the graph in figure 5.2, it is possible to deduce the behavior of the device for a given set of parameters and what areas of the parameters' plane would be modelocked.

The white line indicates where gain is equal to the loss, therefore since below that line intracavity power is not amplified, simulation is not run for that set of parameters.

Above that line we can see that P_{peak}/P_{ave} ratio is low (dark blue area) – close to unity – and pulse formation is not happening. Moving towards the higher parts of the graph, pulse formation is more and more evident because of the increasing ratio (from light blue to yellow areas). However, the ratio does not monotonically increase, and on the top left corner of the graph (green areas) we see that P_{peak}/P_{ave} ratio settles to a value that is lower compared to the yellow areas below. This can be interpreted with the case where multiple pulses travel inside the cavity.

P_{peak}/P_{ave} ratio is good indicator of device's behavior, however it is difficult to classify confidently modelocking regimes by only considering this criterion. Therefore, other significant indicators are necessary. I developed other two indicators: one is the pulsewidth and the other one is the stability.

Pulsewidth means that intracavity waveform is analyzed and peaks that are higher than three times the average intracavity power are detected automatically. To visualize the result, when one peak is detected, its pulsewidth is measured and plotted on graph – large pulsewidths are colored in yellow while narrower pulsewidths are colored in red; if multiple peaks are detected, gray color is assigned to that set of parameters; if no peaks are detected no color is assigned (white).

Figure 5.3 shows an example with the same parameters' plane as in the previous P_{peak}/P_{ave} case. The black line indicates that gain is equal to the loss. Single pulse formation happens in the same area as predicted in the P_{peak}/P_{ave} graph.

P_{peak}/P_{ave} also predicts well multiple pulses, as it can be confirmed by the gray zone of figure 5.3.

However, in the previous two indicators there is no information on the stability of the calculated solution. Therefore, it is necessary to consider stability too, in order to understand if modelocking is stable or not. Stability is studied by calculating the coefficient of variation of the intracavity power for the last 3% of total roundtrips:

$$\text{Stability} = \text{Coeff. of variation}^{-1} = \frac{\mu(P_{cav})}{\sigma(P_{cav})} \quad (5.4)$$

where μ is the mean and σ is the standard deviation. Intuitively low stability means that there is a large fluctuation in time on the intracavity power, while high stability means that this fluctuation is low.

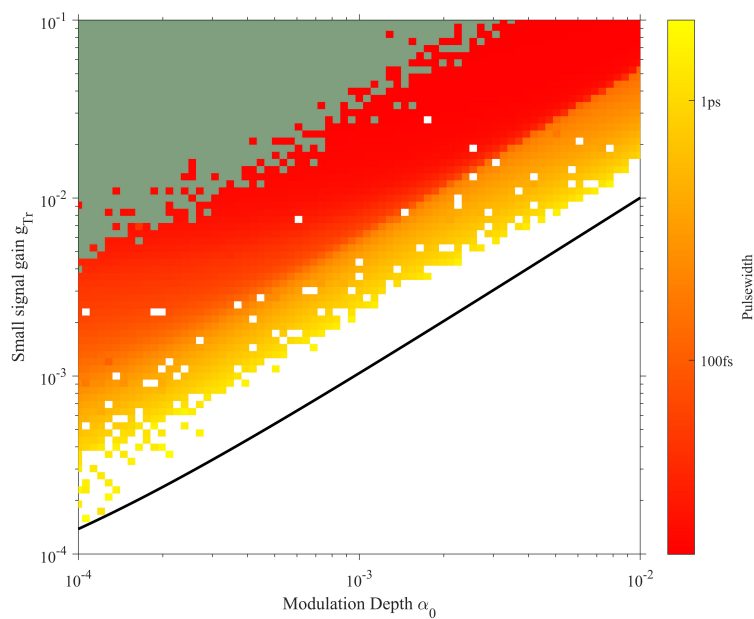


Figure (5.3): Modelocking investigation using pulsewidth as criterion. Large pulsewidths are colored in yellow while narrower pulsewidths are colored in red; if multiple peaks are detected, gray color is assigned to that set of parameters; if no peaks are detected white color is assigned. White dots in the yellow-red area are cases where modelocking occurs but pulse is formed at the beginning or end of the intracavity power array in the simulation and due to how the peak detection algorithm is realized that peak is not detected.

By plotting this indicator in the parameters' space, the stability of the solution can be compared to the previous indicators concerning pulse formation. Figure 5.4 shows the stability result for the same parameters' plane as previous graphs. Red areas indicate low stability, meaning that intracavity power is fluctuating a lot, while moving to the green areas and finally the blue areas, the stability is larger and larger. By visual inspection, above a stability of 10^5 the system can be considered stable.

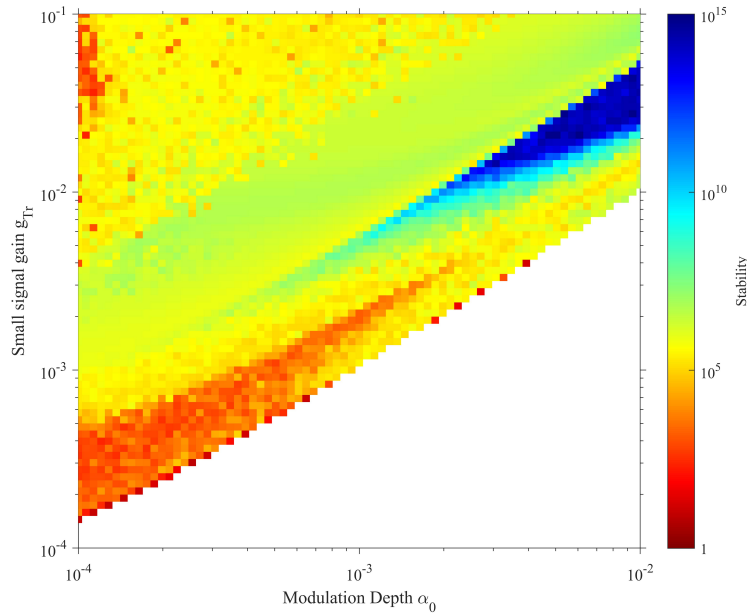


Figure (5.4): Modelocking investigation using stability as criterion. Red areas indicate low stability, meaning that intracavity power is fluctuating a lot, while green areas and the blue areas possess greater stability.

By comparing these three results, a more accurate investigation of device's behavior and modelocking regime can be performed. As a result, regions corresponding to different device's behavior can be individuated and drawn on P_{peak}/P_{ave} graph.

The result is shown on figure 5.5. A detailed explanation of each regime will be given in the following section 5.2.3. Depending on the fineness of the calculation grid, simulation for a single graph as figure 5.5 can take up to a week.

Therefore, by studying different parameters' planes by sweeping parameters two by two accordingly, their relationship and consequences on the behavior and operation of the device can be studied. This, together with the contribution graph, allows deep understanding of how a certain set of parameters affects intracavity field and thoughtful design of a WGM modelocked microlaser can be expected.

5.2.3 Operation regimes

As shown in figure 5.5, different device's operation regimes are individuated:

- Continuous Wave (CW)

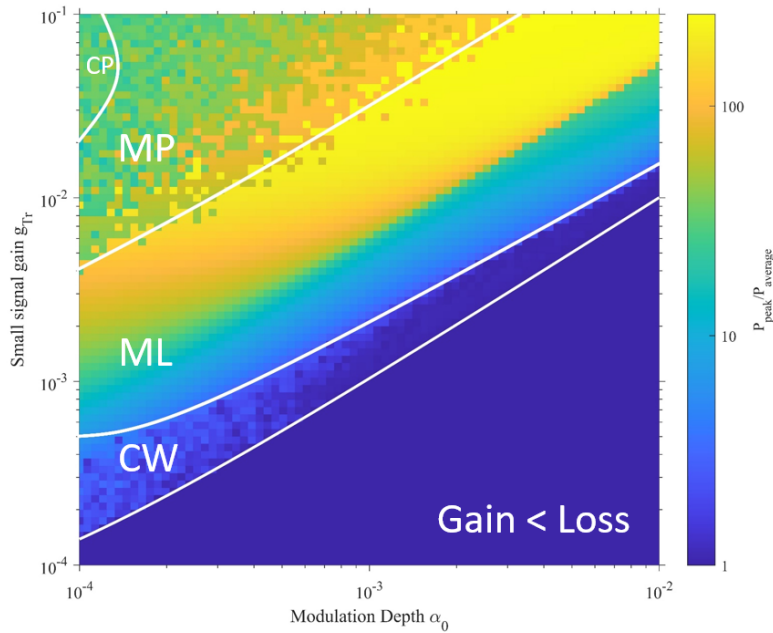


Figure (5.5): Modelocking investigation when combining all three criteria - P_{peak}/P_{ave} ratio, pulswidth and stability - allows categorization of operation regimes. Continuous Wave (CW) operation, Modelocking (ML) regime, Multiple Pulses (MP) and Chaotic (CP) regime are identified.

- Stable Modelocking (ML)
- Multiple Pulses (MP)
- Chaotic Pulses (CP)

In the following, these will be described in details.

Continuous Wave

When in this regime, intracavity power is low and it has not reached SA saturation power, while dispersion is strong and flattens out every attempt of pulse formation. As a result, pulse is not formed, but since gain is higher than the loss CW lasing occurs. As it can be seen in figure 5.6, the saturable absorber does not show any saturation and intracavity power is low. Consequently, intracavity waveform is completely flattened out by dispersion and spectrum is narrow.

Stable Modelocking

In stable modelocking regime (ML), one stable pulse is traveling inside the cavity. This is the result of the balanced action of SPM and dispersion as well as the shape-forming and stabilizing effect of the saturable absorber. According to the balance between these phenomena a more or less sharp pulse is formed. Stability can be verified from the coefficient of variation. In the figure 5.7 an example of stable

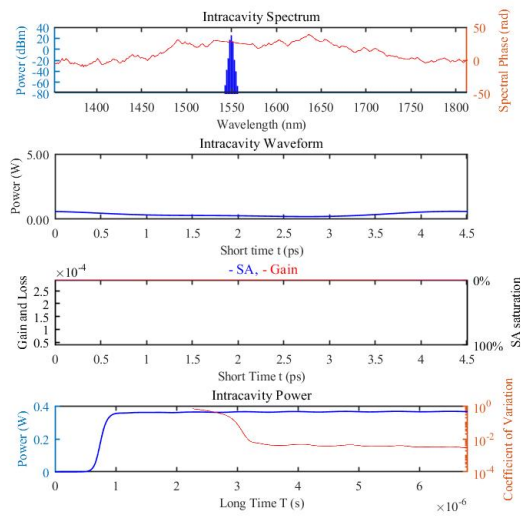


Figure (5.6): Continuous Wave (CW) operation regime.

modelocking is shown. Because of the higher intracavity power compared to the previous example, a good balance between SPM and dispersion is obtained, while the saturable absorber is well saturated. As a result, a sharp pulse is obtained with pulsewidth of a few hundreds of femtoseconds and wide spectral bandwidth.

Stability is confirmed by the low coefficient of variation of $< 10^{-8}$ – and thus stability higher than 10^8 .

When fabricating the device, we are interested in this stable modelocking regime and therefore the design stage will be focused on proposing a modelocked WGM microlaser with parameters that are easily accessible practically.

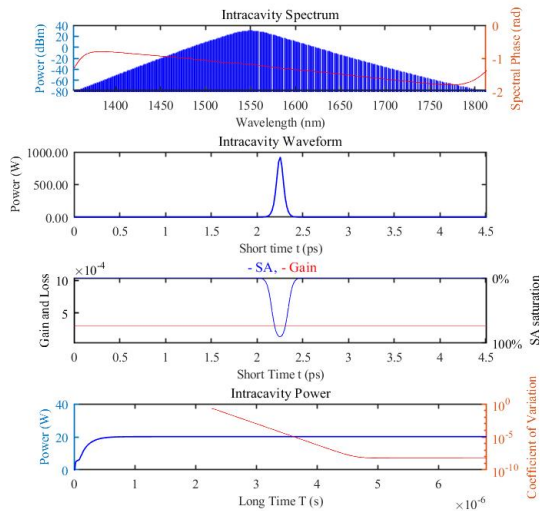


Figure (5.7): Stable Modelocking (ML) operation regime.

Multiple Pulses

When SPM effect is strong, it can cause splitting of the pulse into more pulses, to reach a more stable solution. As a result, multiple pulses travel inside the cavity. Tendency is that such SPM-driven multiple pulses solutions are not very stable, but if stabilizing effect of the saturable absorber is strong enough and dispersion is well balanced it can reach stable solution as in figure 5.8. Here, intracavity power is high and the saturable absorber saturates, encouraging pulse formation. However, SPM effect is too large and it causes splitting of the pulses into two pulses, which are stabilized (stability $\sim 10^7$) by the action of the saturable absorber and dispersion.

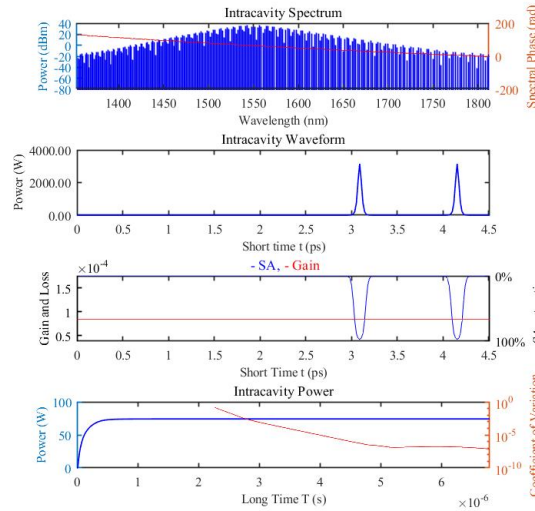


Figure (5.8): Multiple Pulses (MP) operation regime.

Chaotic Pulses

In this regime, SPM effect is too strong and pulse formation is not stable. As a result, there are many unstable pulses that are cyclically generated and quickly destroyed – and a stable solution is not reached. Figure 5.9 shows an example of chaotic pulses (CP). Intracavity power is extremely high and thus SPM is very strong. Therefore, multiple pulses are generated but they cannot stabilize and quickly die out, just to give their energy to new unstable pulses. In fact, coefficient of variation is high ($\sim 10^{-2}$), and thus stability is low ($\sim 10^2$).

5.3 WGM modelocked microlaser design

5.3.1 Small signal gain estimation

Because of the large number of parameters, it is fundamental to be able to estimate some of them, so that parameters' space can be scaled down in dimensions.

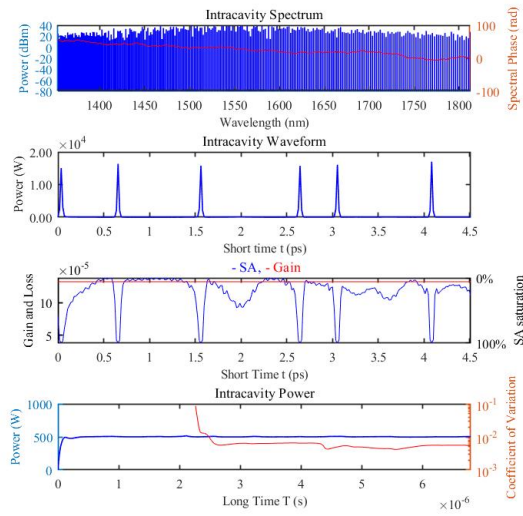


Figure (5.9): Chaotic Pulses (CP) operation regime.

In this case, it is possible to estimate independently to the model, the small signal gain per roundtrip of a given WGM microlaser.

Because of the many ways in which gain inside a cavity can be referred to, definitions of gain terms used in the following of the thesis are given.

When light travels inside a gain medium, its power increases exponentially with its length:

$$P(l) = P(0)e^{gl} \quad (5.5)$$

where g is the small signal gain per unit length (for example [1/cm]).

When light travels a roundtrip length L it experiences a gain per roundtrip of:

$$G_{Tr} = \frac{P(L)}{P(0)} \quad (5.6)$$

and the small signal gain per roundtrip is:

$$g_{Tr} = \frac{\Delta P}{P}(l = L) = G_{Tr} - 1 \quad (5.7)$$

Therefore, the relationship between the small signal gain per unit length, gain per roundtrip, and small signal gain per roundtrip - as defined in this thesis - is:

$$g_{Tr} = G_{Tr} - 1 = e^{gL} - 1 \quad (5.8)$$

The gain can be estimated by solving numerically the rate equation and propagation equation of an erbium doped fiber, supposing that a WGM microlaser is simply a very tiny erbium doped fiber ring laser.

The system of equations is based on propagation equation and rate equation [106]:

$$\begin{cases} \frac{\partial P_p(z,t)}{\partial z} = \rho \Gamma_p \left[\sigma_p^e N_2(z,t) - \sigma_p^a N_1(z,t) \right] P_p(z,t) \\ \frac{\partial P_s(z,t)}{\partial z} = \rho \Gamma_s \left[\sigma_s^e N_2(z,t) - \sigma_s^a N_1(z,t) \right] P_s(z,t) \\ \frac{\partial N_2(z,t)}{\partial t} = -\frac{N_2(z,t)}{\tau} - \frac{1}{\rho A} \left(\frac{\partial P_s(z,t)}{\partial z} - \frac{\partial P_p(z,t)}{\partial z} \right) \\ N_1 + N_2 = 1 \end{cases} \quad (5.9)$$

where P_p and P_s are pump and signal power (in units of photons) respectively, ρ is erbium concentration, Γ is the overlap factor, σ is the absorption/emission cross section, N is the normalized state population density and A is the cross sectional area. Gain cross sections and other parameters not specified are taken from the calculation done for the erbium doped fiber characterization in appendix B.

Figure 5.10 shows numerical results of small signal gain estimation. These results will give an estimate of the gain, to better sweep parameters and to understand realistically where does the device position in the parameters' space. Figure 5.10(a) shows small signal gain per unit length g versus erbium doping concentration. Approaching concentrations of 10^{19} this estimation becomes inaccurate due to erbium ion clustering and quenching which would limit the gain due to energy transfer between excited ions. Figure 5.10(b) graphs the small signal gain per roundtrip against the diameter of the WGM microlaser for different erbium concentrations.

Figure 5.11 shows small signal gain per roundtrip estimations considering a WGM microlaser of $300 \mu\text{m}$ with erbium concentration of $5 \cdot 10^{18}$.

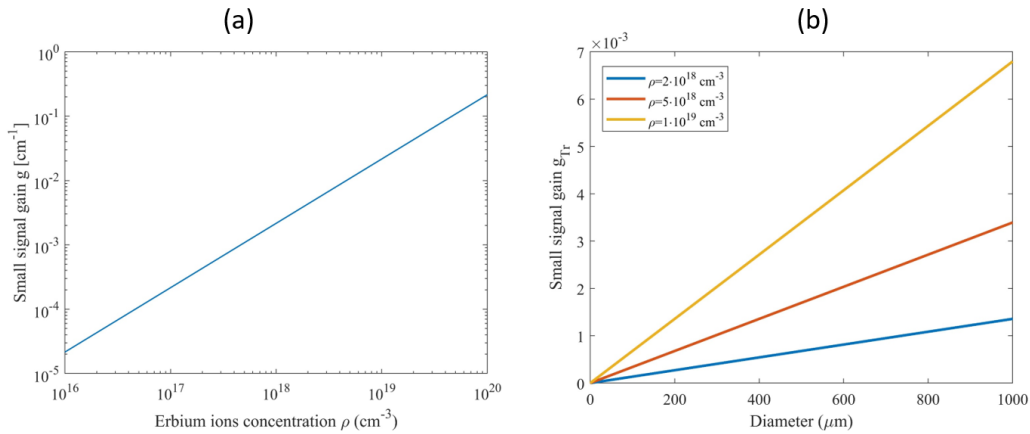


Figure (5.10): (a) Small signal gain per unit length against erbium concentration. (b) Small signal gain per roundtrip against WGM microlaser's diameter at different erbium concentrations. Pump intracavity power is 10W and effective mode area $1 \mu\text{m}^2$.

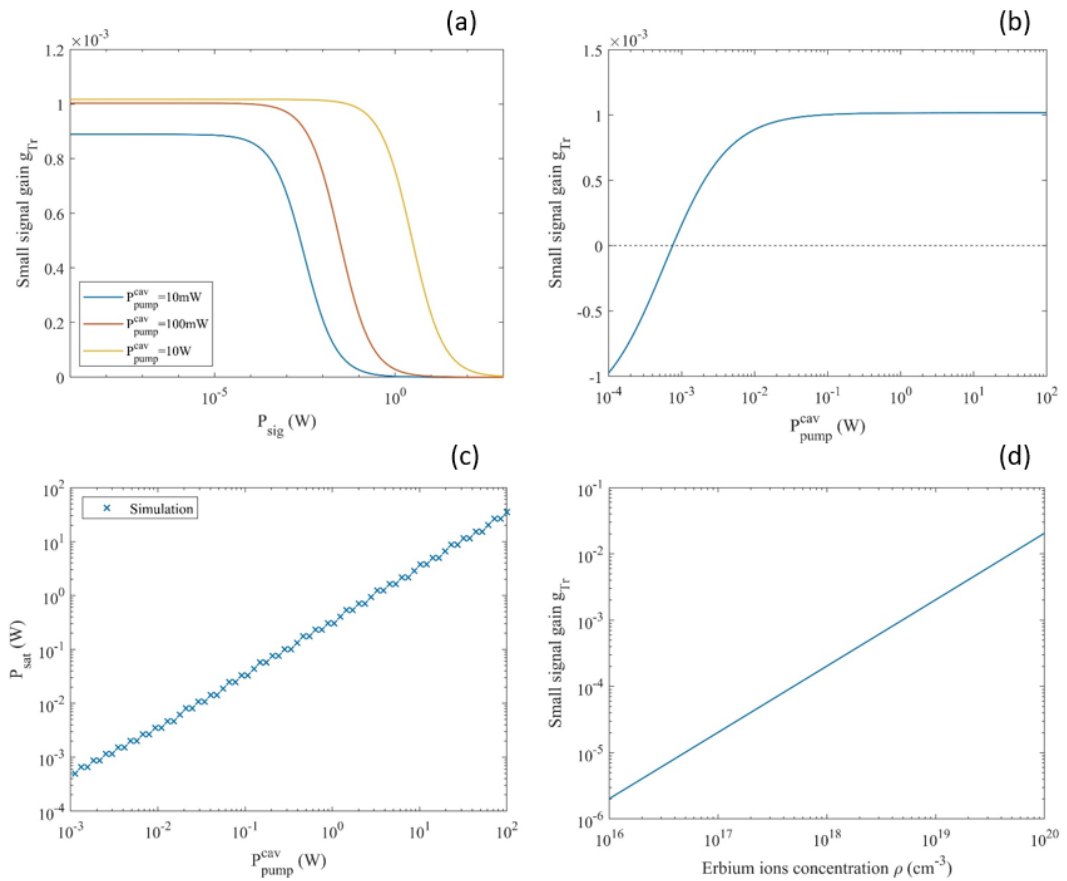


Figure (5.11): (a) Small signal gain per roundtrip against signal power, for different pump powers. Gain saturates and its power increases with pump power. (b) Small signal gain per roundtrip against pump power. Achievable gain per roundtrip reaches a plateau for high pump powers. (c) Signal power saturation against pump power. Power saturation increases proportionally to pump power. (d) Small signal gain per roundtrip against erbium concentration.

5.3.2 Gain and loss

To answer the question on how much erbium and how much carbon nanotubes are needed for modelocking, I performed numerical calculations by considering small signal gain and modulation depth as parameters. Then, the results are plotted as peak to average power ratio in the corresponding parameters' plane. Figure 5.12 shows numerical result for a Q factor of 10^7 and figure 5.13 shows numerical result for a Q factor of 10^8 .

From the graphs it can be inferred that a small signal gain per roundtrip of around ten times the modulation depth will provide sharp and stable modelocking.

However, it is possible to estimate small signal gain – as explained in previous section 5.3.1 - for the cavity of diameter 300 μm considered in this simulation. The red line indicates its estimated gain.

Clearly, gain is limiting factor and an ultra-high Q factor is needed. In fact, for a Q factor of 10^7 , small signal gain provided by erbium ions is sufficient for CW operation, but not enough to reach stable modelocking regime.

On the other side, a Q factor of 10^8 allows modelocking, if modulation depth is adjusted accordingly.

Thanks to its ultra-low intrinsic loss, gain is well above the overall loss - which considers saturable absorber loss too – starting CW lasing. Moreover, this ultra-low loss makes sure that overall loss is dominated by nonlinear loss of the saturable absorber, eventually promoting pulse formation and ML operation over CW operation.

In summary, due to the micrometer size of the device, gain per roundtrip is small and that is the limiting factor for modelocking. As a consequence, ultra-high Q devices ($Q > 10^7$) are necessary for modelocking at low gain; however, the fabrication of such high-Q WGM microresonators is complex and in our lab we can manage to obtain Q factors of around $1 \cdot 10^7$ so far, which throws uncertainty in modelocking a WGM microlaser.

5.3.3 Dispersion

In the previous section, gain and loss parameters contributing to the amplitude of the intracavity field were investigated. However, dispersion – which contributes to the phase of the field – is also known to be a crucial parameter in pulse formation and modelocking.

Therefore, next I performed numerical calculation by considering small signal gain per roundtrip and dispersion (GVD) as parameters. Modulation depth was chosen to a reasonable value of $5 \cdot 10^{-4}$, from figure 5.13. The red dotted lines in figure 5.14(a)-(b) indicate the line along which gain and dispersion are swept in this investigation and the intersection line between the two parameters' plane. Along the red dotted lines, simulation results agree well as expected.

Red continuous line indicates, as in the previous section, the estimated small signal gain. Black dashed line indicates the boundary between anomalous dispersion ($GVD < 0$) and normal dispersion ($GVD > 0$).

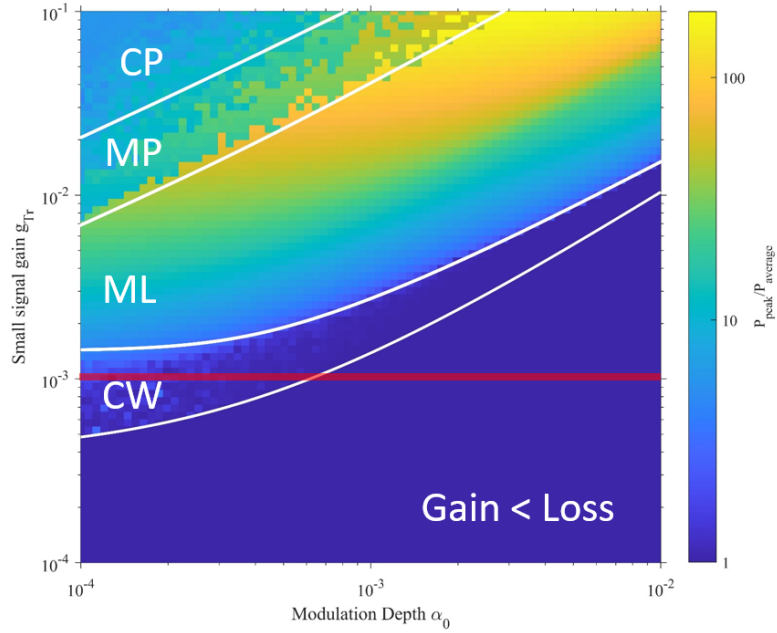


Figure (5.12): Small signal gain g_{Tr} vs modulation depth α_0 for WGM microresonator with Q factor of 10^7 . Red line indicates estimated small signal gain: ML operation cannot be achieved. Diameter is $300 \mu\text{m}$ and dispersion GVD is $-10 \text{ ps}^2/\text{km}$.

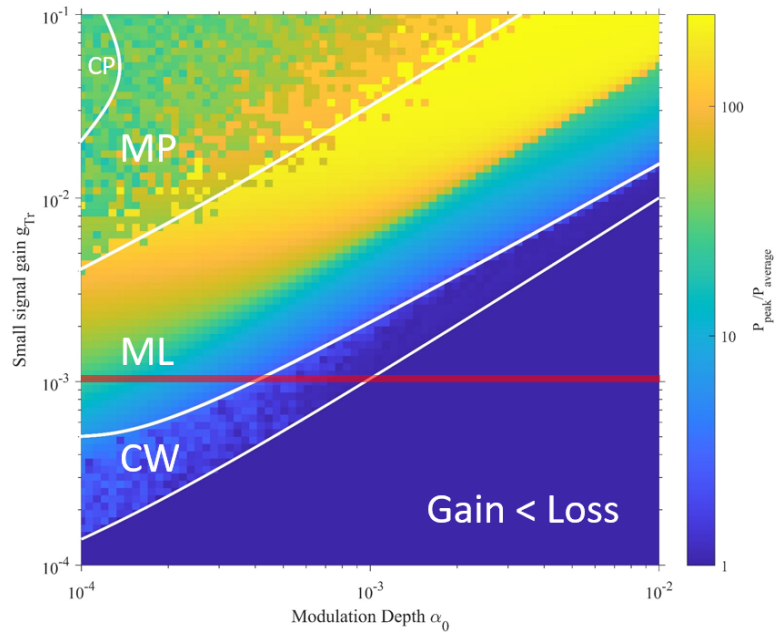


Figure (5.13): Small signal gain g_{Tr} vs modulation depth α_0 for WGM microresonator with Q factor of 10^8 . Red line indicates estimated small signal gain: ML operation can be achieved if α_0 is properly adjusted. Diameter is $300 \mu\text{m}$ and dispersion GVD is $-10 \text{ ps}^2/\text{km}$.

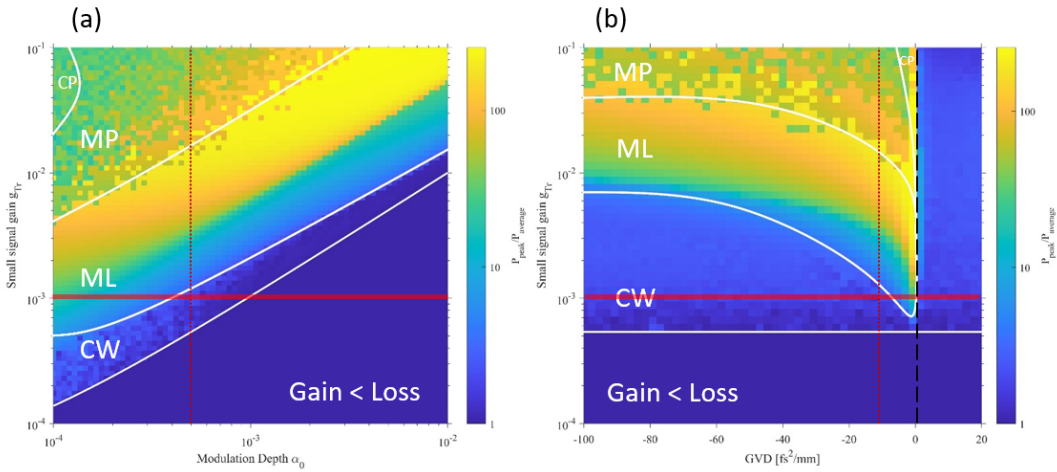


Figure (5.14): (a) Same as figure 5.13. Red dotted line indicates line along which dispersion and gain are swept in graph (b). (b) Small signal gain g_{Tr} vs dispersion GVD. Q factor is 10^8 and modulation depth α_0 is $5 \cdot 10^{-4}$. Red continuous line indicates small signal gain estimation; black dashed line indicates the boundary between anomalous dispersion ($\text{GVD} < 0$) and normal dispersion ($\text{GVD} > 0$). Weak anomalous dispersion allows modelocking at limited gain.

From the dispersion graph on the right it can be concluded that normal dispersion does not allow modelocking, because it does not balance out with self-phase modulation and thus, any attempt of pulse formation is flattened out.

Another important conclusion can be drawn from this graph. In order to modelock at limited gain such as in our case, weak anomalous dispersion is necessary. This might be naturally difficult to understand at first, but with the help of the contribution graph it becomes straightforward.

Figure 5.15 shows a typical contribution graph. When gain is limited, the gain curve translates down, towards the loss curve (1). This means that, because of the saturation of gain, intracavity power at steady state – where gain curve meets loss curve – decreases, which in the graph means that gain-loss crossing point moves to the left (2). Therefore, at weaker intracavity power and, consequently, weaker SPM contribution, dispersion effect has to decrease too, so that good balance for modelocking is obtained. If anomalous dispersion is too strong compared to SPM, its contribution would flatten out any attempt of pulse formation. Therefore, weak anomalous dispersion is necessary for modelocking at limited gain.

Because of the weak SPM and dispersion, the resulting pulse in the modelocking region is mainly formed by the action of the gain and the saturable absorber.

As explained in section 5.3.3, dispersion is the result of chromatic and geometric dispersion. The first one accounts for the frequency dependent nature of refractive index, while the latter accounts for the different light paths that different light frequencies experience. And for silica WGM microtoroids dispersion changes with their diameter, because of the different paths that light takes when varying it.

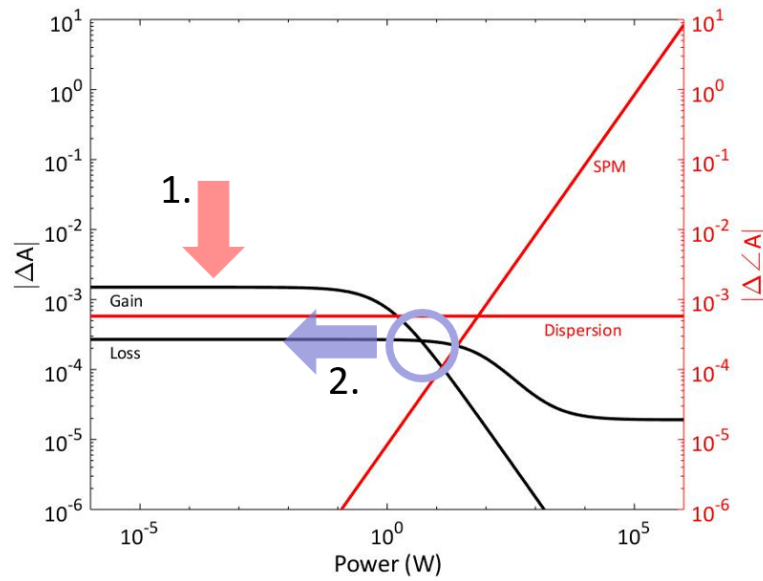


Figure (5.15): Typical contribution graph. It helps understanding why weak anomalous dispersion helps modelocking at limited gain. Lower gain (1) means lower intracavity power (2), thus weak anomalous dispersion is needed not to lose its balance with SPM and flatten out any attempt of pulse formation.

Therefore, WGM microtoroid allows careful dispersion engineering by changing its diameter, in order to tweak its geometric dispersion. Figure 5.16(a) recalls the results in section 5.3.3. Because we are interested in the C-band, figure 5.16(b) shows calculation results of dispersion (GVD) at 1550nm.

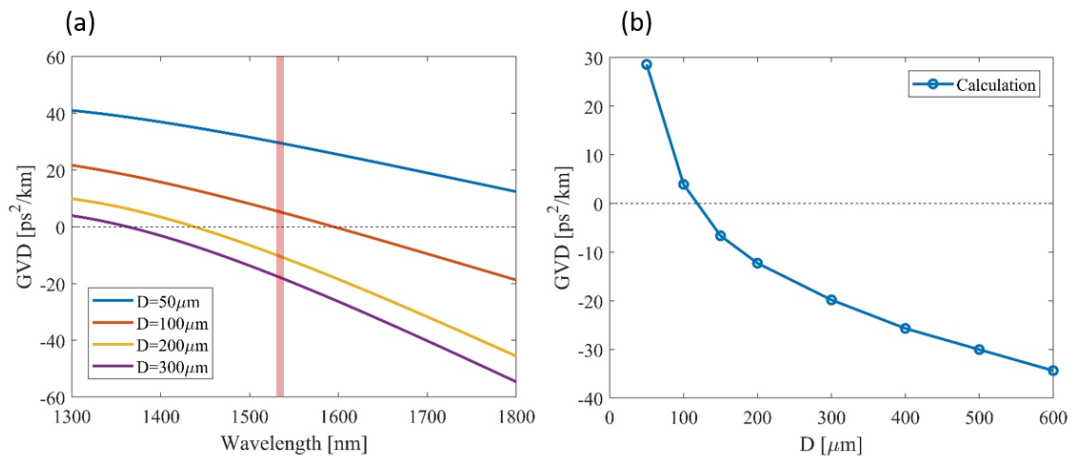


Figure (5.16): (a) Same as figure 2.8. Red line indicates C-band. (b) Calculation results of dispersion (GVD) at 1550nm for different WGM microresonator's diameters.

For a microtoroid of major diameter 300 μm - considered for the simulation result in figure 5.14(b) - a GVD of $-20 \text{ ps}^2/\text{km}$ is calculated. Therefore, as shown in figure 5.17 with a red cross, with estimated gain and calculated dispersion, modelocking

cannot be achieved. Only decreasing its dispersion would allow modelocking. From figure 5.16(b) it can be seen that decreasing the diameter of a WGM microtoroid brings its dispersion towards weak anomalous dispersion.

Therefore, in order to achieve modelocking at limited gain a small diameter WGM microtoroid of around 150 μm with weak anomalous dispersion can be used.

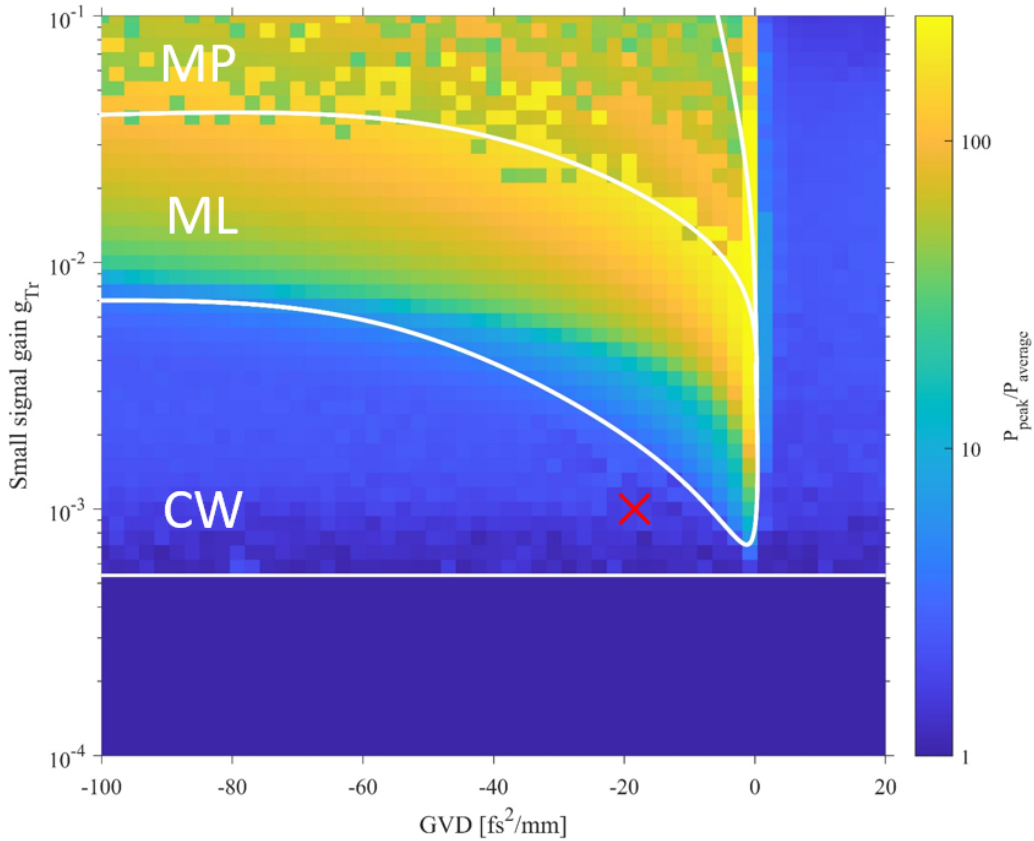


Figure (5.17): Same as figure 5.14(b). Red cross indicates where the simulated WGM microtoroid of diameter 300 μm would position at estimated gain and calculated dispersion. Modelocking cannot be achieved.

5.3.4 Design strategy

In the light of these previous results, we can conclude that there are two improvements that work towards modelocking a WGM microlaser: increase in gain and weak anomalous dispersion. The first allows having a more relaxed condition on the Q factor, while still having a total loss mainly dominated by the nonlinear loss of the saturable absorber. The latter allows modelocking at limited gain and lower intracavity power, without flattening out any attempts of pulse formation.

However, these two strategies are put against with each other in a trade-off relationship by microlaser's diameter. In fact, an increase in diameter will improve small signal gain per roundtrip as in figure 5.10(b), but in turn it will increase anomalous dispersion as in figure 5.16(b).

As a result of this trade-off relationship, there are two design strategies - at polar opposites of this trade-off - that can be taken into consideration:

1. Increase WGM microresonator diameter: by following this strategy increase in gain can be obtained, at the expenses of a larger anomalous dispersion, which working against pulse formation, may ruin any attempt of pulse formation. As a result, modelocking this microlaser may be challenging.
2. Decrease WGM microresonator diameter: by following this strategy, weaker anomalous dispersion for modelocking at limited gain can be obtained. The issue of a smaller gain may be overcome by weak anomalous dispersion, which leaves pulse formation into the hands of gain and nonlinear loss of saturable absorber. This strategy requires careful fabrication for dispersion engineering, but can yield ultra-high repetition rates because of the small size of the cavity.

In order to see which strategy is better, I investigated modelocking regime with three cavities at different diameters of 600 μm , 300 μm and 150 μm . Given the diameter of a WGM microtoroid, estimated gain and calculated dispersion (GVD) are used in the investigation. Modulation depth and Q factor are considered as parameters. Results are shown in figure 5.18.

The objective is to see which microcavity allows modelocking at higher modulation depth and lower Q factor, in order to relax modelocking conditions. This means that microcavity with ML regime that stretches further towards the top left corner of the graph is to be preferred.

The results are self-explanatory. The first design strategy seems to outmatch the second design strategy. A larger WGM microlaser is a better host for pulse formation and stable modelocking.

Increase in diameter leads to greater gain per roundtrip, which plays a bigger role in modelocking compared to dispersion, that also increases but not as much as to flatten out attempts of pulse formation. As a result, modelocking can be achieved at higher modulation depths and lower Q factors.

However, gain itself is not responsible for pulse formation, therefore the reason for better modelocking has to be searched elsewhere. What increased gain really allows, is larger room for larger modulation depth, which is what actually promotes modelocking, overcoming strong anomalous dispersion.

Figure 5.19 shows numerical result when modulation depth and dispersion are considered as parameters. In this case, gain is kept at ten times the modulation depth, so that intracavity power is kept approximately the same and the relationship between modulation depth and dispersion can be studied without worrying that intracavity waveform behavior is caused by non-related phenomena, such as lower intracavity power and consequent loss of SA action.

Although it can be seen that weaker anomalous dispersion allows modelocking at lower modulation depth and therefore lower gain – as predicted by figure 5.17 too – this graph shows how much modulation depth is responsible for pulse formation.

A larger modulation depth promotes ML operation over CW operation. This is evident by observing the graph in the normal dispersion region. Even if the balance

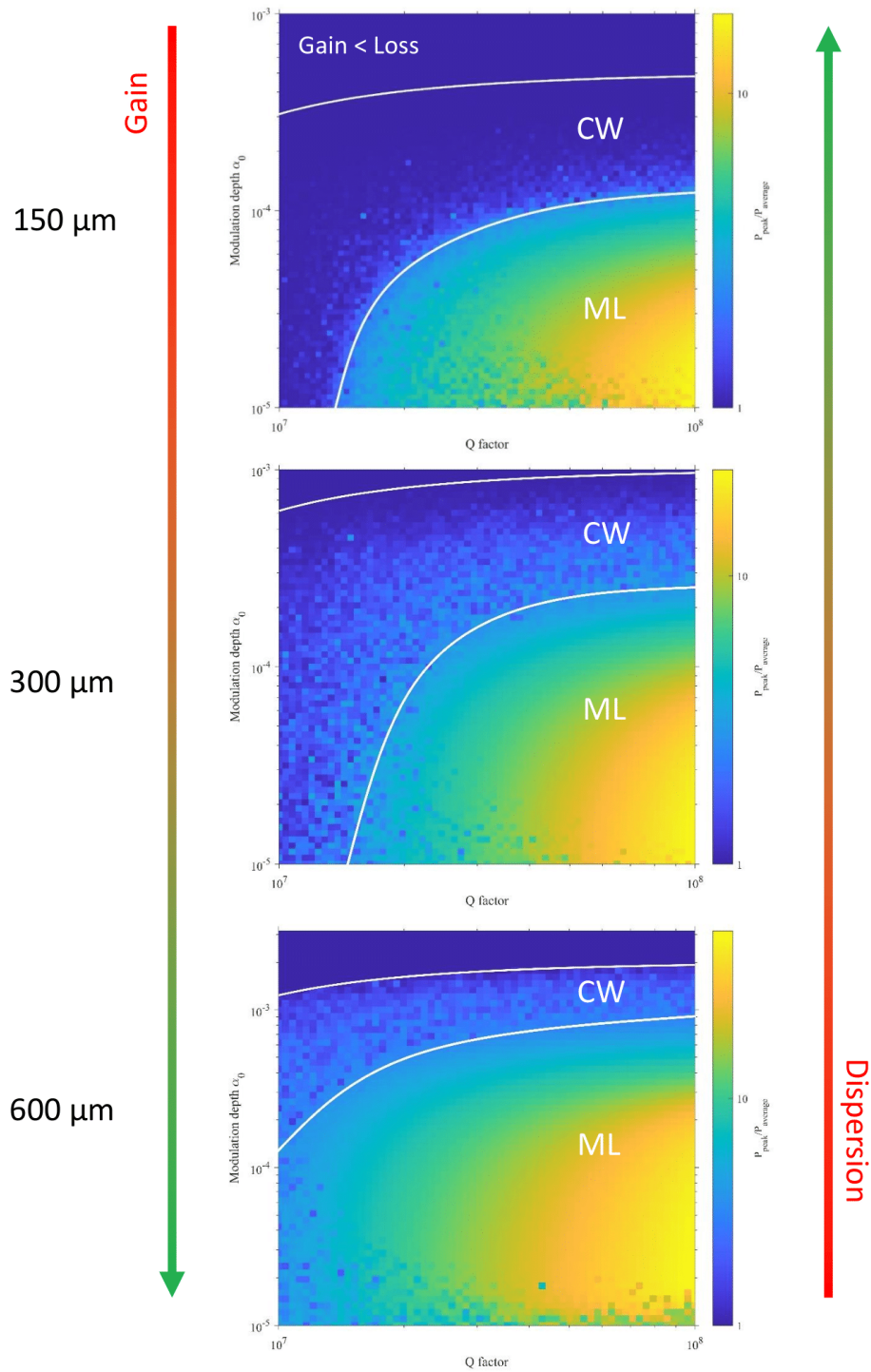


Figure (5.18): Modulation depth α_0 vs Q factor for diameters of 150 μm , 300 μm and 600 μm . Estimated gain and calculated dispersion are used for each WGM microlaser. A diameter of 600 μm allows a more relaxed condition for modelocking, at higher modulation depth and lower Q factor.

between SPM and dispersion is completely lost, large modulation depth can still produce stable modelocking working against the flattening effect of the combined action of SPM and normal dispersion.

Therefore, a large modulation depth actively encourages ML operation over CW operation, even when strong dispersion is working against it. As a consequence, the first design strategy is better for modelocking, because increase in gain per roundtrip by deploying a larger WGM microlaser allows larger “space” for the nonlinear loss of the saturable absorber to act and promote stable pulse formation and ML operation.

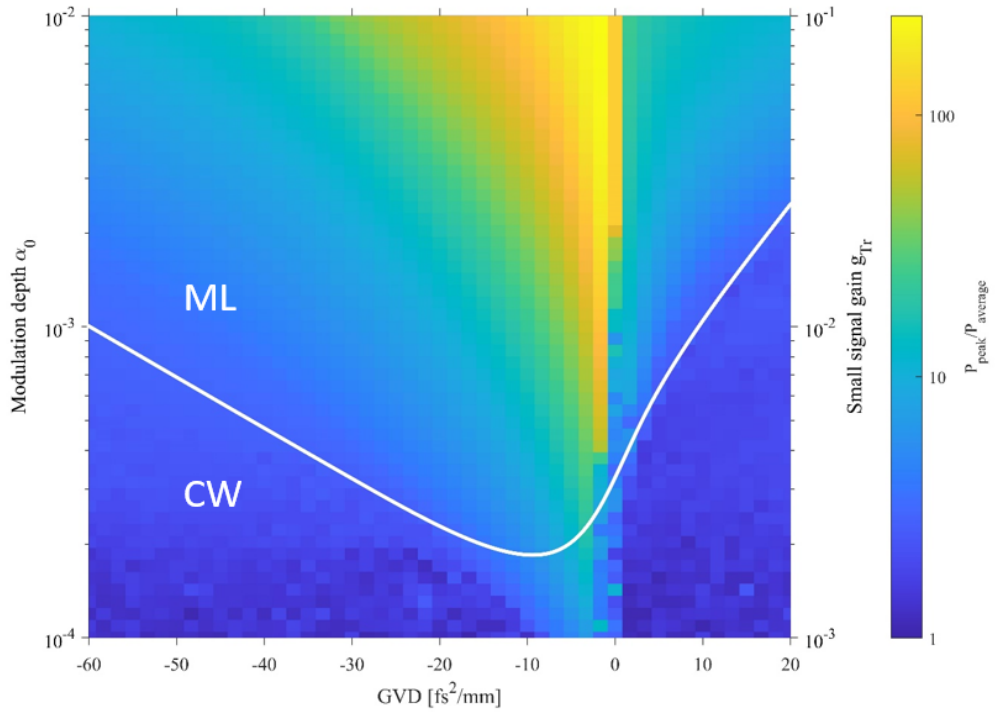


Figure (5.19): Modulation depth α_0 vs dispersion GVD for a WGM microlaser’s diameter of $300\ \mu\text{m}$ and Q factor of 10^7 . Gain g_{Tr} is kept at ten times the modulation depth α_0 . A larger modulation depth promotes ML operation over CW lasing, even in the normal dispersion regime, where balance between SPM and dispersion is completely lost.

5.4 Summary

In this chapter, numerical model of a WGM microlaser modelocked by CNT microprobe was developed and modelocking regime investigated. Tools – such as contribution graph - and methods – such as ML detection approach - were conceived to improve investigation understanding and validity.

A large number of parameters in the model were swept with each other and relationship between them was unveiled. Trade-off relationship between gain and dispersion due to WGM microresonator's diameter is explained and two design strategies at polar opposite of this trade-off are investigated by studying modelocking at different diameters.

Numerical results of such investigation confirm that a large diameter WGM microtoroid (in this study $D=600\ \mu\text{m}$ is considered) is a better host for pulse formation, as it allows modelocking at lower Q factor and higher modulation depth, which in turn strongly promotes ML operation, even at large anomalous dispersion. As a result of this investigation, with a $600\ \mu\text{m}$ diameter WGM microresonator of Q factor of 10^7 , which can be fabricated in our lab, $>100\ \text{GHz}$ pulsed operation can be achieved by properly adjusting the modulation depth with a CNT microprobe at $\sim 10^4$.

Chapter 6

Summary, future works and outlook

This chapter will summarize the work reported in this thesis and raise some questions that need to be addressed in the future works. Finally, an outlook on the future of WGM modelocked microlaser is given.

6.1 Summary

This thesis reported the background, introduction to the research and theory of WGM microresonators in Chapter 1 and 2. Chapter 2 also introduced WGM microlasers and two CW laser platforms – silica WGM microsphere and silica WGM microtoroid - were demonstrated. Extremely high-Q factors of 10^7 allow ultra-low threshold powers at $1\ \mu\text{W}$. These WGM microlasers are the starting point of my research, which is to passively modelock these devices for pulsed operation.

Chapter 3 focuses on the integration of a saturable absorber to a WGM microlaser. A broad overview on saturable absorbers is given and single-walled carbon nanotubes (SWCNT) are designated as saturable absorber for my study.

Next, two CNT integration methods are proposed: CNT tapered fiber and CNT microprobe. Both are fabricated and evaluated to see which method is more suitable. The latter method demonstrates better saturable absorption properties with the possibility to adjust its nonlinear loss parameters by only changing microprobe's position, in order to meet modelocking requirements of a WGM microlaser in a very convenient way.

Since erbium doping technique and CNT integration method are both developed, design of WGM modelocked microlaser is necessary to understand quantitatively how to make them work together. Chapter 4 and 5 describe numerical work performed to design a WGM modelocked microlaser.

Chapter 4 focuses on the realization of a reliable model based on Nonlinear Schrödinger Equation by case studying a modelocked fiber ring laser.

In order to study its reliability, a fiber ring laser modelocked by carbon nanotubes as saturable absorber was realized, its parameters for simulation retrieved experimentally and its properties evaluated. Finally, simulation results and experimental results were compared and the model verified to be reliable.

Chapter 5 focuses on modelocking investigation of a WGM microlaser by miniaturizing the model realized in chapter 4. Tools and methods are developed to improve understanding and investigation's validity.

Relationship between many parameters of the device are investigated and unveiled. Most importantly, the trade-off relationship between gain and dispersion given by WGM microtoroid diameter is explained and two design strategy are proposed at opposite poles of this trade-off.

Numerical results confirm that gain plays a bigger role in modelocking a WGM microlaser compared to dispersion, because of the larger "space" given to the nonlinear loss of the saturable absorber to act as pulse formation mechanism. In view of these considerations, a design proposal is given which would yield pulsed operation at above 100 GHz of repetition rate, by modelocking a high-Q large diameter WGM microlaser with CNT microprobe.

6.2 Future works

This work provides the tools, methods and a design strategy of a WGM modelocked microlaser.

However, there are many challenges to face and overcome. This thesis focuses on the fabrication and design stage of the deliberated research roadmap. Evaluation stage is needed to link fabrication stage and design stage, in order to optimize the process.

Here, small signal gain was estimated by considering absorption and emission cross sections of a standard erbium doped fiber. Experimental evaluation of the small signal gain of a WGM microlaser is necessary for more accurate estimation.

Since sol-gel process is used for introducing erbium ions, doping quality may be studied. As a result, gain may be further limited and below the estimation. Therefore, in order to increase the gain without affecting the repetition rate of the WGM mode-locked microlaser, alternative approaches can be undertaken. Possible approaches are ytterbium co-doping [59] – which has a larger absorption cross section and allows higher doping, so that higher gain can be achieved – and improving erbium quenching – by, for example, introducing aluminum ions in the sol-gel process which coordinate erbium ions to avoid their clustering [107].

Figure 6.1 shows the effects of gain in modelocking a WGM microlaser. This numerical result is obtained by considering small signal gain and Q factor as parameters for a WGM microresonator of diameter 600 μm . Modulation depth is fixed to 10^{-4} . Red line indicates estimated gain, used in the numerical result shown in the bottom inset of figure 5.18.

As it can be clearly seen on graph, gain plays an important role in relaxing Q factor conditions for modelocking. Therefore, experimental small signal gain evaluation will allow accurate gain estimation for improving device's performance.

As discussed in the design stage, a large diameter WGM microtoroid is necessary to experimentally achieve modelocking, because its increase in gain per roundtrip allows more “room” for modulation depth to act as pulse formation mechanism.

Moreover, large diameter microtoroids are better hosts for high-power WGM microlasers, which has to be developed in our lab, so that intracavity power reaches SA saturation power levels and it meets modelocking requirements.

Hence, fabrication-wise, a large diameter WGM microtoroid has to be developed. In our lab small diameter WGM microtoroids can be fabricated by CO₂ laser reflow, however large diameter toroids pose increased complexity in the CO₂ laser reflow system because of their larger size, relatively to the spot size of the laser.

Therefore, if reflow is not straightforward with large diameter toroids, new techniques for laser reflow – such as circularly moving the stage during laser reflow in order to selectively reflow the circumference of the disk – need to be considered [108, 109, 41].

Pulsed operation in C-band is fundamental for optical communication; however, other applications such as laser processing do not have strict operation wavelength requirements.

Therefore, changing gain dopant and lowering lasing wavelength may allow further optimization of pulsed operation by improving dispersion property without changing diameter and affecting gain factor of the WGM microresonator, as shown in figure 5.16.

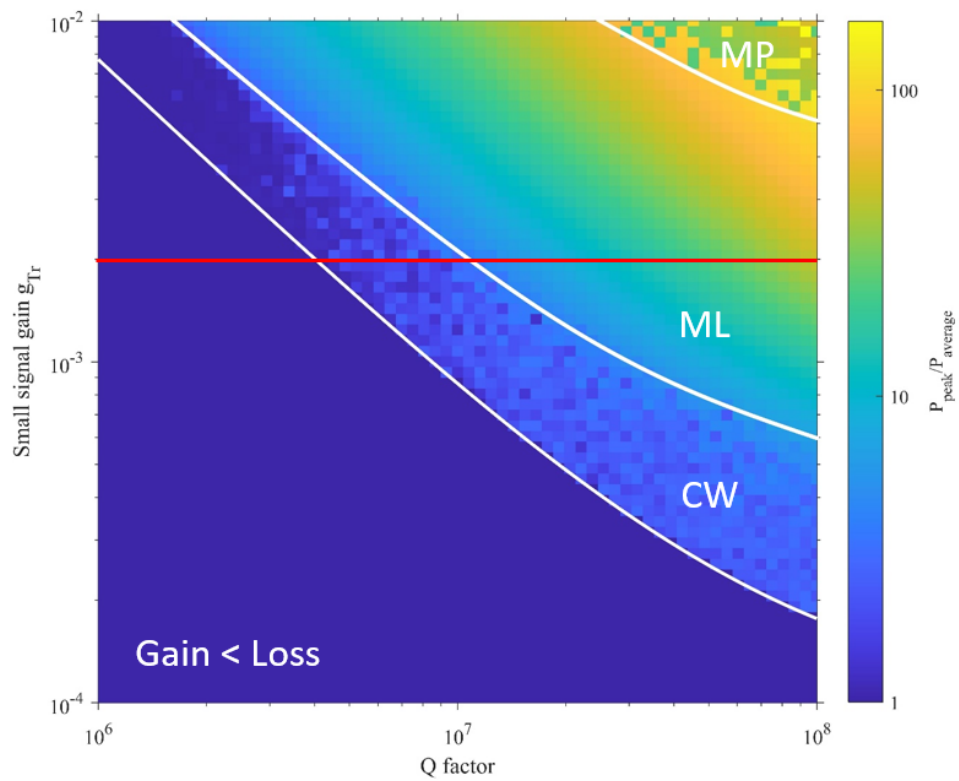


Figure (6.1): Small signal gain g_{Tr} vs Q factor for a WGM microlaser's diameter of $600 \mu\text{m}$. Modulation depth is 10^{-4} . Red line indicates estimated gain. Larger gains compared to the estimated value allow modelocking at lower Q factor; on the other hand, smaller gains compared to estimated value necessitate of higher Q factor for modelocking.

CNT microprobe integration method is ideal in the first stages of modelocking as it allows adjusting saturable absorber parameters in a very convenient way; however, it comes with a drawback.

It needs an ulterior stage for spatial control of the microprobe, increasing complexity of the device and affecting reproducibility of modelocking.

Moreover, its saturable absorber properties should be studied and evaluated when interacting with a WGM microtoroid, as in [84]. This poses new challenges in the experimental setup for evaluation, but it would prove very useful to estimate SA parameters more accurately and for weaker interactions between light and CNTs, in order to better link fabrication and design stage.

As for the design stage, many other parameters can be studied and their relationship investigated – such as gain and saturable absorber power saturation, recovery time [103] and so on.

Particular attention needs to be addressed to the non-saturable absorption. In this work, it was always considered non-existent in view of a simpler investigation; however, in reality non-saturable losses can be significant and degrade Q factor to an extent for which ML operation is not possible, as it steals “room” for modulation depth to act as pulse formation mechanism.

It has been shown that saturable to non-saturable loss ratio increases with evanescent field interaction [75], but further studies are needed to assess non-saturable loss in CNT microprobe. This would allow a more accurate design work that takes into account non-saturable losses of carbon nanotubes.

Lastly, a more meticulous model can be created by taking into account two phenomena that are ignored in this essential model: gain dynamics [110] and CW-CCW lasing operation [111, 112, 113].

The second is of uttermost importance because investigation of WGM mode-locked microlaser is based on the miniaturization of a modelocked fiber ring laser. However, in a fiber ring, an isolator is inserted in the cavity to suppress bidirectional operation. This cannot be easily done inside a WGM microresonator.

Therefore, investigating bidirectional operation in WGM microresonator may help understanding its consequences to device’s performance and advice a solution to this concern.

6.3 Outlook

Since their invention, pulsed lasers have rapidly increased their reputation, from being labeled “a solution seeking a problem” at first, to later spread a revolution in science and industry. Now many scientific discoveries depend upon pulsed lasers and industrial processes are increasingly based on pulsed lasers.

It is inevitable to think that, in the near future, we will expand the horizon of possible applications of pulsed lasers towards every-day life technologies.

In view of that, cost-effective and on-chip integrable high repetition rate mode-locked lasers are crucial components of this revolution and this work is an attempt to

provide a solution. WGM microlaser modelocked by carbon nanotubes as saturable absorber is potentially a cheap and on-chip platform for high repetition rate pulsed laser.

Therefore, I believe it is important to further research on it and achieve mode-locked pulsed operation, with a long-sighted perspective on how every-day technologies can benefit from it.

Appendix A

Marangoni effect

Marangoni effect is a very relevant phenomenon in electronics and manufacturing industries, because of its importance in fields like welding, crystal growth and heat radiation – just to name a few.

Recently, Marangoni effect has also been studied in microgravity on the International Space Station (ISS), in order to improve its understanding. That is how impactful Marangoni effect is in the development of future technologies.

Marangoni effect is named after the Italian physicist Carlo Marangoni, who studied it in 1865, but it is also alternatively called “tears of wine” effect, as it can be easily observed in a glass of wine.

Marangoni effect is the mass transfer along an interface due to a gradient in surface tension. In the case of “tears of wine” effect, while wine rises up the surface of the glass due to capillary action, alcohol (which exhibits higher volatility) evaporates, leaving behind a waterier solution with higher surface tension. This, due to Marangoni effect, further pulls up solution with lower surface tension (and higher concentration of alcohol) until its own weight causes it to drop back to the wine, in form of tears.

When the gradient of surface tension is caused by temperature, Marangoni effect is also known as thermos-capillary convection.

This is the case that I have observed during optical deposition of CNT tapered fiber. In fact, high power laser input causes the side of the droplet facing towards the laser to heat up, while its back is relatively cold. Because surface tension depends on temperature as:

$$\sigma(T) = \sigma_0 - bT \quad (\text{A.1})$$

the front of the droplet results in lower surface tension than the back. In eq. A.1 σ is the surface tension, T is the temperature and b is a coefficient.

As a result, there is a net mass transfer (see figure A.1(a)) towards the back of the droplet. Because the position of the droplet is fixed by the slide glass where it is positioned and the tapered fiber gives an escape path for the net mass transfer (see figure A.1(b)), solution accumulates on the tapered fiber and eventually forms droplets to minimize its surface energy. Figure A.2 shows the evolution in time of Marangoni effect during optical deposition of carbon nanotubes on tapered fiber, for different input powers.

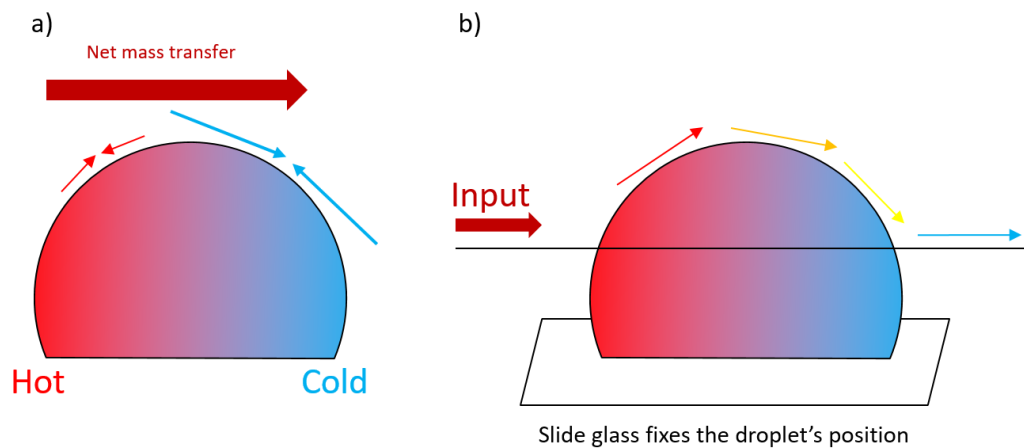


Figure (A.1): *a) Illustration of Marangoni effect in droplet with temperature gradient. b) Illustration of Marangoni effect during optical deposition of carbon nanotubes on tapered fibers. The latter provides an escape path for the net mass transfer, which then forms small side droplets along the fiber.*

This phenomenon is unwanted in my experiments as explained in section 3.4.1, but it can be very useful in many fields of physics and biology for light-matter interaction and manipulation - such as for droplet transport along thin fibers [91, 89] and gas bubbles formation and manipulation [90].

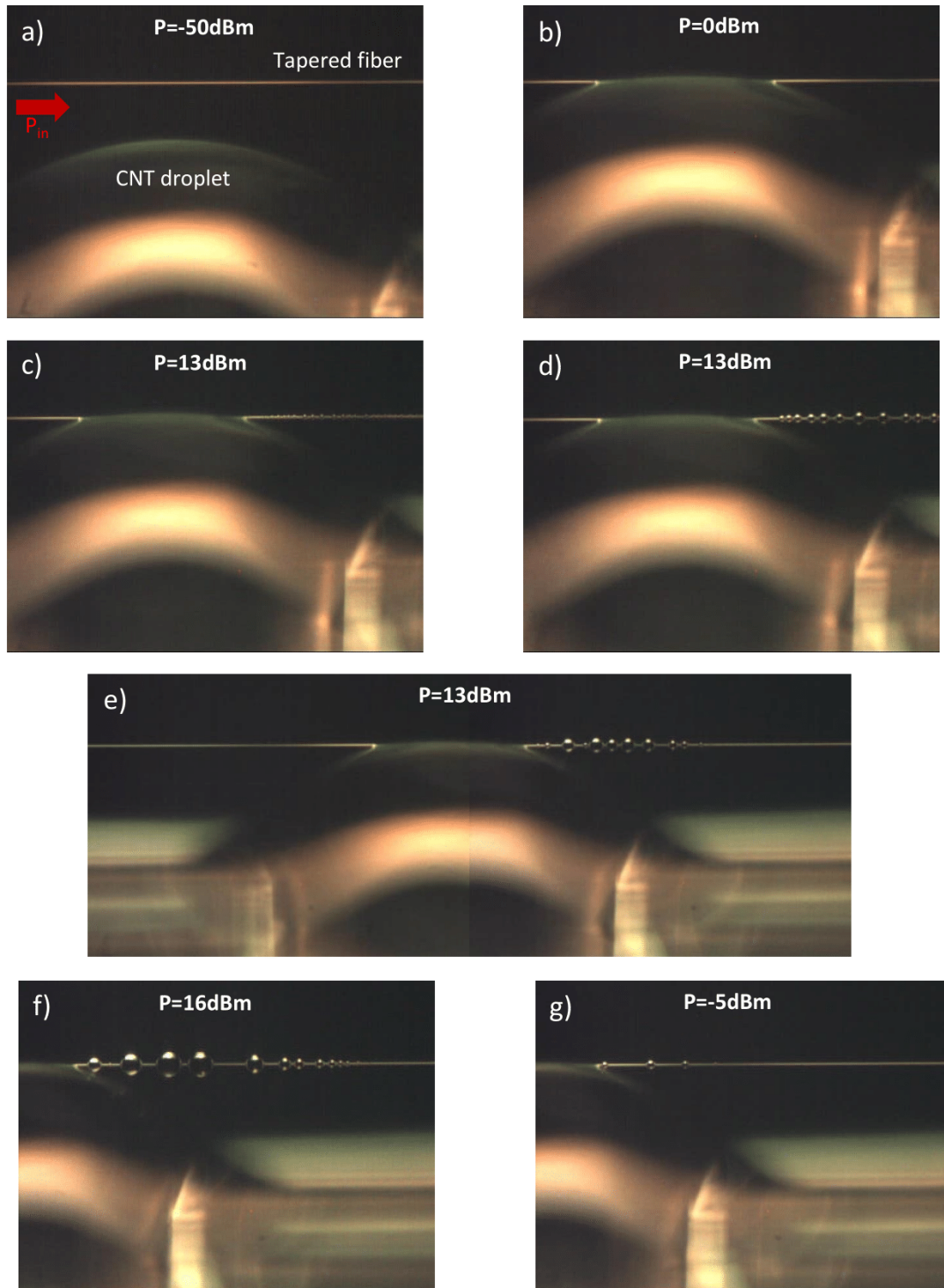


Figure (A.2): Evolution in time of Marangoni effect during optical deposition on tapered fiber. a) Shows initial condition for optical deposition. b) For low input powers ($P=0 \text{ dBm}$), small side droplets due to Marangoni effect are not observed. c) For higher input powers ($P=13 \text{ dBm}$), small droplets start to form along the tapered fiber on the colder side of the main droplet. d) Side droplets increase in size with time. e) Full picture at $P=13 \text{ dBm}$. Small droplets are observed only on the colder side of the main droplet, confirming Marangoni effect hypothesis. f) Further increase of input power causes larger and more extended side droplets along the tapered fiber. g) When power is decreased again below the threshold power for Marangoni effect to happen, side droplets slowly evaporate and vanish.

Appendix B

Er-doped fiber simulation

In section 4.2.1, 3 meters of Er-doped fiber were characterized experimentally, in order to retrieve parameters for simulation. In the following, numerical calculation is performed to verify experimental results. Calculation of gain of erbium doped fiber is done by numerically solving propagation equation together with the rate equation [106]:

$$\begin{cases} \frac{\partial P_p(z,t)}{\partial z} = \rho \Gamma_p \left[\sigma_p^e N_2(z,t) - \sigma_p^a N_1(z,t) \right] P_p(z,t) \\ \frac{\partial P_s(z,t)}{\partial z} = \rho \Gamma_s \left[\sigma_s^e N_2(z,t) - \sigma_s^a N_1(z,t) \right] P_s(z,t) \\ \frac{\partial N_2(z,t)}{\partial t} = -\frac{N_2(z,t)}{\tau} - \frac{1}{\rho A} \left(\frac{\partial P_s(z,t)}{\partial z} - \frac{\partial P_p(z,t)}{\partial z} \right) \\ N_1 + N_2 = 1 \end{cases} \quad (\text{B.1})$$

where P_p and P_s are pump and signal power (in units of photons) respectively, ρ is erbium concentration, Γ is the overlap factor, σ is the absorption/emission cross sections, N is the normalized state population density and A is the cross sectional area.

Numerical results are shown in figure B.1. Experimental behavior of erbium doped fiber is numerically predicted.

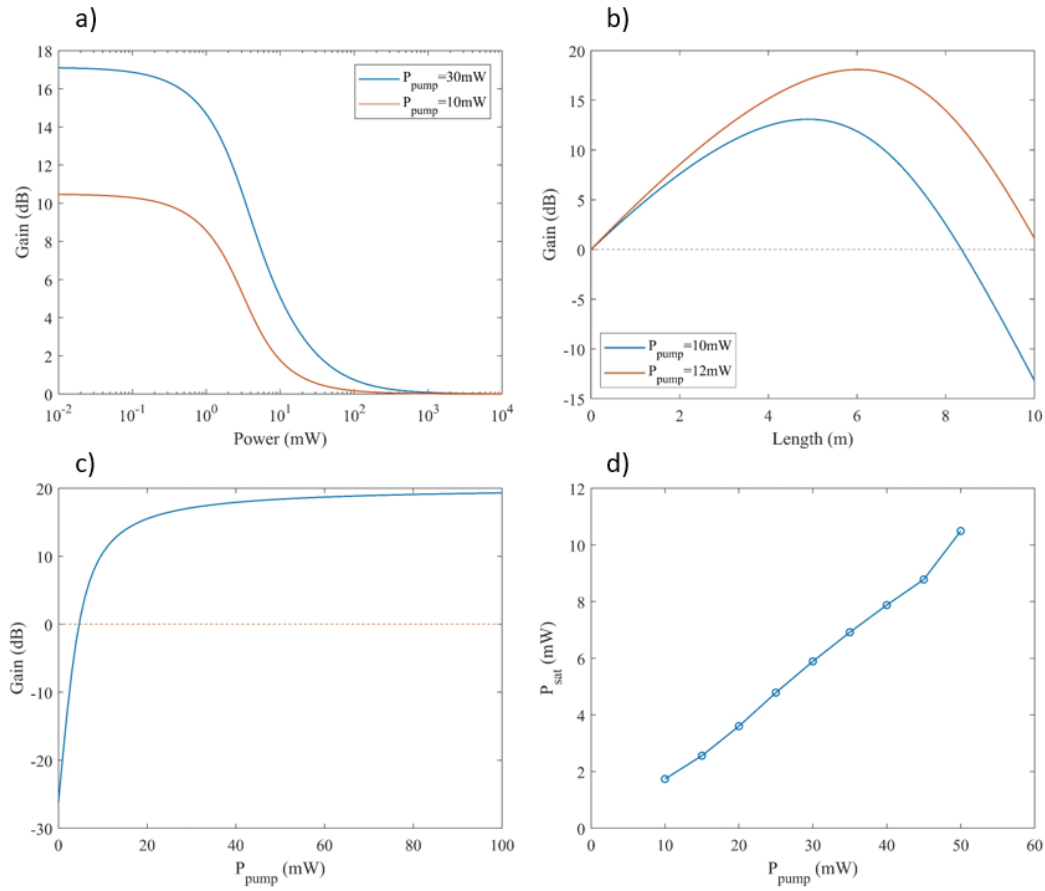


Figure (B.1): Simulation parameters are: $\rho = 1.9 \cdot 10^{19} \text{ cm}^{-3}$, $\tau = 10 \text{ ms}$, $A = 12.5 \text{ }\mu\text{m}^2$, $\Gamma = 0.4$. Gain cross sections are: $\sigma_p^a = 1.5 \cdot 10^{-25} \text{ m}^2$, $\sigma_p^e = 0.8 \cdot 10^{-25} \text{ m}^2$, $\sigma_s^a = 2.8 \cdot 10^{-25} \text{ m}^2$, $\sigma_s^e = 4.8 \cdot 10^{-25} \text{ m}^2$. a) Gain vs signal power: Gain saturation is observed. b) Gain vs length: given a pump power, there is an optimal length of erbium doped fiber for maximum gain. c) Gain vs pump power: Increase in pump power results in higher gain, but it will eventually saturate. d) Gain saturation power vs pump power: P_{sat}^g is proportional to pump power.

Appendix C

SA parameters relationship

As shown in section 3.1, saturable absorbers can be explained by:

$$\alpha(I) = \alpha_{ns} + \frac{\alpha_0}{1 + \frac{I}{I_{sat}}} \quad (\text{C.1})$$

where α_{ns} is the non-saturable loss, α_0 is the modulation depth, I_{sat} is the saturation intensity.

Non-saturable absorption α_{ns} is the fraction of absorption that is not power dependent and it cannot be saturated by increasing light intensity. Modulation depth α_0 is the fraction of absorption that is power dependent and can be saturated by increasing light intensity. α_{ns} and α_0 make up the total absorption.

I_{sat} describes the intensity of impinging light at which the absorber saturates – precisely to half of its modulation depth.

It is therefore intuitive to think that these parameters are related to each other by the amount of saturable absorber that interacts with impinging light. If that amount is small, absorption loss will be smaller – and consequently α_{ns} and α_0 too – and weaker intensities are needed to saturate the absorber.

On the other hand, if the amount of saturable absorber that interacts with light is large, absorption loss will be greater – and thus α_{ns} and α_0 too – and stronger light intensities will be needed to saturate it.

In the following, saturable absorber parameter's relationships are experimentally investigated for the case of carbon nanotubes. Transmission experiment at varying input powers for different optically deposited CNTs on fiber ferrule (as in section 4.2.2) is performed. Then by fitting with eq. C.1, SA parameters are retrieved and their relationship investigated.

Figure C.1 shows different saturable absorption curves of different samples. Figure C.2 shows SA parameter's relationship for CNT samples under test. Total absorption – sum of modulation depth α_0 and non-saturable absorption α_{ns} – is used as a measure of CNTs interacting with impinging light. As described earlier, experiments confirm that as the extent of CNT interaction with light increases, saturable absorber parameters – non-saturable absorption, modulation depth and saturation intensity – increase [114].

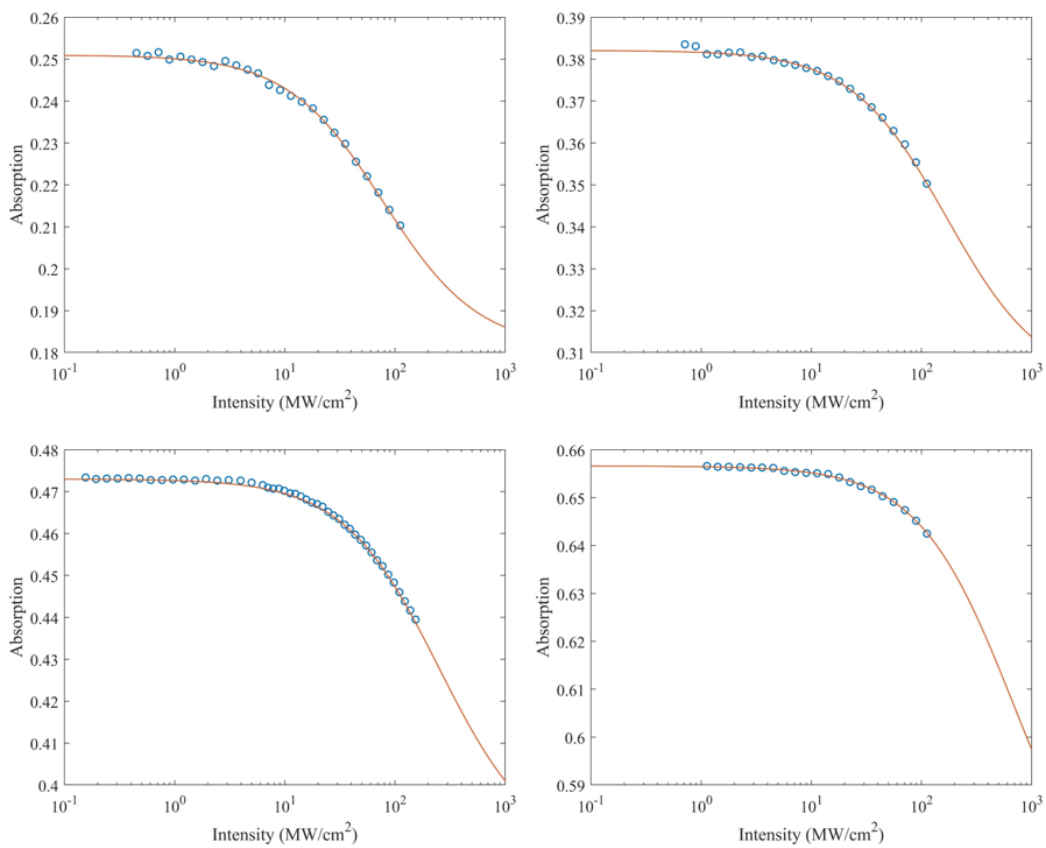


Figure (C.1): SA curves for different CNT samples on fiber ferrule, fabricated by optical deposition. By fitting with eq. C.1, saturable absorber parameters can be retrieved.

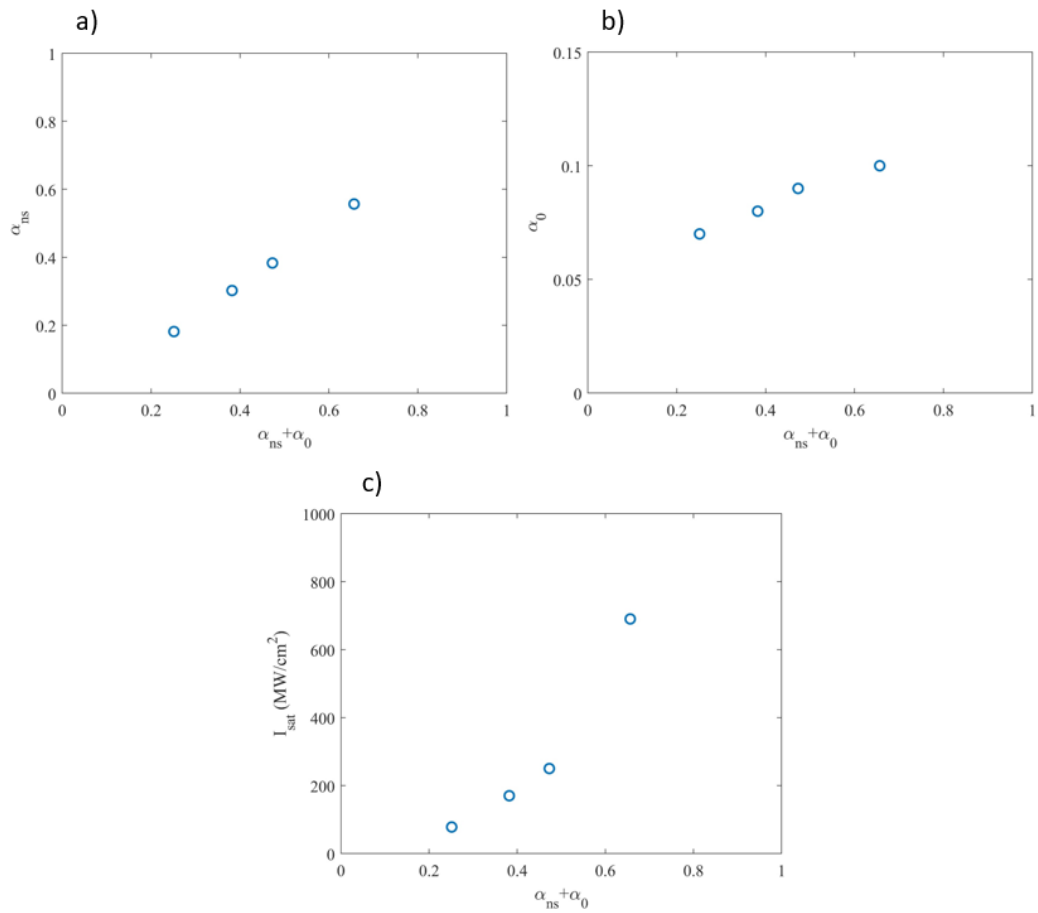


Figure (C.2): Total absorption - sum of non-saturable absorption and modulation depth α_0 - is used as a measure of CNT interaction with light. Non-saturable loss (a), modulation depth (b) and saturation intensity (c) proportionally increase with larger CNT-light interaction.

Appendix D

Gain and SA power saturation

Gain power saturation and saturable absorber power saturation are also important parameters for modelocking in WGM microlasers. Section 5.1 include them in the model used for modelocking investigation.

Here, I report numerical result of modelocking investigation when gain power saturation and saturable absorber power saturation are used as parameters. Figure D.1 shows investigation result. A gain to SA power saturation ratio of ~ 100 yields stable modelocking. Therefore, in numerical results in chapter 5, gain power saturation and saturable absorber power saturation are fixed taking into account this ratio, at values that are reasonable with experiments and estimations.

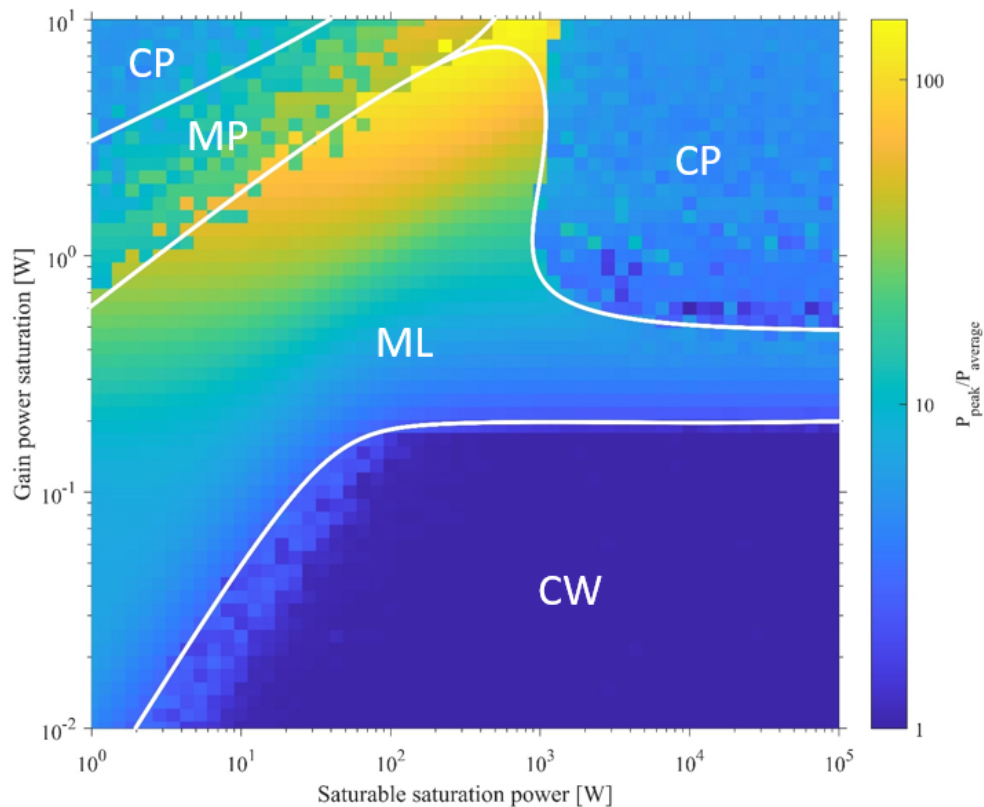


Figure (D.1): Gain power saturation vs saturable absorber power saturation. Q factor is 10^7 and small signal gain is ten times the modulation depth. The strange shape of the modelocking region is due to the fact that the peninsula stretching towards the right side of the graph is stably modelocked by the good balance between SPM and dispersion. In this case, the saturable absorber is not helping pulse formation and stabilization, as its saturation power is well above the intracavity power. In fact, beyond SA power saturations of 10^3 W, the saturable absorber is not saturated at these gain values due to limited intracavity power. As a result, in this region modelocking is only determined by the balance between SPM and dispersion. Below ML region, dispersion is too strong and CW operation is promoted; above ML region, SPM is too strong and it enters into a chaotic regime (CP).

Bibliography

- [1] R. Ell, U. Morgner, F. X. Kärtner, J. G. Fujimoto, E. P. Ippen, V. Scheuer, G. Angelow, T. Tschudi, M. J. Lederer, A. Boiko, and B. Luther-Davies, “Generation of 5-fs pulses and octave-spanning spectra directly from a Ti:sapphire laser,” *Optics Letters* **26**(6), p. 373, 2001.
- [2] T. Südmeyer, F. Brunner, E. Innerhofer, R. Paschotta, K. Furusawa, J. C. Baggett, T. M. Monro, D. J. Richardson, and U. Keller, “Nonlinear femtosecond pulse compression at high average power levels by use of a large-mode-area holey fiber,” *Optics Letters* **28**(20), p. 1951, 2003.
- [3] L. Krainer, R. Paschotta, S. Lecomte, M. Moser, K. Weingarten, and U. Keller, “Compact Nd:YVO/sub 4/ lasers with pulse repetition rates up to 160 GHz,” *IEEE Journal of Quantum Electronics* **38**(10), pp. 1331–1338, 2002.
- [4] U. Keller, “Recent developments in compact ultrafast lasers,” *Nature* **424**(6950), pp. 831–838, 2003.
- [5] P. Elahi, C. Kerse, H. Hoogland, Ö. Akçaalan, D. K. Kesim, B. Çetin, R. Holzwarth, F. Ö. Ilday, B. Öktem, M. D. Aşık, S. Yavaş, and H. Kalaycıoğlu, “Ablation-cooled material removal with ultrafast bursts of pulses,” *Nature* **537**(7618), pp. 84–88, 2016.
- [6] S. H. Chung and E. Mazur, “Surgical applications of femtosecond lasers,” *Journal of Biophotonics* **2**(10), pp. 557–572, 2009.
- [7] F. H. Loesel, J. P. Fischer, M. H. Götz, C. Horvath, T. Juhasz, F. Noack, N. Suhm, and J. F. Bille, “Non-thermal ablation of neural tissue with femtosecond laser pulses,” *Applied Physics B: Lasers and Optics* **66**(1), pp. 121–128, 1998.
- [8] L. F. Mollenauer, P. V. Mamyshev, J. Gripp, M. J. Neubelt, N. Mamysheva, L. Grüner-Nielsen, and T. Veng, “Demonstration of massive wavelength-division multiplexing over transoceanic distances by use of dispersion-managed solitons,” *Optics Letters* **25**(10), p. 704, 2000.
- [9] H. Murai, H. Yamada, K. Fujii, Y. Ozeki, I. Ogura, T. Ono, and H. Yokoyama, “3 × 80 Gbit/s WDM-transmission over 600 km using mode-locked laser diodes with an 80 Gbit/s OTDM module,” pp. 180–181, 2002.
- [10] I. Ogura, H. Kurita, T. Sasaki, and H. Yokoyama, “Precise operation-frequency control of monolithic mode-locked laser diodes for high-speed optical communication and all-optical signal processing,” *Optical and Quantum Electronics* **33**(7-10), pp. 709–725, 2001.

- [11] D. Cotter, Z. Chen, M. Mitchell, and M. Segev, "Nonlinear Optics for High-Speed Digital Information Processing," **1523**(1999), pp. 1523–1529, 2010.
- [12] P. T. Callahan, M. L. Dennis, and T. R. Clark, "Photonic analog-to-digital conversion," *Johns Hopkins APL Technical Digest (Applied Physics Laboratory)* **30**(4), pp. 280–286, 2012.
- [13] A. Bhatnagar and D. Miller, "Optical Interconnection and Clocking for Electronic Chips," *8th World Multiconference on Systemics, Cybernetics and Informatics (SCI 2004) (Sci)*, pp. 1–5, 2004.
- [14] Y. Wang, J. Li, K. Mo, Y. Wang, F. Liu, and Y. Liu, "14.5 GHz passive harmonic mode-locking in a dispersion compensated Tm-doped fiber laser," *Scientific Reports* **7**(1), pp. 5–10, 2017.
- [15] S. W. Henderson, P. J. M. Suni, C. P. Hale, S. M. Hannon, J. R. Magee, D. L. Bruns, and E. H. Yuen, "Coherent laser radar at 2 μm using solid-state lasers," *IEEE Transactions on Geoscience and Remote Sensing* **31**, pp. 4–15, Jan 1993.
- [16] R. J. De Young and N. P. Barnes, "Profiling atmospheric water vapor using a fiber laser lidar system," *Applied Optics* **49**(4), p. 562, 2010.
- [17] L. Krainer, R. Paschotta, J. A. D. Au, C. Hönninger, U. Keller, M. Moser, D. Kopf, and K. J. Weingarten, "Rapid communication Passively mode-locked Nd : YVO 4 laser with up to 13 GHz repetition rate," **247**, pp. 245–247, 1999.
- [18] A. Bartels, D. Heinecke, and S. A. Diddams, "Passively mode-locked 10 GHz femtosecond Ti:sapphire laser," *Optics Letters* **33**(16), p. 1905, 2008.
- [19] J. J. Plant, J. T. Gopinath, B. Chann, D. J. Ripin, R. K. Huang, and P. W. Juodawlkis, "Slab-Coupled Optical Waveguide Laser," *Optics Letters* **31**(2), pp. 223–225, 2006.
- [20] D. Lorensen, D. J. Maas, H. J. Unold, A. R. Bellancourt, B. Rudin, E. Gini, D. Ebling, and U. Keller, "50-GHz passively mode-locked surface-emitting semiconductor laser with 100-mW average output power," *IEEE Journal of Quantum Electronics* **42**(8), pp. 838–847, 2006.
- [21] U. Keller and A. C. Tropper, "Passively modelocked surface-emitting semiconductor lasers," *Physics Reports* **429**(2), pp. 67–120, 2006.
- [22] M. Mangold, C. A. Zaugg, S. M. Link, M. Golling, B. W. Tilma, and U. Keller, "Pulse repetition rate scaling from 5 to 100 GHz with a high-power semiconductor disk laser," *Optics Express* **22**(5), p. 6099, 2014.
- [23] D. J. Maas, A. R. Bellancourt, B. Rudin, M. Golling, H. J. Unold, T. Südmeyer, and U. Keller, "Vertical integration of ultrafast semiconductor lasers," *Applied Physics B: Lasers and Optics* **88**(4), pp. 493–497, 2007.

- [24] B. Rudin, V. J. Wittwer, D. J. H. C. Maas, M. Hoffmann, O. D. Sieber, Y. Barbarin, M. Golling, T. Südmeyer, and U. Keller, "High-power MIXSEL: an integrated ultrafast semiconductor laser with 64 W average power," *Optics Express* **18**(26), p. 27582, 2010.
- [25] C. G. E. Alfieri, D. Waldburger, J. Nürnberg, M. Golling, and U. Keller, "Sub-150-fs pulses from an optically pumped broadband modelocked integrated external-cavity surface emitting laser," *Optics Letters* **44**(1), p. 25, 2019.
- [26] S. Lefrançois, K. Kieu, Y. Deng, J. D. Kafka, and F. W. Wise, "Scaling of dissipative soliton fiber lasers to megawatt peak powers by use of large-area photonic crystal fiber," *Opt. Lett.* **35**, pp. 1569–1571, May 2010.
- [27] N. Nishizawa and J. Takayanagi, "Octave spanning high-quality supercontinuum generation in all-fiber system," *J. Opt. Soc. Am. B* **24**, pp. 1786–1792, Aug 2007.
- [28] B. Schenkel, "Generation of 3.8-fs pulses from adaptive compression of a cascaded hollow fiber supercontinuum," *Opt. Lett.* **28**(20), pp. 1987–1989, 2003.
- [29] W. Sibbett, A. A. Lagatsky, and C. T. A. Brown, "The development and application of femtosecond laser systems," *Optics Express* **20**(7), p. 6989, 2012.
- [30] F. Wang, A. G. Rozhin, V. Scardaci, Z. Sun, F. Hennrich, I. H. White, W. I. Milne, and A. C. Ferrari, "Wideband-tuneable, nanotube mode-locked, fibre laser," *Nature Nanotechnology* **3**(12), pp. 738–742, 2008.
- [31] J. W. Nicholson and D. J. DiGiovanni, "High-repetition-frequency low-noise fiber ring lasers mode-locked with carbon nanotubes," *IEEE Photonics Technology Letters* **20**(24), pp. 2123–2125, 2008.
- [32] S. Yamashita, Y. Inoue, K. Hsu, T. Kotake, H. Yaguchi, D. Tanaka, M. Jablonski, and S. Y. Set, "5-GHz pulsed fiber fabry-Pérot laser mode-locked using carbon nanotubes," *IEEE Photonics Technology Letters* **17**(4), pp. 750–752, 2005.
- [33] A. Martinez and S. Yamashita, "Multi-gigahertz repetition rate passively modelocked fiber lasers using carbon nanotubes," *Optics Express* **19**, p. 6155, mar 2011.
- [34] R. D. Richtmyer, "Dielectric resonators," *Journal of Applied Physics* **10**(6), pp. 391–398, 1939.
- [35] V. B. Braginsky, M. L. Gorodetsky, and V. S. Ilchenko, "Quality-factor and nonlinear properties of optical whispering-gallery modes," *Physics Letters A* **137**(7-8), pp. 393–397, 1989.
- [36] J. Ward and O. Benson, "WGM microresonators: Sensing, lasing and fundamental optics with microspheres," *Laser and Photonics Reviews* **5**(4), pp. 553–570, 2011.

- [37] T. Herr, M. L. Gorodetsky, and T. J. Kippenberg, "Dissipative Kerr Solitons in Optical Microresonators," *Nonlinear Optical Cavity Dynamics: From Microresonators to Fiber Lasers* **8083**, pp. 129–162, 2015.
- [38] A. A. Savchenkov, V. S. Ilchenko, A. B. Matsko, and L. Maleki, "Kilohertz optical resonances in dielectric crystal cavities," *Physical Review A - Atomic, Molecular, and Optical Physics* **70**(5 A), pp. 1–4, 2004.
- [39] I. Grudinin, A. Savchenkov, A. Matsko, D. Strekalov, V. Ilchenko, and L. Maleki, "Ultra high Q crystalline microcavities," *IQEC, International Quantum Electronics Conference Proceedings* **2005**, pp. 380–381, 2005.
- [40] A. M. Flatae, M. Burrelli, H. Zeng, S. Nocentini, S. Wiegeler, C. Parmeggiani, H. Kalt, and D. Wiersma, "Optically controlled elastic microcavities," *Light: Science and Applications* **4**(4), pp. 2–6, 2015.
- [41] D. K. Armani, T. J. Kippenberg, S. M. Spillane, and K. J. Vahala, "Ultra-high-Q toroid microcavity on a chip," *Nature* **421**(6926), pp. 925–8, 2003.
- [42] L. Yang and K. J. Vahala, "Gain functionalization of silica microresonators," *Optics Letters* **28**(8), p. 592, 2003.
- [43] L. He, a. K. Özdemir, J. Zhu, and L. Yang, "Self-pulsation in fiber-coupled, on-chip microcavity lasers," *Optics Letters* **35**(2), p. 256, 2010.
- [44] F. Sanchez, P. Le Boudec, P. L. François, and G. Stephan, "Effects of ion pairs on the dynamics of erbium-doped fiber lasers," *Physical Review A* **48**(3), pp. 2220–2229, 1993.
- [45] T. Herr, V. Brasch, J. D. Jost, C. Y. Wang, N. M. Kondratiev, M. L. Gorodetsky, and T. J. Kippenberg, "Temporal solitons in optical microresonators," *Nature Photonics* **8**(2), pp. 145–152, 2014.
- [46] S. Yamashita, S. Y. Set, C. S. Goh, and K. Kikuchi, "Ultrafast saturable absorbers based on carbon nanotubes and their applications to passively mode-locked fiber lasers," *Electronics and Communications in Japan (Part II: Electronics)* **90**(2), pp. 17–24, 2007.
- [47] A. Martinez and Z. Sun, "Nanotube and graphene saturable absorbers for fibre lasers," *Nature Photonics* **7**(11), pp. 842–845, 2013.
- [48] W. B. Cho, J. H. Yim, S. Y. Choi, S. Lee, A. Schmidt, G. Steinmeyer, U. Griebner, V. Petrov, D. I. Yeom, K. Kim, and F. Rotermund, "Boosting the nonlinear optical response of carbon nanotube saturable absorbers for broadband mode-locking of bulk lasers," *Advanced Functional Materials* **20**(12), pp. 1937–1943, 2010.
- [49] Y. P. Yariv A., *Photonics: optical electronics in modern communications (6th)*, Oxford University Press, 2006.

- [50] J. C. Knight, G. Cheung, F. Jacques, and T. A. Birks, "Phase-matched excitation of whispering-gallery-mode resonances by a fiber taper," *Optics Letters* **22**(15), p. 1129, 1997.
- [51] G. Liu, V. S. Ilchenko, T. Su, Y.-C. Ling, S. Feng, K. Shang, Y. Zhang, W. Liang, A. A. Savchenkov, A. B. Matsko, L. Maleki, and S. J. Ben Yoo, "Low-loss prism-waveguide optical coupling for ultrahigh-Q low-index monolithic resonators," *Optica* **5**(2), p. 219, 2018.
- [52] C. H. Dong, L. He, Y. F. Xiao, V. R. Gaddam, S. K. Ozdemir, Z. F. Han, G. C. Guo, and L. Yang, "Fabrication of high-Q polydimethylsiloxane optical microspheres for thermal sensing," *Applied Physics Letters* **94**(23), pp. 1–4, 2009.
- [53] X. Xu, W. Chen, G. Zhao, Y. Li, C. Lu, and L. Yang, "Wireless whispering-gallery-mode sensor for thermal sensing and aerial mapping," *Light: Science and Applications* **7**(1), 2018.
- [54] A. M. Armani, R. P. Kulkarni, S. E. Fraser, R. C. Flagan, and K. J. Vahala, "Detection with Optical Microcavities," *Science* **317**(5839), pp. 783–787, 2007.
- [55] J. C. Knight, N. Dubreuil, V. Sandoghdar, J. Hare, V. Lefèvre-Seguin, J. M. Raimond, and S. Haroche, "Mapping whispering-gallery modes in microspheres with a near-field probe," *Optics Letters* **20**(14), p. 1515, 1995.
- [56] T. Herr, V. Brasch, J. D. Jost, I. Mirgorodskiy, G. Lihachev, M. L. Gorodetsky, and T. J. Kippenberg, "Mode spectrum and temporal soliton formation in optical microresonators," *Physical Review Letters* **113**(12), pp. 1–6, 2014.
- [57] H. A., *Waves and fields in optoelectronics*, Prentice-Hall, 1984.
- [58] T. J. Kippenberg, S. M. Spillane, D. K. Armani, and K. J. Vahala, "Ultralow-threshold microcavity Raman laser on a microelectronic chip," *Optics Letters* **29**(11), p. 1224, 2004.
- [59] H.-S. Hsu, C. Cai, and A. M. Armani, "Ultra-low-threshold Er:Yb sol-gel microlaser on silicon," *Optics Express* **17**(25), p. 23265, 2009.
- [60] M. Mennig, G. Jonschker, and H. K. Schmidt, "Sol-gel-derived thick coatings and their thermomechanical and optical properties," *Sol-Gel Optics II* **1758**(July), p. 125, 2004.
- [61] L. Yang, T. Carmon, B. Min, S. M. Spillane, and K. J. Vahala, "Erbium-doped and Raman microlasers on a silicon chip fabricated by the sol-gel process," *Applied Physics Letters* **86**(9), pp. 1–3, 2005.
- [62] F. A. Sigoli, R. R. Gonçalves, Y. Messaddeq, and S. J. Ribeiro, "Erbium- and ytterbium-doped sol-gel SiO₂-HfO₂ crack-free thick films onto silica on silicon substrate," *Journal of Non-Crystalline Solids* **352**(32-35), pp. 3463–3468, 2006.

- [63] B. Min, T. J. Kippenberg, L. Yang, K. J. Vahala, J. Kalkman, and A. Polman, "Erbium-implanted high-Q silica toroidal microcavity laser on a silicon chip," *Physical Review A* **70**, p. 033803, sep 2004.
- [64] L. Yang, D. K. Armani, and K. J. Vahala, "Fiber-coupled erbium microlasers on a chip," *Applied Physics Letters* **83**(5), pp. 825–826, 2003.
- [65] O. Okhotnikov, A. Grudinin, and M. Pessa, "Ultra-fast fibre laser systems based on SESAM technology: new horizons and applications," *New Journal of Physics* **6**, pp. 177–177, nov 2004.
- [66] U. Keller, K. J. Weingarten, F. X. Kartner, D. Kopf, B. Braun, I. D. Jung, R. Fluck, C. Honninger, N. Matuschek, and J. Aus der Au, "Semiconductor saturable absorber mirrors (sesam's) for femtosecond to nanosecond pulse generation in solid-state lasers," *IEEE Journal of Selected Topics in Quantum Electronics* **2**, pp. 435–453, Sep. 1996.
- [67] A. Chong, W. H. Renninger, and F. W. Wise, "Properties of all-normal-dispersion femtosecond fiber lasers," *Conference on Lasers and Electro-Optics, 2007, CLEO 2007* **25**(2), pp. 140–148, 2007.
- [68] A. Chong, J. Buckley, W. Renninger, and F. Wise, "All-normal-dispersion femtosecond fiber laser," *Optics Express* **14**(21), pp. 660–662, 2006.
- [69] N. J. Doran and D. Wood, "Nonlinear-optical loop mirror," *Optics Letters* **13**(1), p. 56, 1988.
- [70] D. Wang, E. A. Golovchenko, A. N. Pilipetskii, C. R. Menyuk, and M. F. Arend, "Nonlinear optical loop mirror based on standard communication fiber," *Journal of Lightwave Technology* **15**(4), pp. 642–646, 1997.
- [71] Y. C. Chen, N. R. Raravikar, L. S. Schadler, P. M. Ajayan, Y. P. Zhao, T. M. Lu, G. C. Wang, and X. C. Zhang, "Ultrafast optical switching properties of single-wall carbon nanotube polymer composites at 1.55 μm ," *Applied Physics Letters* **81**(6), pp. 975–977, 2002.
- [72] Y. Sakakibara, S. Tatsuura, H. Kataura, M. Tokumoto, and Y. Achiba, "Near-infrared saturable absorption of single-wall carbon nanotubes prepared by laser ablation method," *Japanese Journal of Applied Physics, Part 2: Letters* **42**(5 A), 2003.
- [73] S. Y. Set, H. Yaguchi, Y. Tanaka, and M. Jablonski, "Laser Mode Locking Using a Saturable Absorber Incorporating Carbon Nanotubes," *Journal of Lightwave Technology* **22**(1), pp. 51–56, 2004.
- [74] K. Kashiwagi and S. Yamashita, "Optical Deposition of Carbon Nanotubes for Fiber-based Device Fabrication," *Frontiers in Guided Wave Optics and Optoelectronics* (February), pp. 385–402, 2010.

- [75] A. Martinez, M. Al Araimi, A. Dmitriev, P. Lutsyk, S. Li, C. Mou, A. Rozhin, M. Sumetsky, and S. Turitsyn, "Low-loss saturable absorbers based on tapered fibers embedded in carbon nanotube/polymer composites," *APL Photonics* **2**(12), p. 126103, 2017.
- [76] R. I. Woodward and E. J. R. Kelleher, "2D Saturable Absorbers for Fibre Lasers," *Appl. Sci* **5**, pp. 1440–1456, 2015.
- [77] X. M. Liu, H. R. Yang, Y. D. Cui, G. W. Chen, Y. Yang, X. Q. Wu, X. K. Yao, D. D. Han, X. X. Han, C. Zeng, J. Guo, W. L. Li, G. Cheng, and L. M. Tong, "Graphene-clad microfibre saturable absorber for ultrafast fibre lasers," *Scientific Reports* **6**(May), pp. 1–8, 2016.
- [78] Sumlo Iijima, "Helical microtubules of graphitic carbon," *Nature* **354**(354), pp. 56–58, 1991.
- [79] K. S. Ibrahim, "Carbon nanotubes-properties and applications: a review," *Carbon letters* **14**(3), pp. 131–144, 2013.
- [80] M. D. Hanwell, D. E. Curtis, D. C. Lonie, T. E. Z. Vandermeersch, and G. R. Hutchison, "Avogadro: An advanced semantic chemical editor, visualization, and analysis platform," *Journal of Cheminformatics* **4**(17), 2012.
- [81] R. Vajtai, *Springer handbook of nanomaterials*, 2013.
- [82] M. Dresselhaus, G. Dresselhaus, R. Saito, and A. Jorio, "Raman spectroscopy of carbon nanotubes," *Physics Reports* **409**(2), pp. 47–99, 2005.
- [83] K. D. Ausman, R. Piner, O. Lourie, R. S. Ruoff, and M. Korobov, "Organic Solvent Dispersions of Single-Walled Carbon Nanotubes: Toward Solutions of Pristine Nanotubes," *The Journal of Physical Chemistry B* **104**(38), pp. 8911–8915, 2002.
- [84] T. Kumagai, N. Hirota, K. Sato, K. Namiki, H. Maki, and T. Tanabe, "Saturable absorption by carbon nanotubes on silica microtoroids," *Journal of Applied Physics* **123**(23), 2018.
- [85] P. Polimeno, A. Magazzù, M. A. Iatì, F. Patti, R. Saija, C. D. Esposti Boschi, M. G. Donato, P. G. Gucciardi, P. H. Jones, G. Volpe, and O. M. Maragò, "Optical tweezers and their applications," *Journal of Quantitative Spectroscopy and Radiative Transfer* **218**, pp. 131–150, 2018.
- [86] J. Wang, Z. Luo, M. Zhou, C. Ye, H. Fu, Z. Cai, H. Cheng, H. Xu, and W. Qi, "Evanescent-light deposition of graphene onto tapered fibers for passive Q-switch and mode-locker," *IEEE Photonics Journal* **4**(5), pp. 1295–1305, 2012.
- [87] K. Kashiwagi and S. Yamashita, "Optical deposition of carbon nanotubes around tapered fibers," *European Conference on Optical Communication, ECOC* **5**(September), pp. 53–54, 2008.

- [88] K. Kashiwagi and S. Yamashita, "Deposition of carbon nanotubes around microfiber via evanescent light," *Optics Express* **17**(20), p. 18364, 2009.
- [89] S. E. Skelton, M. Sergides, R. Patel, E. Karczewska, O. M. Maragó, and P. H. Jones, "Evanescent wave optical trapping and transport of micro- and nanoparticles on tapered optical fibers," *Journal of Quantitative Spectroscopy and Radiative Transfer* **113**(18), pp. 2512–2520, 2012.
- [90] A. Miniewicz, S. Bartkiewicz, H. Orlikowska, and K. Dradrach, "Marangoni effect visualized in two-dimensions Optical tweezers for gas bubbles," *Scientific Reports* **6**(October), pp. 1–8, 2016.
- [91] A. L. Yarin, W. Liu, and D. H. Reneker, "Motion of droplets along thin fibers with temperature gradient," *Journal of Applied Physics* **91**(7), pp. 4751–4760, 2002.
- [92] K. Kashiwagi, S. Yamashita, and S. Y. Set, "In-situ monitoring of optical deposition of carbon nanotubes onto fiber end," *Optics Express* **17**(7), p. 5711, 2009.
- [93] A. Martinez, K. Fuse, B. Xu, and S. Yamashita, "Optical deposition of graphene and carbon nanotubes in a fiber ferrule for passive mode-locked lasing," *Optics Express* **18**(22), p. 23054, 2010.
- [94] J. Zhu, S. K. Ozdemir, Y. F. Xiao, L. Li, L. He, D. R. Chen, and L. Yang, "On-chip single nanoparticle detection and sizing by mode splitting in an ultrahigh-Q microresonator," *Nature Photonics* **4**(1), pp. 46–49, 2010.
- [95] T. J. Kippenberg, "Microresonators: Particle sizing by mode splitting," *Nature Photonics* **4**(1), pp. 9–10, 2010.
- [96] G. Agrawal, *Nonlinear Fiber Optics Fifth Edition*, 2013.
- [97] U. Morgner, S. H. Cho, H. A. Haus, E. P. Ippen, J. G. Fujimoto, Y. Chen, and F. X. Ka, "Dispersion-managed mode locking," *Journal of the Optical Society of America B* **16**(11), pp. 1999–2004, 1999.
- [98] L. F. Mollenauer and P. V. Mamyshev, "Massive wavelength-division multiplexing with solitons," *IEEE Journal of Quantum Electronics* **34**(11), pp. 2089–2102, 1998.
- [99] H. A. Haus, "Theory of Mode Locking with a Fast Saturable Absorber," *IEEE Journal of Quantum Electronics* **11**(9), pp. 736–746, 1975.
- [100] H. A. Haus, J. G. Fujimoto, and E. P. Ippen, "Structures for additive pulse mode locking," *Journal of the Optical Society of America B* **8**(10), p. 2068, 1991.
- [101] H. A. Haus, "Mode-locking of lasers," *IEEE Journal on Selected Topics in Quantum Electronics* **6**(6), pp. 1173–1185, 2000.

- [102] I. A. Yarutkina, O. V. Shtyrina, M. P. Fedoruk, and S. K. Turitsyn, "Numerical modeling of fiber lasers with long and ultra-long ring cavity," *Optics Express* **21**(10), p. 12942, 2013.
- [103] F. X. Kärtner, J. Aus Der Au, and U. Keller, "Mode-locking with slow and fast saturable absorbers - What's the difference?," *IEEE Journal on Selected Topics in Quantum Electronics* **4**(2), pp. 159–168, 1998.
- [104] C. Rasmussen, "Simple and fast method for step size determination in computations of signal propagation through nonlinear fibres," *OFC 2001. Optical Fiber Communication Conference and Exhibit. Technical Digest Postconference Edition (IEEE Cat. 01CH37171)* **3**(1), pp. 1–3, 2001.
- [105] J. W. Nicholson, R. S. Windeler, and D. J. Digiovanni, "Optically driven deposition of single-walled carbon-nanotube saturable absorbers on optical fiber end-faces," *Optics express* **15**(15), pp. 9176–9183, 2007.
- [106] P. C. Becker, N. A. Olsson, and J. R. Simpson, *Erbium-doped Fiber Amplifiers*, Academic Press, 1999.
- [107] C. K. Ryu, H. Choi, and K. Kim, "Fabrication of highly concentrated Er³⁺ doped aluminosilicate films via sol-gel processing," *Applied Physics Letters* **66**(19), pp. 2496–2498, 2002.
- [108] J. Ma, X. Jiang, and M. Xiao, "Kerr frequency combs in large-size, ultra-high-Q toroid microcavities with low repetition rates," *Photonics Research* **5**(6), p. B54, 2017.
- [109] P. Del'Haye, O. Arcizet, A. Schliesser, R. Holzwarth, and T. J. Kippenberg, "Full stabilization of a microresonator-based optical frequency comb," *Physical Review Letters* **101**(5), pp. 1–4, 2008.
- [110] J. N. Kutz, B. C. Collings, K. Bergman, and W. H. Knox, "Stabilized pulse spacing in soliton lasers due to gain depletion and recovery," *IEEE Journal of Quantum Electronics* **34**(9), pp. 1749–1757, 1998.
- [111] J. W. Lee, K. Y. Kim, H. J. Moon, and K. S. Hyun, "Selection of lasing direction in single mode semiconductor square ring cavities," *Journal of Applied Physics* **119**(5), 2016.
- [112] Y. Shi, M. Sejka, and O. Poulsen, "A Unidirectional Er³⁺ -Doped Fiber Ring Laser without Isolator," *IEEE Photonics Technology Letters* **7**(3), pp. 290–292, 1995.
- [113] B. Peng, a. K. Özdemir, M. Liertzer, W. Chen, J. Kramer, H. Yilmaz, J. Wiersig, S. Rotter, and L. Yang, "Chiral modes and directional lasing at exceptional points," *Proceedings of the National Academy of Sciences* **113**(25), pp. 6845–6850, 2016.

- [114] G. Sobon, A. Duzynska, M. Świniarski, J. Judek, J. Sotor, and M. Zdrojek, “CNT-based saturable absorbers with scalable modulation depth for Thulium-doped fiber lasers operating at 1.9 μm ,” *Scientific Reports* **7**(February), pp. 1–9, 2017.
- [115] S. T. Cundiff, “New generation of combs,” *Nature* **450**(7173), pp. 1175–1176, 2007.